Master's thesis

NTNU
Norwegian University of Science and Technology
Faculty of Natural Sciences
Department of Materials Science and Engineering

Mika Serna Malmer

Combining $LiNi_{0.5}Mn_{1.5}O_4$ Cathodes with Phosphonium-based Ionic Liquids in Li-ion Batteries

Master's thesis in Materials Chemistry and Energy Technology
Supervisor: Ann Mari Svensson
Co-supervisor: Inger-Emma Nylund, Johan Hamonnet
June 2023

NTNU
Norwegian University of
Science and Technology

Mika Serna Malmer

Combining $LiNi_{0.5}Mn_{1.5}O_4$ Cathodes with Phosphonium-based Ionic Liquids in Li-ion Batteries

Master's thesis in Materials Chemistry and Energy Technology
Supervisor: Ann Mari Svensson
Co-supervisor: Inger-Emma Nylund, Johan Hamonnet
June 2023

Norwegian University of Science and Technology
Faculty of Natural Sciences
Department of Materials Science and Engineering

NTNU
Norwegian University of
Science and Technology

Preface

This master's thesis is the outcome of the course TMT4900 - Materials Chemistry and Energy Technology, Master's Thesis, carried out at Department of Materials Science and Engineering at Norwegian University of Science and Technology (NTNU) the spring semester 2023. The work done in this thesis is related to and builds on the specialisation project report produced by the same author during the autumn semester 2022, with the title "Combining $LiNi_{0.5}Mn_{1.5}O_4$ Cathodes with Lithium Bis(fluorosulfonyl)imide-based Electrolytes". As the literature basis of that report was similar, some sections of the theory were adapted, rephrased and extended for the use in this thesis. Also, the experimental procedures in the methods utilised in the report have been proceeded.

First of all, I want to express gratitude to my supervisor during both the specialisation project and the master's thesis, Professor Ann Mari Svensson, for always being available for valuable discussions and helpful guidance. Also, she introduced me to the fascinating battery technology field, which I hope to be a part of for a long time to come. Secondly, I want to thank my co-supervisor and Postdoctoral Fellow Inger-Emma Nylund for consistently being available for questions and for giving me fundamental training, whether it concerned assembly of battery cells or characterisation with SEM. Despite that he late became a part of the project, Postdoctoral Fellow Johan Hamonnet has contributed with important feedback. I very much appreciate the work the engineers in Chemistry Block 2 put in for keeping the laboratories up and running, especially Pei Na Kui, Marthe Folstad and Johannes Ofstad. I also want to thank the electrochemistry group and the battery group for fruitful discussions and feedback during the last year. Last, but not least, I want to thank my remarkable and supportive friends that I have met through my studies, who I know will continue to play an important role in my life. The Research Council of Norway is acknowledged for the support to the Norwegian Micro- and Nano-Fabrication Facility, NorFab, project number 295864.

Mika Serna Malmer
Trondheim, 18.06.2023

Abstract

This thesis aims to develop an alternative electrolyte for the use with the high voltage cathode material $LiNi_{0.5}Mn_{1.5}O_4$ (LNMO) in Li-ion batteries (LIBs), with the intention of substituting the salt $LiPF_6$ in carbonate-based electrolytes. Cathode materials in commercial LIBs today are mainly build up from transition metal oxides, which implies the use of scarce and costly elements as cobalt, which also raise ethical concerns. LNMO is a cathode material which has received attention for the use in next generation LIBs, as it offers a higher operating potential than conventional materials and also does not involve cobalt. However, the combination of LNMO with $LiPF_6$ in carbonate gives rise to challenges with hydrofluoric acid (HF) formation, especially at higher temperatures. This will further contribute to cell degradation through accelerating transition metal dissolution of the active material, in addition of being a safety concern. There is an ambition to develop an alternative electrolyte system to tackle these issues, based on the salt LiFSI dissolved in the room temperature ionic liquid (RTIL) $P_{111i4}FSI$. RTILs are a type of electrolytes which recently have gained attention for the use in LIBs, as they provide superior safety than conventional nonaqueous aprotic electrolytes, and at the same time offers a high thermal and electrochemical stability, making it suitable for the use with LNMO. Since the conductive carbon additive in conventional electrodes is found to give rise to side reaction, it is also of interest to examine the cyclability of bare LNMO electrodes with both the conventional carbonate-based electrolyte and the RTIL.

Initially, half cells with LNMO against lithium with LP40 (1M $LiPF_6$ in EC/DEC 1:1) were assembled and galvanostatic cycled as a reference. Next, electrolyte with 0.79 m and 3 m LiFSI in $P_{111i4}FSI$ were prepared and cycled in similar cells as the reference for 200 C/2 cycles and in a rate test at higher C-rates. Potentiostatic electrochemical impedance spectroscopy (PEIS) was also conducted to measure the cell's ohmic resistance. In the end, the LNMO electrodes were extracted and characterised post-mortem with scanning electron microscopy (SEM), energy dispersive X-ray spectrometry (EDS) and Raman spectroscopy. Additionally, LNMO without conductive carbon additive was fabricated and attempted cycled at a low C-rate.

The low-concentrated RTIL performed superior to the high-concentrated RTIL and also LP40, accomplishing a discharge capacity of 112 mAh/g and a coulombic efficiency above 99% after 200 C/2 cycles, resulting in a capacity retention of 86.8% (compared to 84.8% of LP40). However, at C-rates up to 2C, the RTILs were outperformed by LP40. As the discharge capacity increased up to initial level

when decreasing the C-rate, electrolyte kinetics are considered the limiting factor, not severe degradation of the active material. Post-mortem characterisation revealed an electrode surface of the low-concentrated RTIL which was more intact and similar to the pristine material than with LP40, where a surface film was formed during cycling. The high-concentrated RTIL showed a significantly different electrode surface with less visible LNMO particles and a dominating network surrounding them, probably caused by the higher salt concentration and viscosity of the RTIL. LNMO without conductive carbon additive failed to produce any capacity during slow cycling, probably due to poor conductivity.

Sammendrag

Denne avhandlingen har som mål å utvikle en alternativ elektrolytt for bruk med høyspenningkatodematerialet $LiNi_{0.5}Mn_{1.5}O_4$ (LNMO) i Li-ion-batterier, med hensikt å erstatte karbonatbaserte elektrolytter med saltet $LiPF_6$. Katodematerialet i kommersielle Li-ion-batterier i dag består av overgangsmetalloksider, som involverer bruken av sjeldne og kostbare grunnstoffer som kobolt, og som også gir opphav til etiske utfordringer. LNMO er et katodemateriale som er ansett som interessant for bruk i neste generasjons Li-ion-batterier, ettersom det byr på en høyere driftsspenning enn konvensjonelle materialer og heller ikke involverer bruken av kobolt. Imidlertid fører kombinasjonen av LNMO med $LiPF_6$ i karbonat med seg utfordringer når det gjelder dannelse av flussyre, spesielt ved høyere temperaturer. Dette vil videre føre til degradering av cellen gjennom akselerering av overgangsmetallopløsning av det aktive materialet, i tillegg til å være en sikkerhetsutfordring. Med dette i tankene så er det en ambisjon å utvikle et alternativt elektrolyttsystem for å takle disse problemene, basert på saltet LiFSI oppløst i den ioniske væsken $P_{111i4}FSI$. Ioniske væsker er en type elektrolytter som nylig har fått oppmerksomhet for sin bruk i Li-ion-batterier, ettersom de byr på en bedre sikkerhet enn konvensjonelle ikke-vanndige aprotiske elektrolytter, samtidig som de byr på høy termisk og elektrokjemisk stabilitet, noe som gjør de til egnede for bruk med LNMO. Siden strømledende tilsetningsstoffer av karbon i konvensjonelle elektroder forårsaker sidereaksjoner, er det også av interesse å undersøke i hvilken grad celler med LNMO uten karbon er i stand til å sykle, både med ionisk væske og konvensjonell karbonatbasert elektrolytt.

Først ble halvceller med LNMO mot litium med LP40 (1M $LiPF_6$ i EC/DEC 1:1) satt sammen og galvanostatisk syklet som en referanse. Deretter ble elektrolytt bestående av 0.79 m og 3 m LiFSI i $P_{111i4}FSI$ preparert og syklet i lignende celler som med referansen over 200 C/2 sykler og ved høyere syklingsrater. Potentiostatisk elektrokjemisk impedansspektroskopi ble også utført for å måle cellenes ohmske motstand. Til slutt ble LNMO elektrodene tatt ut fra cellene og karakterisert med sveipelektronmikroskop, energidispersiv røntgenanalyse og Raman spektroskopi. I tillegg ble LNMO uten karbon lagd og forsøkt syklet ved lav syklingsrate.

Den lavkonsentrerte ioniske væsken presterte bedre sammenlignet med den høykonsentrerte ioniske væsken og LP40, og oppnådde en utladningskapasitet på 112 mAh/g og en colombisk effektivitet på over 99% etter 200 C/2 sykler, som resulterte i en kapasitetsbevaring på 86.8% (sammenlignet med 84.8% for LP40). Ved høye syklingrater opp mot 2C så ble de ioniske væskene imidlertidig utkonkur-

rert av LP40. Siden utladningskapasiteten økte opp mot opprinnelig nivå da syklingraten gikk ned igjen så tyder dette på at elektrolyttkinetikk er den begrensende faktoren, ikke alvorlig degradering av det aktive materialet. Karakterisering av elektrodene etter endt sykling viste at elektrodeoverflate til den lavkonsentrerte ioniske væsken var mer intakt og likt det friske elektrodemateriale enn med LP40, hvor det ble observert en overflatefilm etter sykling. Den høykonsentrerte ioniske væsken viste en betydelig annerledes elektrodeoverflate med mindre synlige LNMO-partikler og et dominerende nettverk rundt dem, antageligvis grunnet en høyere saltkonsentrasjon og viskositet. LNMO uten karbon mislyktes i å produsere kapasitet gjennom sakte sykling, sannsynligvis på grunn av dårlig ledningsevne.

Contents

List of Figures

List of Tables

Abbreviations

List of abbreviations in alphabetic order:

BSE	Backscattered electrons
CE	Coulombic efficiency
CEI	Cathode electrolyte interphase
DEC	Diethyl carbonate
DMC	Dimethyl carbonate
EC	Ethylene carbonate
EDS	Energy dispersive X-ray spectroscopy
ESS	Energy storage system
FEC	Fluoroethylene carbonate
GEIS	Galvanostatic electrochemical impedance spectroscopy
HF	Hydrofluoric acid
IR	Infrared
LCO	$LiCoO_2$
LFP	$LiFePO_4$
LIB	Li-ion battery
LiBOB	Lithium bis(oxalato)borate
LiDFOB	Lithium difluoro(oxalato)borate
LiFSI	Lithium bis(fluorosulfonyl)imide

LMO	$LiMn_2O_4$
LNMO	$LiNi_{0.5}Mn_{1.5}O_4$
LP40	1M $LiPF_6$ in EC/DEC 1:1
LTO	$Li_4Ti_5O_{12}$
NMC	$LiNi_xMn_yCo_{1-x-y}O_2$
NMP	N-methyl-2-pyrrolidone
PE	Polyethylene
PEC	Poly(ethylene carbonate)
PEO	Poly(ethylene oxide)
PET	Polyethylene terephthalate
PP	Polypropylene
PVDF	Polyvinylidene fluoride
PEIS	Potentiostatic electrochemical impedance spectroscopy
RTIL	Room temperature ionic liquid
SE	Secondary electrons
SEI	Solid electrolyte interphase
SEM	Scanning electron microscopy
SOC	State of charge
UV	Ultraviolet
VC	Vinylene carbonate

Chapter 1

Introduction

The world's population is in the middle of a very complex situation. Ever since the industrial revolution, we have faced an incredible technological development and we continue in the search of ways to improve our lives. At the same time, we are encountering a serious climate crisis, which makes it an urgent matter to take action. In the context of the IPCC climate report presented this spring, UN Secretary General António Guterres stated that *"We need a renewables revolution, not a self-destructive fossil fuel resurgence."* [1]. With this in mind, it has never been more important to keep up the technological development we have seen so far in the history, yet is has to be shifted towards namely renewable energy. With a greater focus on renewable energy follows a need of storing the produced energy through energy storage systems (ESS) so it can be used when there is a higher demand [2]. We have also seen a high growth of electrical battery vehicles on the roads the recent years, which is expected to continue and surpass fossil fuel driven vehicles in the next years [3].

Secondary Li-ion batteries (LIBs), meaning they are rechargeable, were introduced in the 80s and have dominated the market of ESS already for a long period. LIBs stand out from previous technologies with an exceptional energy density, as well as an efficiency close to 100% [2]. As for all technology, there is a continuous demand in upgrading LIBs and make them suitable for new applications. To improve the technology there is a focus on especially two factors: make the units cheaper and enhance the energy density. The cathode is the component which constitutes to the largest part of the cell cost and is also the limiting factor in terms of energy density [4]. The latter is determined by both the cathode material's operating potential and theoretical capacity. $LiNi_{0.5}Mn_{1.5}O_4$ (LNMO) has been introduced as a promising cathode material, as it offers a significantly higher operating potential than most conventional cathode materials. Another important feature is that it

does not involve cobalt, which gives rise to ethical concerns [5].

For LNMO to succeed as cathode material in LIBs, it must work well with the other components of the cell. The conventional electrolyte in LIBs today are non-aqueous aprotic electrolytes, such as the salt $LiPF_6$ in carbonate-based solvents. In combination with LNMO, especially at higher temperatures, the salt may react with small amounts of water or alcohols and undergo hydrolysis, which will result in the formation of hydrofluoric acid (HF). This acid will accelerate transition metal dissolution of manganese and nickel from the active material and thus decrease the cell performance. Also, it gives rise to safety concerns [6]. Room temperature ionic liquids (RTILs) is another type of electrolytes which lately has received focus, as they offer superior safety than conventional nonaqueous aprotic electrolytes, in addition to providing a high thermal stability and a high electrochemical stability between 2 and 6 V [7]. The reason they are not commercialised yet is because they face certain issues, such as high cost and high viscosity, resulting in a low electronic conductivity [2]. Phosphonium-based RTILs, such as $P_{111i4}FSI$, have been introduced as a potential candidate for enhancing the generally poor conductivity of RTILs, and have showed improving transport properties and a wider electrochemical window with the addition of the salt LiFSI [8]. A wider electrochemical window is especially relevant for high voltage cathodes as LNMO to avoid decomposition of the electrolyte. With that considered, LiFSI in $P_{111i4}FSI$ has been investigated in combination with LNMO. The conductive carbon additive in LNMO electrodes is believed to contribute to cell degradation as it is a basis of side reactions [9]. Therefore, LNMO electrodes without conductive additive were fabricated and tested with both the conventional electrolyte and the RTIL.

Aim of Work

The aim of this master's thesis was to study the combination of the cathode active material LNMO with alternative electrolytes. This is related to the specialisation project last semester, where the aim was to investigate the combination of LNMO with an electrolyte based on the salt LiFSI dissolved in carbonate solvent. However, the outcome with such electrolyte was not as intended. Therefore, the focus was shifted against the ionic liquid $P_{111i4}FSI$ with the addition of the salt LiFSI. This thesis has investigated the electrochemical performance of this electrolyte in comparison to a conventional carbonate-based electrolyte with the salt $LiPF_6$. Cells with the different electrolytes were cycled over a long period and characterised with the aim to understand how LNMO with the electrolytes degrades. Publications have arrived at different concentrations of salt in the ionic liquid, for that reason there is a desire to conclude whether a high or low salt concentration will result in the best performance. Additionally, it is believed that the conductive carbon additive in LNMO electrodes is a source to side reaction which leads to the degradation of the cell. Consequently, LNMO electrodes without carbon as conductive additive was fabricated and attempted cycled with both conventional electrolyte and ionic liquid.

To begin with, reference cells with the conventional electrolyte composed of $LiPF_6$ in carbonate were assembled and galvanostatic cycled for 200 C/2 cycles. Then, cells with 0.79 m and 3 m LiFSI in $P_{111i4}FSI$ were cycled and compared against the reference cells. To study their performance also at higher cycling rates, rate tests were conducted with all electrolytes, followed by measurements of ohmic resistance. In the end, LNMO without conductive additive was fabricated to investigate the electrode material's cycling capability. In addition to the electrochemical testing, cells with all the electrolytes were disassembled and characterised post-mortem with SEM, EDS and Raman spectroscopy to study the electrode degradation.

Chapter 2

Theory

2.1 Li-Ion Batteries

A Li-ion battery (LIB) is a device made to store electrical energy as chemical energy. Hence, a LIB can supply this energy and function as a power source when there is demand. These devices are also called secondary batteries since they can be recharged, as the chemical reactions occurring during the cycling are reversible. Whereas the structure of a LIB can be standardised, the components in different types of LIB may differ substantially. All LIB cells consist of two electrodes, an anode and a cathode. When the cell is discharging, the anode undergoes oxidation, meaning electrons are extracted. On the other hand, the cathode undergoes reduction and receives electrons. During the charging of LIBs, the electron transport will be reversed [10].

The cathode is made up from a slurry which consists of an active material, which constitutes the majority of the slurry, together with a binder and a conductive additive. The purpose of the binder is to plasticise the electrode and make it manageable, and polyvinylidene fluoride (PVDF) is commonly used. The conductive additive, usually a type of carbon black, is added to increase the electrical conductivity of the electrode, in addition to absorb the expansion/contraction of the powder particles. Between the anode and the cathode, Li-ions flow and intercalation occurs, which can be explained as a reversible process in the layered structure of the anode/cathode where introduction and removal of Li-ions take place. With the purpose of establishing connection between the active material of the electrodes and the power source, the electrodes are coupled with current collectors, where Al is generally used for the cathode and Cu for the anode. A liquid electrolyte with the function to conduct Li-ions is located between the anode and the cathode. Since the electrolyte has a great ionic conductivity and

simultaneously behaves as an electronic insulator, it also ensures that the electrical charge pass in the external circuit. A separator is placed between the anode and the cathode, which must be permeable to the electrolyte. Its main function is to behave as a physical barrier between the electrodes to prevent short circuiting of the cell [2]. The overall structure of a LIB cell is presented in Figure 2.1.1.

The cathode is cast from a slurry consisting of an active material, a binder, and a conductive additive. The purpose of the binder, usually made of polyvinylidene fluoride (PVDF), is to plasticise the electrode and make the cast mechanically stable. The conductive additive, usually a type of carbon black, is added to increase the electrical conductivity of the electrode and absorb the expansion/contraction of the particles. The Li-ions flow and intercalation occurring between the anode and the cathode can be explained as a reversible process in the layered structure of the anode/cathode where the introduction and removal of Li-ions occur. The electrodes are coupled with current collectors to establish a connection between the active material of the electrodes and the power source, where Al is generally used for the cathode and Cu for the anode. A liquid electrolyte that conducts Li-ions is located between the anode and the cathode. Since the electrolyte has excellent ionic conductivity and simultaneously behaves as an electronic insulator, it also ensures that the electrical charge passes on the external circuit. Finally, a separator is also placed between the anode and the cathode, which must be permeable to the electrolyte. Its main function is to be a physical barrier between the electrodes to prevent the cell from short-circuiting [2]. The overall structure of a LIB cell is presented in Figure 2.1.1.

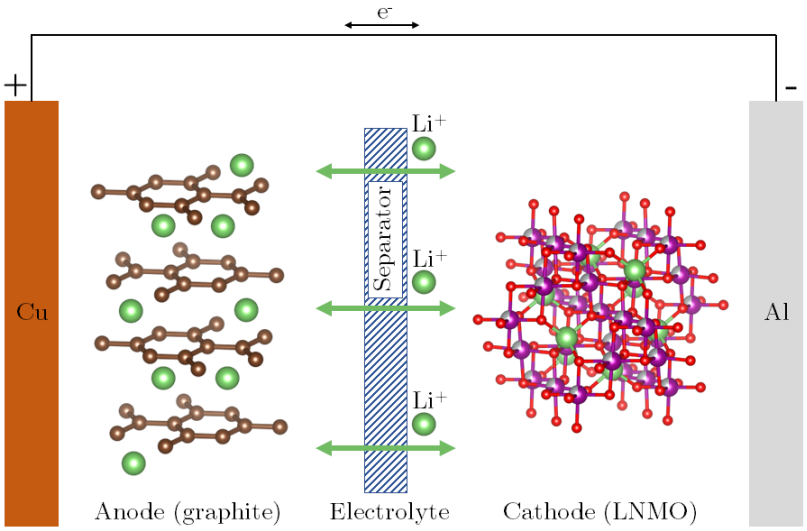

Figure 2.1.1: Structure of a LIB, with graphite as the anode material and LNMO as the cathode material.

The electrochemical reaction which takes place in a graphite anode during charge/discharge is expressed in Equation 2.1:

$$\mathrm{xLi^+ + xe^- + 6\,C} \underset{discharge}{\overset{charge}{\rightleftharpoons}} \mathrm{Li_xC_6}, \tag{2.1}$$

where x is the number of electrons taking part in the reaction.

The electrochemical reaction occurring in the transition metal oxide cathode, in this case $\mathrm{LiNi_{0.5}Mn_{1.5}O_4}$ (LNMO) with a theoretical capacity of 147 mAh/g [11], is expressed in Equation 2.2:

$$\mathrm{LiNi_{0.5}Mn_{1.5}O_4} \underset{discharge}{\overset{charge}{\rightleftharpoons}} \mathrm{Li_{1-x}Ni_{0.5}Mn_{1.5}O_4 + xLi^+ + xe^-}. \tag{2.2}$$

The total LIB cell reaction is expressed in Equation 2.3:

$$\mathrm{LiNi_{0.5}Mn_{1.5}O_4 + 6\,C} \underset{discharge}{\overset{charge}{\rightleftharpoons}} \mathrm{Li_{1-x}Ni_{0.5}Mn_{1.5}O_4 + Li_xC_6}. \tag{2.3}$$

2.2 Basic Terminology and Parameters

Some specific parameters and expressions are used to describe LIBs adequately.

V_{oc}, the open circuit potential, is the voltage difference between the anode and the cathode while no current is drawn from the cell. The equation describing the open circuit potential is presented in Equation 2.4 [2]:

$$V_{oc} = -\frac{1}{nF}(\mu^i_{\text{anode}} - \mu^i_{\text{cathode}}), \tag{2.4}$$

where n represents the number of electrons taking part in the chemical reaction, F is the Faraday's constant and $(\mu^i_{\text{anode}} - \mu^i_{\text{cathode}})$ is the difference in electrochemical potential between the electrodes.

The capacity of a LIB is the charge that may be stored in a cell. It is measured in Ah and expressed in Equation 2.5 [10]:

$$Q = \int_0^{\Delta t} I dt = \int_0^{\Delta t} \frac{dq}{dt} dt = \int_0^{Q} dq. \tag{2.5}$$

The C-rate characterises the time of a LIB's charge and discharge process. More specifically, it measures the charge/discharge current in proportion to the maximum capacity. A C-rate equal to zC implies complete charge or discharge in $1/z$ hours [2]. For example, C/5 represents the current charging or discharging the cell

for five hours.

CE is the coulombic efficiency and is the ratio between the discharge and charge capacity. It is calculated for every cycle. This value can also characterise the loss of Li ions after each cycle. *CE* is expressed in Equation 2.6 [2]:

$$CE[\%] = \frac{Q_{\text{discharge}}}{Q_{\text{charge}}} \cdot 100\%. \tag{2.6}$$

Capacity retention is described as the capacity available as a percentage of the initial capacity after a certain number of cycles. A battery which does not undergo any capacity loss will have a capacity retention of 100% [2].

The state of charge (SOC) of a LIB is the portion of available charge capacity relative to the total battery capacity, in percentage. SOC is a useful parameter to indicate the available energy in the battery before it is charged again. The formula describing it is given in Equation 2.7 [2]:

$$SOC[\%] = 100\% - \frac{Q_e}{Q_0}, \tag{2.7}$$

where Q_e represents the charge of the battery and Q_0 is the nominal capacity in the unit Ah.

The calendar life is determined by assessing the capacity retention when the cell is inactive at a given SOC [2].

The cycle life is defined by the number of cycles a cell can handle before a capacity retention of 80% is reached [10].

The available energy measures the cell's performance when a LIB is fully charged. It may be described as energy density through volumetric energy density [Wh L^{-1}] or gravimetric energy density [Wh kg^{-1}]. The value is described by Equation 2.8 [10]:

$$\text{Energy [Wh]} = \int_0^{\Delta t} IV(t)dt = \int_0^{Q} V(q)dq. \tag{2.8}$$

2.3 Cathode Materials

The active cathode material is usually composed of a transition metal oxide. Li ions will move from the active material during the charge, and the cathode will oxidise. This process is often referred to as delithiation. On the contrary, lithiation occurs with the insertion of Li-ions in the cathode material during discharge. In contrast to other LIB components, the cost of the cathode cost has increased recently, accounting for a significant share of the total cost of the cell [4]. Furthermore, the cathode can be considered a limiting factor for the cell's energy density since its specific capacity is significantly lower than that of most anode materials. Therefore, enhancing the cathode material has been a recent focus. The characteristics that a cathode should possess are the following [12]:

- Being able to undergo a reversible reaction between the cathode material and the Li-ions without modifying the structure.
- Having a high free energy for the reaction between the cathode and Li, leading to both a high capacity and high potential, with the ability to store much energy.
- The reaction between the cathode and Li should be fast to allow a high-power density.
- The materials should have sufficient electronic conductivity so that the rates of the oxidation and reduction reactions in the porous structures are high.
- The material should be stable, inexpensive and environmentally friendly.

There are two main types of cathode materials utilised, and they are differenced by their structure. The first one possesses a layered structure, meaning that the Li-ions are stored between the layers. This class of cathode materials consist mainly of transition metal oxides and sulfides, such as $LiTiS_2$, $LiVSe_2$, $LiCoO_2$ (LCO), $LiNiO_2$ and $LiNi_xMn_yCo_{1-x-y}O_2$[12]. The latter cathode material is called NMC and was first developed by Liu et al. [13] as an improvement for LCO, offering superior calendar life and thermal stability. The limiting factor of these cathode materials is the inclusion of cobalt, which raises ethical and environmental issues [14]. Spinels is another type of structure which can be regarded as a sub class of layered structures, where transition metal cations are arranged in all the layers. An example of a spinel-type material is LNMO, which will be assessed in detail in Section 2.3.1. One of the benefits of is their high volumetric capacity, which is due to their compact lattices. The second class of cathode materials has a more open structure, such as olivine $LiFePO_4$ (LFP) [12]. Although LFP possesses a

lower capacity and operating potential than other materials, it is still suitable for certain applications as it is significantly cheaper and more environmentally friendly because it does not contain cobalt or nickel. The voltages and capacities of relevant cathode materials are compared in Figure 2.3.1.

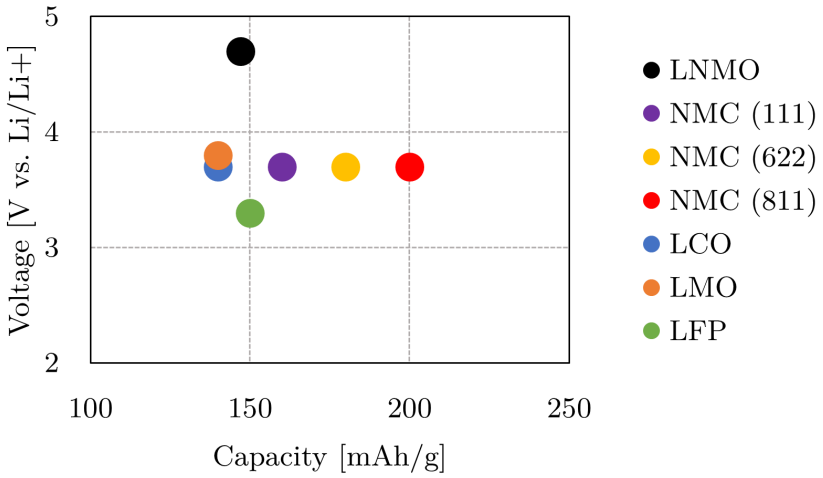

Figure 2.3.1: A comparison of the voltage and the specific capacity of cathode materials [15] [16] [11].

2.3.1 LNMO

LNMO is a cathode material that has received significant attention in the recent years as a promising material for the next generation of LIBs [17]. This material has a 4.7 V vs Li/Li^+ operating voltage because of the Ni^{2+}/Ni^{4+} redox couple, which is high compared to the conventional alternatives, shown in Figure 2.3.1. In addition, it offers a theoretical capacity of 147 mAh/g [11]. The high operating voltage of the material leads to a high energy density of 650 Wh/kg with a graphite anode which is 162.5% higher than that of a $LiMn_2O_4$ (LMO) cell. Since LNMO has a three-dimensional structure, as shown in Figure 2.3.2, it gives rise to fast diffusion of lithium ions, which gives the material a high ionic conductivity. LNMO also has an exceptional thermal stability and is a more environmentally friendly alternative to other cathode materials, as it does not contain cobalt. However, LNMO faces problems, such as electrolyte decomposition due to the high operating voltage and transition metal dissolution, leading to a rapid decrease in capacity [5].

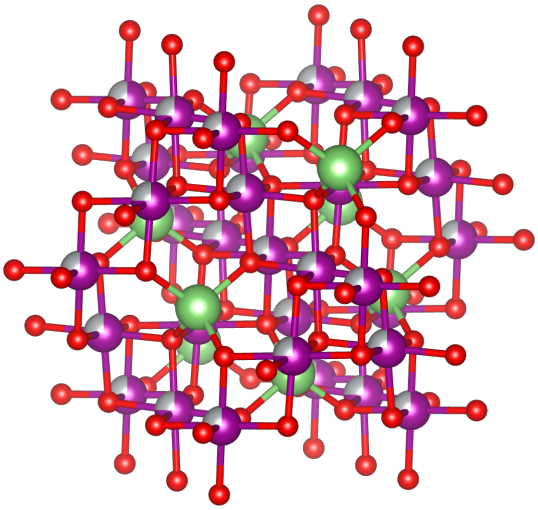

Figure 2.3.2: Disordered LNMO with space group $Fd\bar{3}m$, made with VESTA [18]. Li-atoms in green, Mn-atoms in purple, Ni-atoms in grey and O-atoms in red.

2.3.1.1 Structure

LNMO can adopt either an ordered or disordered structure depending on the sintering temperature used during its fabrication. A primitive, simple cubic structure with the space group $P4_332$ characterises the ordered structure. In contrast, the disordered structure is identified by a face-centred cubic (FCC) structure with the space group $Fd\bar{3}m$ [5]. Disordered LNMO will be the material used in this thesis, with the structure of the material is illustrated in Figure 2.3.2. For this FCC structure, the unit cell comprises tetrahedral 8a sites occupied with Li ions, arbitrarily allocated Mn/Ni-ion-occupied octahedral 16d sites, and cubic close-packed 32e sites occupied by O [19].

The location of Ni and Mn determines whether the structure will be of the ordered or disordered type. The latter structure will be created when the sintering temperature surpasses 700 °C. To maintain electron neutrality, oxygen loss in the disordered structure reduces Mn^{4+} to Mn^{3+}, which can lead to a higher electronic conductivity for the disordered structure [20]. This structure also demonstrates a more stable cycling performance than the ordered structure, as the ordered LNMO shows a higher resistance during delithiation. While the disordered type experiences a single-step phase transition, the ordered type experiences a partial phase transition over two steps. It is also established that the disordered LNMO possesses both a better electrochemical behaviour and structural reversibility [19].

The Raman spectrum in Figure 2.3.3a shows the characteristic peaks of disordered LNMO with the space group $Fd\bar{3}m$. Compared to the ordered type, the spectra of the disordered type contains less distinct and sharp peaks. For instance, the peaks representing Ni-O bands at 166 and 410 cm^{-1} are more intense in the structure with the space group $P4_332$ [21]. Ordered LNMO also includes split peaks at approximately 588–623 cm^{-1} [22]. Carbon, commonly added as conductive additive to the electrode slurry, possesses two characteristic bands. The D-band at 1350 cm^{-1} represents disordered lattice vibrations with A_{1g} symmetry and is therefore often referred to as the disorder or defect band. An intense D-band therefore indicates many defects in the carbon. The G-band at 1600 cm^{-1} reflects lattice vibrations with E_{2g} symmetry [23].

The electrochemical behaviour of the two structures can be easily distinguished when observing the potential plateaus. A small plateau due to the Mn^{3+}/Mn^{4+} redox couple can be observed for the disordered type at around 4 V vs. Li/Li^+. At elevated voltage, two major plateaus occur at 4.6 and 4.8 V vs. Li/Li^+, originating from the Ni^{2+}/Ni^{3+} and Ni^{3+}/Ni^{4+} redox couples, respectively [5]. Figure 2.3.3b shows the position of the plateaus during both charge and discharge.

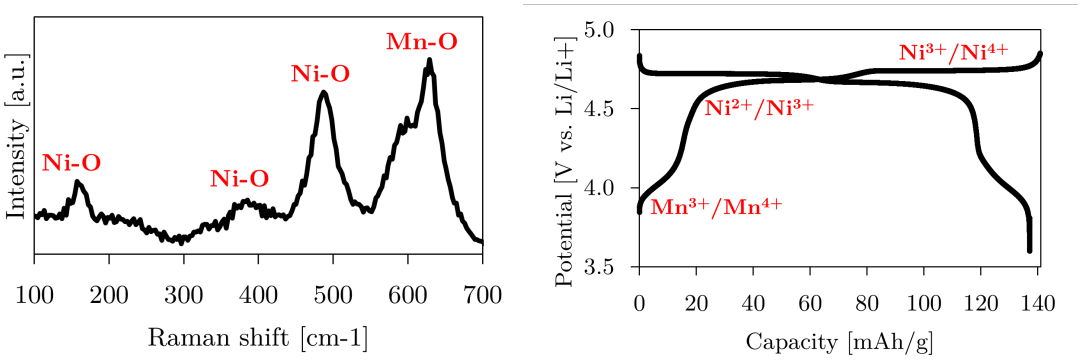

(a) **(b)**

Figure 2.3.3: (a) Raman spectrum of disordered LNMO with the space group $Fd\bar{3}m$, with the chemical origin of the peaks [21] and (b) potential curve during charge and discharge with plateaus of the redox couples [5].

2.3.1.2 Synthesis

The electrochemical behaviour of LNMO is highly influenced by the possible structure of LNMO, which is dependent on the synthesis procedure [24]. Solid-state synthesis is the most common method of fabrication. It involves the stochiometric mixture of initial materials through either ground or ball milling, followed

by heat treatment. Wet synthesis methods involve the sol-gel method and co-precipitation. It allows the controls of parameters such as size, morphology, and uniformity of the particles. When using a wet synthesis procedure, the purity of the final LNMO material is determined by that of the initial materials, the temperature of the calcination and the duration of the experiment. The impurity phases in LNMO synthesised through wet methods includes NiO and $Li_xNi_{1-x}O$. Such impurities are formed because of the oxygen loss at elevated temperatures. The molten salt method has been introduced as an alternative to wet synthesis to synthesise LNMO of high purity. In this method, a salt with a low melting point is used to exploit the high diffusion rates between the initial reaction components and form a single-phase powder [19].

2.3.1.3 Degradation

One of the reasons LNMO still is not commercialised is because of the severe degradation occurring during operation [25]. The three major degradation factors of LNMO are the electrolyte decomposition, the dissolution of the transition metal and the production of gas [19]. Such degradation mechanisms are particularly present in full cells with a graphite anode, as the anode in half cells constantly supplies lithium and thus the negative impact of lithium being immobilised by side reaction is minimized [25].

A general problem in high-voltage LIBs is the decomposition of the electrolyte caused by the high potential. Oxidation and reduction of the solvents in the electrolyte may occur at both the anode and the cathode [25]. The decomposition of the electrolyte can be explained by the self-discharge behaviour of LNMO at high potential caused when the active material is delithiated, which then catalyses the decay of the electrolyte at the cathode-electrolyte interphase (CEI) through oxidation. The deterioration of the electrolyte can further be explained by discussing its thermodynamic stability as the difference between the Fermi energy levels and highest occupied molecular orbital (HOMO)/lowest unoccupied molecular orbital (LUMO). For cathode materials such as LNMO, a Fermi energy level (E_c) lower than the HOMO of the electrolyte promotes electrolyte oxidation, resulting the formation of a CEI layer. In a similar fashion, the high Fermi energy level of the anode material as graphite (E_a) when compared to the LUMO of the electrolyte leads to the reduction of the electrolyte and the formation of a solid-electrolyte interphase (SEI) layer. This situation is sketched in Figure 2.3.4, with a general explanation given in Section 2.5. Even though calculations demonstrate that the solvent should be thermodynamically stable below potentials of 5.5 V vs. Li,

experimental publications show that conventional carbonate-based solvents experience oxidation over 4.5 V, which is probably due to the presence of impurities and additives. Hence, the high operating voltage of 4.7 V causes electrolyte oxidation and the formation of a thick CEI layer [5].

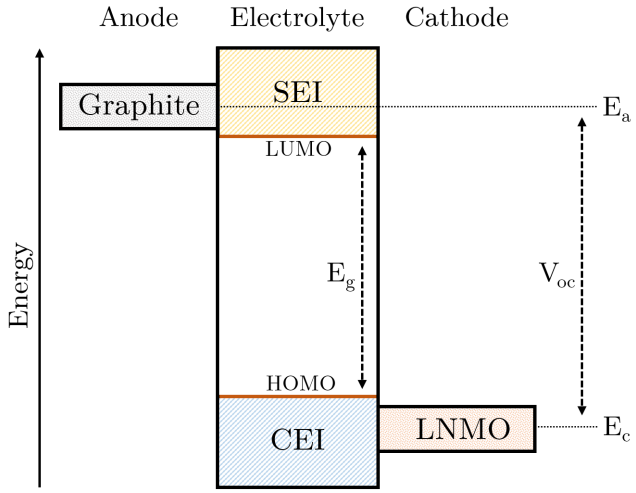

Figure 2.3.4: The event of formation of the CEI layer on the cathode material (LNMO) through electrolyte oxidation and the SEI layer on the anode material (graphite) through electrolyte reduction. In this case, the open circuit potential of the cell, V_{oc}, is larger than the band gap of the electrolyte, E_g.

The effects of the high potential of LNMO on the oxidation of conventional solvents like EC and DEC have been investigated in the literature. It was found that poly(ethylene carbonate) (PEC), an oxidation product of EC, was formed on the surface of LNMO at potentials above 4.7 V vs. Li [26]. In addition, it was reported that the Lewis acid PF_5, which originates from the solute $LiPF_6$, promotes polymerisation of EC into poly(ethylene oxide) (PEO). The decomposition of EC in a system with LNMO and $LiPF_6$ can be summarised by Equation 2.9 [6]:

$$\mathrm{EC} \xrightarrow{\mathrm{LiPF_6}} \mathrm{PEC} \xrightarrow{-\mathrm{CO_2}} \mathrm{PEO}. \tag{2.9}$$

Ethanol (C_2H_6O) has been proposed as a decomposition product of DEC when manganese oxide, potential impurity from the decomposition of LNMO, is present as a catalyst. The chemical reaction is presented in Equation 2.10 [27]:

$$\mathrm{DEC} \xrightarrow[\mathrm{LiPF_6}]{\mathrm{Mn}} \mathrm{C_2H_6O} + \mathrm{CO_2} + \mathrm{C_2H_4}. \tag{2.10}$$

The dissolution of transition metal is another possible cause for the severe capacity fade observed in LNMO full cells. This dissolution is of particular concern for Mn and is a result of the already discussed sintering temperature, where oxygen loss

promotes the reduction of Mn^{4+} to Mn^{3+}. Mn^{3+} can then undergo the reaction presented in Equation 2.11 [5],

$$2\,Mn^{3+} \longrightarrow Mn^{4+} + Mn^{2+}, \tag{2.11}$$

where the Mn^{2+} is soluble in the electrolyte. Pieczonka et al. have studied the behaviour of transition metal dissolution in LNMO full cells by varying conditions such as temperature, SOC and storage time [6]. They found that the decomposition of the electrolyte and the formation of HF may accelerate the dissolution of Ni and Mn from LNMO, which will lead to the formation of several products on the surface of the electrode. These degradation products can be LiF, MnF_2, NiF_2 and polymerised organic compounds, where their formation is described in Equation 2.12, contributing to a higher impedance of the cell:

$$\begin{aligned} &2\,LiNi_{0.5}Mn_{1.5}O_4 + 4\,H^+ + 4\,F^- \\ &\qquad\longrightarrow 3\,Ni_{0.25}Mn_{0.75}O_2 + 0.25\,NiF_2 + 0.75\,MnF_2 + 2\,LiF + 2\,H_2O. \end{aligned} \tag{2.12}$$

The soluble Mn^{2+} ions may be reduced on the graphite surface of the anode and consume active lithium ions. This phenomenon is expressed by Equation 2.13:

$$Mn^{2+} + 2\,LiC_6 \longrightarrow Mn + 2\,Li^+ + \text{graphite}. \tag{2.13}$$

Furthermore, the reduced Mn will catalyse electrolyte reduction reactions, causing severe capacity fade and degradation of the cell. Pieczonka et al. findings also imply that the dissolution of both Mn and Ni increases with storage time due to chemical degradation, temperature, and SOC. The fact that the metal dissolution increases with the SOC was not expected, as the discharged state of the material usually holds lower valences of the metals [24].

Gas gas production is considered another source of degradation in high-voltage LIBs. The gaseous compounds formed by the degradation of the electrolyte can lead to the swelling of prismatic and pouch cells. These gases are usually made of light hydrocarbons, CO_2 and H_2 [19].

2.4 Anode Materials

When a LIB is charging, the anode stores the Li-ions coming from the cathode through electrochemical reduction. The ideal anode material should fulfil the following characteristics [2]:

- Being light and able to fit many Li-ions to reach a high gravimetric capacity.
- Having a low redox potential compared to Li/Li^+ to sustain a high cell potential.
- Having both good electric and ionic conductivity to provide fast Li-ion and electron transport and enhance the power density.
- Not getting dissolved by the solvent in the electrolyte and being inert to lithium salt.
- Being safe to use, particularly avoid thermal runaway.
- Being low cost and environmentally friendly.

Whereas traditional cathode materials can have various structures and compositions, graphite has been used as an anode material for decades without many derivations [28]. In 1976, Besenhard and Eichinger introduced graphite as a possible anode material when they observed its behaviour with the reversible intercalation of Li-ions [29]. Later, the formation of a solid-electrolyte interphase (SEI) layer on the anode during the initial cycles, often referred to as the formation cycles, was discovered. The SEI layer behaves as a passivating layer between the electrode and the electrolyte and prevent uncontrolled intercalation of the solvent, in addition to conducting Li-ions. The following features are required for the SEI layer [2]:

- Exhibiting mechanical stability in case of electrode volume expansion during cycling.
- Ensuring rapid lithium-ion transfer between the electrolyte and the electrode.
- Offering adequate ionic conductivity in the temperature interval from -40 °C to 60 °C.
- Act electronically insulating.

Li-ions intercalate between the graphite layers to form LiC_6 when charging, as illustrated in Figure 2.1.1. The theoretical capacity is significantly higher than the corresponding values of the cathode materials, presented in Figure 2.3.1, with graphite's 372 mAh/g [2]. Nevertheless, its gravimetric capacity is also acting as the material's limiting factor, which has led to the target of improving the capacity by introducing other materials.

A possible replacement for graphite as anode material is silicon, which has been given significant focus in recent years. While graphite is limited in capacity, silicon, through $Li_{22}S_5$, can have high gravimetric and volumetric capacity of 4200 mAh/g and 9786 mAh/cm^3, respectively. The potential of silicon vs Li/Li$^+$ is slightly higher than that of graphite. Also, the material has a low cost and is highly abundant. Still, silicon faces some challenges, the most significant being the volume expansion, as silicon can expand up to 400% during charge and discharge, which will lead to poor cycle life and irreversible capacity reduction. Nanostructured silicon has received attention as a possible solution to this concern, as silicon nanowires, nanotubes and nanospheres have proven to tackle the volume expansion issue [28].

$Li_4Ti_5O_{12}$ (LTO) is another anode material which has been commercialised [2]. LTO is used in high power batteries, where nano materials are utilised to ensure more rapid charge time compared to traditional LIBs [30]. Anode materials based on titanium oxides, such as LTO, offer improved safety, lower price, and are less toxic. LTO is also not concerned by the issues related to volume expansion that can be observed for silicon-based materials. However, LTO is challenged by its low theoretical capacity of 175 mAh/g and low electronic conductivity of 10^{-13} S/cm [28].

2.5 Electrolyte

The role of the electrolyte in LIBs is to ensure conduction of lithium ions between the two electrodes. The choice of electrolyte is mostly influenced by the nature of the electrode material. The electrolyte is essential regarding the formation of steady SEI and CEI layer. They can be seen as an intimate coating layers formed by the electrolyte degradation [31]. An optimal electrolyte should have the following properties [2]:

- Offering a large phase stability window, so neither vaporisation nor crystallisation take place.
- Being inflammable.
- Having a wide electrochemical stability window.
- Having good ionic conductivity and poor electrical conductivity.
- Being non-toxic.

- Consisting of abundant materials.
- Not lead to corrosion of the components in the cell.
- Being environmentally friendly to use.
- Resist thermal, electrical, and mechanical abuse.
- Having good wetting properties towards the electrodes.

As previously indicated in Figure 2.3.4, the thermodynamic stability of an electrolyte is governed by the difference between the Fermi energy of the anode (E_a) and the cathode (E_c), and the HOMO/LUMO of the electrolyte. The electrolyte possesses a band gap (E_g), which expresses the difference between the energy of HOMO and LUMO. A general requirement of thermodynamic stability is that the energies of the electrodes, E_a and E_c, are in the electrolyte window and thus limit the open circuit voltage (V_{oc}). This can be expressed in Equation 2.14 [2]:

$$eV_{oc} = E_c - E_a \geq E_g, \tag{2.14}$$

where e indicates the elementary electronic charge.

An electrolyte is based on several components to satisfy as many of the listed requirements as possible. Overall, an electrolyte is composed of a solvent, a solute, and additives. Conventional electrolytes are nonaqueous aprotic, but ionic liquids have recently received attention for the use in future LIBs [32].

2.5.1 Nonaqueous Aprotic Electrolytes

2.5.1.1 Solvents

Nonaqueous aprotic electrolytes are often used due to the highly reactive environment of the electrodes. Protic solvents react electrochemically at 2 to 4 V vs Li/Li^+, hence in the same potential window that a LIB operates in, making them unsuitable for battery fabrication. An adequate solvent should have the following characteristics [32]:

- Having a high dielectric constant so the solvent is capable of dissolving salts at sufficient concentrations.
- Having a high fluidity and low viscosity to facilitate the ion transport.
- Not reacting with the other components in the cell.

- Having good SEI-forming properties.
- Maintaining liquid state at high and low temperatures.
- Being safe, non-toxic, and low cost.

The commonly used solvents are composed of organic carbonates, esters, and ethers, as they include polar groups and can dissolve salts at sufficient concentrations. A typical solvent system uses a 1:1 volumetric ratio of the cyclic carbonate ethylene carbonate (EC) and the linear carbonate dimethyl carbonate (DMC). In this mixture, EC contributes with high anodic stability on the cathode surface and dissolves the solutes, while DMC leads to a low viscosity [32].

2.5.1.2 Solutes

In a LIB, the solute in the electrolyte is often a lithium salt, selected because of its suitability with the electrodes. While the range of solvents is large, there are less different solutes available commercially. The characteristics important for an optimal solute are [32]:

- Being capable of complete dissociation in the solvent at strong concentrations.
- Having sufficient mobility for the lithium cation.
- Stable anion, meaning that it does not decompose due to the strong oxidation reactions at the cathode, and also does not react with the solvent.
- No reaction between the cation/anion and the cell components.
- Having good SEI forming properties.
- Being non-toxic.
- Resistant to thermal mistreatment.

The majority of lithium-based solutes fail to dissolve in low-dielectric solvents. This can be explained by the small radius of the lithium-ion, which makes solutes as lithium oxides and halides impossible candidates as solutes. The solutes that can fulfil this desired characteristic are generally containing complex anions, such as lithium hexafluorophosphate ($LiPF_6$). This salt is composed of the Lewis acid PF_5 which has complexed the anion F^-, as shown in Figure 2.5.1a. Since its introduction in the late 1960s, it has been the dominating solute in LIBs [32].

Despite that, $LiPF_6$-based electrolytes have specific issues regarding thermal stability. When increasing the temperature, $LiPF_6$ may react with small amounts of both water and alcohols, which will lead to the formation of hydrofluoric acid (HF). This acid degrades the LIB and is a safety issue [33].

Initially, PF_5 is formed as an equilibrium product of $LiPF_6$, which is given in Equation 2.15 [33]:

$$LiPF_6 \rightleftharpoons LiF + PF_5. \tag{2.15}$$

Next, PF_5 will face hydrolysis when trace elements of water are present to form HF, as shown in equation 2.16 [33]:

$$PF_5 + H_2O \longrightarrow POF_3 + 2\,HF. \tag{2.16}$$

The following reactions will be further derived from POF_3, presented in Equation 2.17-2.18 [6]:

$$POF_3 + 2\,xLi^+ + 2\,xe^- \longrightarrow Li_xPF_{3-x}O + xLiF, \tag{2.17}$$

$$POF_3 + 3\,H_2O \longrightarrow PO_4H_3 + 3\,HF. \tag{2.18}$$

Lithium bis(fluorosulfonyl)imide (LiFSI), shown in Figure 2.5.1b, is a promising solute for use in LIBs and is anticipated to replace $LiPF_6$ in the next generation of electrolytes. LiFSI has a significantly high decomposition temperature above 200 °C, in comparison to 60 °C of $LiPF_6$. Furthermore, LiFSI does not have the same hydrolysis challenge leading to the formation of HF, as it is more resistant to moisture, and it possesses better ionic transport properties. Still, LiFSI is can cause serious corrosion of the aluminium current collector, since the absence of HF leads to the lack of a passivating layer, making the aluminium more prone to corrosion [34].

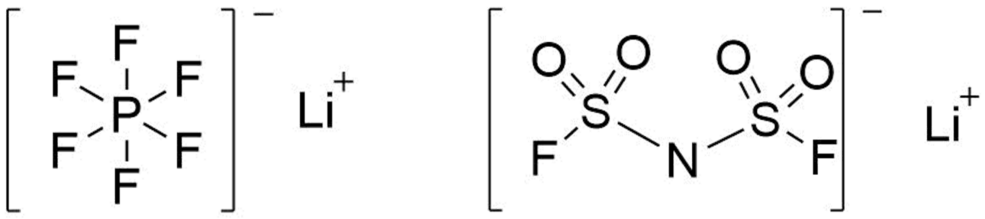

(a) **(b)**

Figure 2.5.1: Structural formulas of (a) $LiPF_6$ and (b) LiFSI.

2.5.1.3 Additives

Additives are added to the electrolyte to enhance the cell performance in a cost-effective way. They also give rise to advantages such as better battery safety with the reduction of flammability, the overcharge conditions are enhanced, and the battery operation is shut down in the event of mistreatment. The amount in the electrolyte is commonly limited to 5 vol-/wt-%. An ideal additive should possess these requirements to enhance the cell performance [35]:

- Facilitate the SEI layer formation on the anode surface.
- Reduce the irreversible capacity.
- Minimise gas formation through long-term cycling and SEI layer formation.
- Enhance the thermal stability of the electrolyte.
- Avoid cathode dissolution and overcharge.
- Improve the electrolyte properties, such as ionic conductivity, fluidity, and wetting behaviour in combination with the separator.

Lithium bis(oxalato)borate (LiBOB) is unique in improving several aspects of a LIB's performance. It has been established that LiBOB contributes to and stabilises the SEI, decreases cathode dissolution, deliver great overcharge resistance, and enables aluminium passivation in the electrolyte. Lithium difluoro(oxalato)borate (LiDFOB) is considered to share many of LiBOB's functions. Yet, several times, the use of additives will also give rise to disadvantageous effects. For instance, using the conventional additive vinylene carbonate (VC) is beneficial for forming a stable SEI layer. Still, too much will result in low cycling efficiency and a high self-discharge rate [35].

2.5.2 Ionic Liquids

A new group of liquids that has gained growing interest lately are salts that are liquid at ambient operating temperatures. These are typically called room-temperature ionic liquids (RTIL) [36]. The low melting temperature is because the ionic liquids consist of large organic cations and organic, or inorganic, anions, with weak ionic forces [37]. RTILs are very relevant for LIBs because they provide better safety than conventional nonaqueous aprotic electrolytes, while offering high thermal and electrochemical stability, ranging from 2 to 6 V [7]. The general characteristics of RTILs are [38]:

- Being not flammable.
- Having a low vapour pressure.
- Being hardly toxic.
- Having a broad potential window, providing good electrochemical stability.
- Having a good thermal stability.
- Having a tolerable conductivity.
- Being compatible with anodes and cathodes during charge/discharge.

However, ionic liquids possess some drawbacks, such as high cost and viscosity, and low conductivity at low temperatures. The wetting conditions will be poor because the contact angle of ionic liquids is often high with certain electrode materials [2].

There is a vast amount of RTILs available, with different combinations of cations and anions. Earlier research has focused on cations based on cyclic ammonium, such as pyrrolidnium [39]. In the search of electrolytes which improve the disadvantageous characteristics of the more common RTILs, as high viscosity and low conductivity, investigations of new ionic liquids based on a phosphonium cation ($P_{111i4}{}^{+}$) have been conducted [39]. An example of an RTIL where such cation has been combined with the anion FSI^{-} is $P_{111i4}FSI$, which in combination with the salt LiFSI showed promising properties, such as enhanced transport properties and a broader electrochemical window, making it adapted for usage with high-voltage electrodes, such as LNMO [8]. The structural formula of $P_{111i4}FSI$ is presented in Figure 2.5.2.

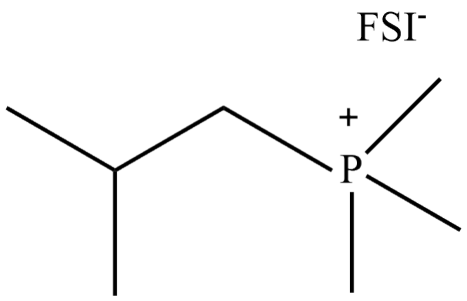

Figure 2.5.2: Structural formula of $P_{111i4}FSI$.

The cycling performance is dependent on the concentration of lithium salt available in the electrolyte. There is a trade off in obtaining the right concentration of the lithium salt, as a higher salt concentration will lead to higher viscosity and, therefore, lower conductivity, but also increases the amount of lithium cations in the electrolyte, which is beneficial [8]. Forsyth et al. have studied the physicochemical properties and electrochemical performance of phosphonium-based RTILs in combination with high voltage NMC cathode, where the concentration of LiFSI in $P_{111i4FSI}$ has exceeded 50 mol-% [8]. It was observed that, although the viscosity increased and the conductivity decreased, the metal ion transference number was higher at elevated concentrations of LiFSI. Also, significantly improvements in electrochemical stability and rate performance were discovered for highly concentrated RTIL when compared to a conventional carbonate-based electrolyte (1 M $LiPF_6$ in EC/DMC). More specifically, the cycling performance of the highly concentrated RTIL was superior at medium rates as C/5, ensuring a better charge/discharge capacity. The discharge capacities were equivalent at more rapid discharge rates (1C and 2C). At even higher rates (up to 4C), the highly concentrated RTIL cell showed a lower discharge capacity than that of the cell using the carbonate electrolyte [8].

Limited investigations have been conducted on combining high-voltage cathodes like LNMO with $P_{111i4}FSI$ are limited. As an exception, Salem et al. [40] have studied $P_{111i4}FSI$ with 0.5 M $LiPF_6$ in combination with different electrode materials, including LNMO. Mixing the RTIL with $LiPF_6$ increased the viscosity which decreased the conductivity and improved the electrochemical stability of the cathode. The RTIL electrolyte performed well and was comparable with conventional electrolytes in half cells with LFP at both slow and fast rates. It was predicted that the wide electrochemical stability window of the RTIL would make it a successful option for use with the high-voltage cathode LNMO. However, LNMO half cells with 0.5 M $LiPF_6$ in $P_{111i4}FSI$ and other phosphonium-based RTILs, did

not produce any capacity at all. A possible reason for this malfunction is the RTIL's reactivity towards the cations present at the surface of LNMO. Chemical side reactions may occur, preventing the formation of a stable CEI layer. This passivation layer improves the cathode performance and is available when using carbonate-based electrolytes [41]. Thus, adding EC as a co-solvent is proposed to avoid reactions between the RTIL and the cathode surface through the development of such CEI layer [40].

2.6 Separators

As previously mentioned, separators are essential in LIBs as they hinder physical contact between the anode and the cathode. A separator needs to be porous to maintain a flow of ions and ensure good absorption of the electrolyte, while behaving as an electrical insulator to avoid electronic flow that may cause short-circuiting of the cell [2]. Mainly, the separator is a microporous layer made of either a polymeric membrane or a non-woven fabric mat. It should be both chemically and electrochemically steady with the electrolyte and the anode/cathode and resist the high mechanical tension that occurs during the assembly of the LIBs. Since the separator adds electrical resistance and occupies the sparse space of a LIB, it influences the battery performance, such as energy and power density, cycle life and safety. To ensure a good safety, the separator needs to be able to shut the battery cell down if overheating happens, for instance, during short-circuiting. Specifically, this function can be obtained through the multilayer design, where one layer may melt and thus block the pores beneath the thermal runaway temperature. The characteristics of separators in LIBs can be summarised as [42]:

- When fully charged, the separator must be chemically stable towards the electrolyte and the anode/cathode, particularly under heavily reductive/oxidative conditions

- The thickness should be as small as possible to secure high energy and power densities, meanwhile not sacrificing strength or safety.

- Suitable porosity to hold an adequate amount of electrolyte and ensure high ionic conductivity (typically a porosity of 40%).

- A pore size which is smaller than the particle size of the electrode components.

- A uniform permeability is essential for the cycle life, and imbalance will lead to differences in the current density distribution throughout the separator, encouraging dendrite formation.
- The separator needs to be mechanically strong to resist tension during assembly.
- The separator should be properly wet when in contact with the electrolyte.
- The dimensional stability of the separator must be good over a broad temperature range, and thermal shrinkage should be avoided.
- The separator must be able to shutdown at a temperature lower than the thermal runaway while maintaining the separation of the electrodes.
- The manufacturing process must be cost-effective and evaluated with the other characteristics.

Generally, separators can be divided into microporous polymer membranes, non-woven fabric mats and inorganic composite membranes, where the first group dominates LIBs. This type of membrane is mostly made of semi-crystalline polyolefin materials, such as polyethylene (PE), polypropylene (PP) and combinations of these materials. An example of such a combination is Celgard 2325 with a PP-PE-PP trilayer with a thickness of 25 μm. This trilayer structure follows a shutdown temperature of approximately 130 °C, as this is the melting point of PE. At this temperature, PE will fill the pores of the PP and thus increase the electrical resistance significantly, leading to a shut down of the operation of the battery. PP has a melting temperature of 165 °C, providing a buffer of 35 °C, which usually is enough for LIBs, although it does not protect against more serious damage [42].

Another type of separator is Viledon, supplied by Freudenberg, which consists of polymeric non-woven polyethylene terephthalate (PET) combined with a ceramic impregnation of Al_2O_3 [43]. This separator has not been investigated extensively but is similar to the more known separator series Separion, developed by Degussa. This series of separators were designed to face the problems of composite separators not being mechanically sturdy enough for battery assembly. In Separion, Degussa has combined polymeric non-woven PET with different ceramic materials in the form of nanoparticles, such as alumina, silica, zirconia, or a mixture. The result is a flexible perforated non-woven mat impregnated with a ceramic coating on both sides. An inorganic binder maintains the beneficial hydrophilic characteristic of ceramic materials. Compared to well-known separators, such as Celgard,

Separion shows great wettability, good permeability, high melting temperature and minor shrinkage, even at elevated temperatures [42].

Glass fibre membranes provide a very porous structure and great wettability, which may contribute to a high electrolyte uptake and, thus, high ionic conductivity [44]. An example of such separator is the binder-free Whatman glass microfiber filter from Cytiva, which may be used for several applications. Their glass fibre filter with grade GF/A consists of borosilicate glass and has a thickness of 260 μm, which implies a thickness more than 10 times larger than that of the Celgard 2325 separator. The thickness also limits the use in conventional LIBs and make them more suitable for lab-scale batteries.

2.7 Characterisation Methods

2.7.1 Galvanostatic Cycling

Galvanostatic cycling is a technique that aims to decide the specific capacity of a particular electrode material. During galvanostatic cycling, the voltage is recorded as a function of time while a direct and constant current is applied to the battery cell. This gives the opportunity to demonstrate the potentials of the oxidation/reduction reactions occurring in the electrode material during charge and discharge. Frequently, half cells configurations are used, indicating that Li is used as the counter electrode, and the cell potential is given with respect to Li/Li^+. Among the data that can be acquired from this technique is the reversibility of the relevant reactions, capacity, coloumbic efficiency, long-term cycling performance and phase changes visible at distinct potential plateaus. Constant current constant voltage (CCCV) is a common charging method for secondary batteries. Through CCCV, the operation will switch from charging with constant current to charging with constant potential depending on the potential of the cell [45].

2.7.2 Electrochemical Impedance Spectroscopy

Electrochemical impedance spectroscopy (EIS) provides both kinetic and mechanistic data for different electrochemical systems and is based on the perturbation of a system experiences in either equilibrium or in a steady state through the implementation of a sinusoidal signal. The signal may be either ac voltage (PEIS) or ac current (GEIS) over a broad range of frequencies. The sinusoidal response, either current or voltage, respectively, is monitored towards the applied perturbation [46].

In battery-related EIS measurements, lithium metal is used as a reference electrode. The EIS is conducted with an impedance/gain-phase analyser connected to a battery tester. The frequency range is typically from 350 kHz to 3 mHz, together with an ac signal amplitude of approximately 5 mV [2]. A common impedance spectrum is a Nyquist plot, where the x-axis expresses the real impedance, while the y-axis expresses the imaginary impedance. The frequency is not stated but is highest on the left side of the plot, and then becomes lower towards the right side [47]. In such a plot, the typical behaviour consists of a semicircle in the high-frequency region, followed by a linear tendency in the low-frequency region due to Warbug diffusion. The cell's impedance is given by a complex quantity, expressed in Equation 2.19 [2]:

$$Z_c = Re(Z_c) + Im(Z_c), \tag{2.19}$$

where $Re(Z_c)$ can further be expressed as the sum of the internal resistance in the cell in addition to the Warbug contribution from the diffusive process, shown in Equation 2.20 [2]:

$$Re(Z_c) = R_1 + R_2 + \frac{\sigma}{\sqrt{\omega}}, \tag{2.20}$$

where R_1 and R_2 are the charge transfer resistances of the two electrodes, and ω represents the Warbug coefficient.

In a Nyquist plot, the ohmic resistance of a LIB is indicated by the intersection between the spectrum and the x-axis, meaning the real part. It is mainly composed of the resistance of the electrolyte, but is also influenced by the active material, separator, current collectors and other points of contact in the cell. The electrolyte decomposition has a substantial role on the LIB impedance, where electrolyte loss due to reactions with the anode/cathode will increase the resistance of the electrolyte, caused by reduction in the mobility of lithium ions. Therefore, an increase in ohmic resistance will be followed by a reduction in conductivity [47].

2.7.3 Raman Spectroscopy

Raman spectroscopy is a vibrational spectroscopy method utilised to study the structural properties of a sample's surface. The technique is built upon the principle of inelastic scattering of light, which relates to the transitions between the vibrational energy levels of a compound. During exposure to electromagnetic radiation to a molecule, absorption, transmission, and scattering may arise. Ab-

sorption and transmission lead to radiation in the form of the infrared spectrum (IR), while scattering generates the Raman spectrum. Contrary to IR, Raman scattering depends on the vibration of induced dipole moment, indicating that non-polar bonds give rise to stronger signals than polar bonds [48].

Raman imaging spectroscopy combines a microscope with a Raman spectrometer based on a laser energy source. The photon energy of such a laser is usually in the span between the UV and the IR region [49]. The working principle can be described as scattered photons being measured because electrons from the sample move into a virtual state when monochromatic light is focused on the sample surface. The scattered radiation can further be split into Rayleigh, Stokes, and anti-Stokes, where there mainly Stokes will be present since the spectroscopy technique is executed at room temperature and thus the compound is in its fundamental state [48].

For comparing the peaks in a Raman spectrum, there are mainly two different procedures of calculating the ratio: integrated area ratio (A_a/A_b) or intensity ratio (I_a/I_b), where a and b represent two different peaks. The latter procedure involving intensity ratio is however recommended over integrated area ratio [50].

2.7.4 Scanning Electron Microscopy

Scanning electron microscopy (SEM) is a helpful apparatus used to characterise the surface of heterogeneous compounds at small scales. When the SEM is operated, the sample gets irradiated with a focused electron beam, generating various signals that the microscope can detect. For instance, such signals are secondary electrons (SE), which provides details about the topography, backscattered electrons (BSE), which shows the chemical composition, Auger electrons and X-ray radiation [51].

Energy dispersive X-ray spectrometry (EDS) is a technique for chemical analysis based on distinct X-rays, which means the interaction between approaching electrons and interior orbital electrons from the sample's atoms. The presence of such material can be confirmed because the wavelength of a specific radiation is specified for a particular atom number. Therefore, the spectra obtained from the EDS analysis can be utilised to determine the chemical composition quantitatively and qualitatively [51].

Chapter 3

Methods

3.1 LNMO Electrode Fabrication

LNMO electrodes were fabricated both with and without carbon. The solids were first added in a zirconia jar and mixed for 2 minutes at 25 Hz with Retsch Mixer MM400. Then, the binder solution and, if appropriate, extra solvent was added to the jar to achieve the proper viscosity, together with three zirconia balls. The slurry was mixed at 25 Hz for 30 minutes. After the mixing, the slurry was distributed on an aluminium foil and tape cast with RK K Control Coater 101 with a bar of a particular gap size. The cast was then dried at 60 °C overnight. Finally, the cast was calendered with MSK-HPR-MR100A to achieve a 10 % decrease in the thickness of the active material. The final electrodes were cut out from the calendered cast with a diameter of 12 mm and dried overnight at 120 °C under vacuum.

3.1.1 LNMO with Carbon

For the LNMO electrodes with carbon, the slurry was made from 90 wt-% LNMO ($LiNi_{0.5}Mn_{1.5}O_4$, Haldor Topsøe), 5 wt-% conductive additive carbon black (CNERGY SUPER C65) and 5% polyvinylidene fluoride (PVDF, Astrup) in n-methyl-2-pyrrolidone (NMP, Alfa Aesar) solution. The accurate formula is presented in Table B.1, with a ratio between solids and NMP of 1:2, respectively. Double-sided carbon-coated aluminium foil and a 100 µm bar were used for the tape casting.

3.1.2 LNMO without Carbon

For the LNMO electrodes without carbon, the slurry was made from 95 wt-% LNMO ($LiNi_{0.5}Mn_{1.5}O_4$, Haldor Topsøe) and 5% polyvinylidene fluoride (PVDF, Astrup) in n-methyl-2-pyrrolidone (NMP, Alfa Aesar) solution. Several attempts

were made to optimise the thickness and viscosity, and the different formulas are given in Table B.1 to B.4. No additional NMP resulted in the best viscosity. Aluminium foil without carbon coating and different gap sizes were used for the tape casting.

3.2 Electrolyte Preparation

The ionic liquid consisting of the liquid trimethyl(isobutyl)phosphonium bis(fluorosulfonyl)imide ($P_{111i4}FSI$, IoLiTec) and the salt lithium bis(fluorosulfonyl)imide (LiFSI, Solvionic) was mixed and prepared in a glove box with Ar atmosphere. Different concentrations of LiFSI were dissolved in $P_{111i4}FSI$ with a magnetic stirrer for a couple of hours, with a total weight of 5 g of each solution. The exact amounts of the components are presented in Table 3.2.1.

Table 3.2.1: Amounts of the components in the electrolytes.

Concentration of LiFSI [mol/kg]	$P_{111i4}FSI$ [g]	LiFSI [g]
0.79	4.2563	0.7417
3	2.1796	2.8155

3.3 Pouch Cell Manufacture and Assembly

The pouch cell comprises four main components, as presented in Figure 3.3.1. The exterior of the pouch cell is a thick polymer laminated Al foil, with rough measures of 12 x 8 cm. A thermoplastic bonding film in the upper part of the inside of the Al foil leaves a small gap at the top. An electrical tape covers this gap and the upper part of the bonding film and is folded on both the inside and the outside of the Al foil. The current collector tabs consist of Al and Cu, forming a triangle toward the cell stack. The pouch cell is then folded as indicated with the dotted line and sealed for 4 seconds at 130 °C with Gelon GN-HS200. The placement of the seal should be on the bonding film but below the electrical tape.

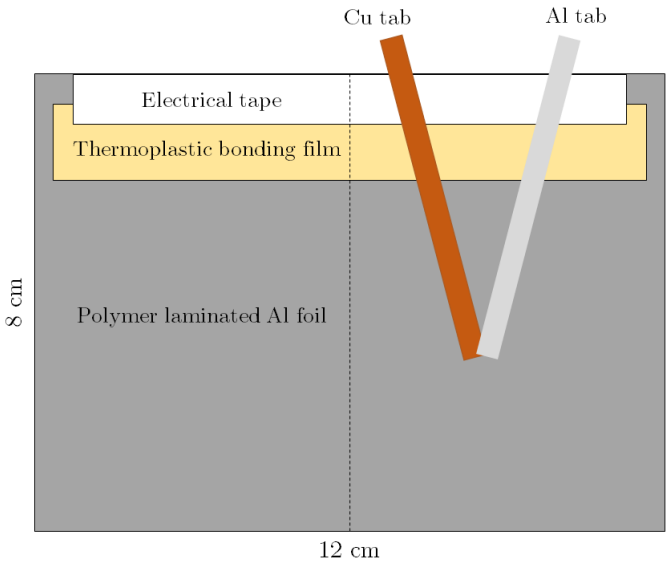

Figure 3.3.1: Overview of the pouch cell manufacturing.

The pouch cell assembly was done through the following method, with certain variations determined by whether a carbonate-based electrolyte or an RTIL was used. The assembly was carried out in a glove box with Ar atmosphere and levels of H_2O and O_2 below 0.1 ppm. After the cell stack was assembled, it was inserted in the pouch cell, where the Li counter electrode was attached to the Cu current collector, and the LNMO backside was attached to the Al current collector. The final seals were made with AudionVac VMS 53, as presented in Figure 3.3.2.

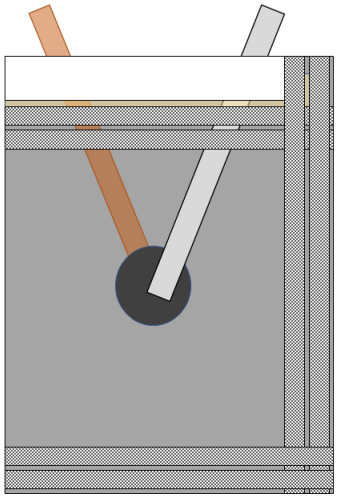

Figure 3.3.2: Sealing positions on the pouch cell.

3.3.1 LNMO/Li/$LiPF_6$

The stack of the reference cells is made up of Li metal as a counter electrode, Celgard 2325 separator, LNMO electrode and 1 M $LiPF_6$ in 1:1 EC:DEC (v/v) (Sigma Aldrich) as an electrolyte, as illustrated in Figure 3.3.3. First, a 12 mm Li metal disk was brushed to remove the oxide layer on the surface. Second, 20 µL electrolyte was pipetted out on the Li disk, and the separator was put on top. Additionally 20 µL electrolyte was pipetted out on top of the separator. In the end, the LNMO electrode was placed on the top of the cell stack, with its active material fronting the separator.

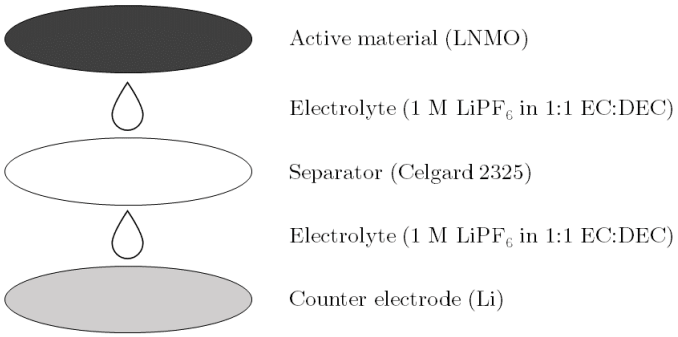

Figure 3.3.3: Cell stack with LNMO/Li/$LiPF_6$.

3.3.2 LNMO/Li/LiFSI in $P_{111i4}FSI$

The stack of the cells with RTIL was made up of Li metal as the counter electrode, two glass fibre (Whatman GF/A) and one non-woven ceramic impregnated PET separator (Freudenberg), LNMO electrode and in total 80 µL of either 0.79 m or 3 m LiFSI in $P_{111i4}FSI$ as the electrolyte, as illustrated in Figure 3.3.4. First, a 12 mm Li metal disk was brushed to remove the oxide layer on the surface. Second, 15 µL electrolyte was pipetted out on the Li disk, and the PET separator was put on top. Additionally 15 µL electrolyte was pipetted out on top of the separator, and a glass fibre separator was placed on top. 35 µL electrolyte was pipetted out on top of the glass fibre separator, and an additional PET separator was put on top. In the end, 15 µL electrolyte was pipetted out on the last PET separator, before the LNMO electrode was placed on the top of the cell stack, with its active material fronting the separator.

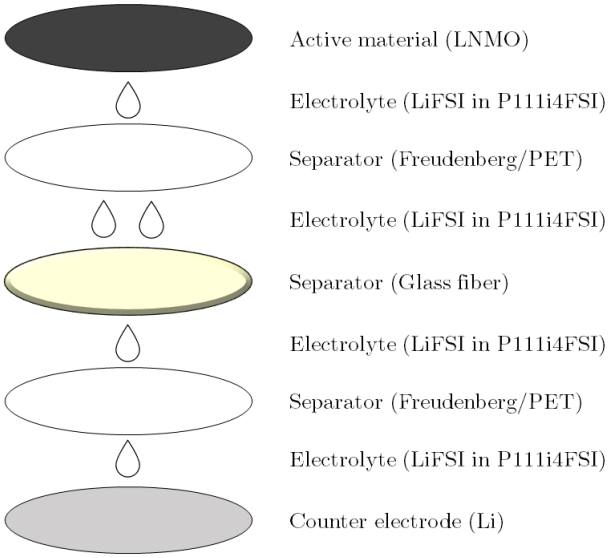

Figure 3.3.4: Cell stack with LNMO/Li/LiFSI in $P_{111i4}FSI$.

3.4 Electrochemical Characterisation

3.4.1 Galvanostatic Cycling

Following the pouch cell assembly, the cells rested for 24 hours at room temperature before the cycling procedure. BioLogic BCS-805 was to cycle all the prepared cells. A single cycling program consisted of 2 C/10 cycles at first, followed by 50 C/2 cycles and finished by 2 C/10 cycles. Such cycling program was repeated consequently until maximum 200 C/2 cycles, regarding the cell's configuration and performance. The voltage limit was 3.6 to 4.85 V. The program is shown in Table 3.4.1:

Table 3.4.1: Galvanostatic cycling program for half-cell configuration with LNMO.

C-rate	Voltage limits [V]	Number of cycles
C/10	3.6-4.85	2
C/2	3.6-4.85	50
C/10	3.6-4.85	2

A rate test was performed to study the difference between the different concentrations of the RTIL to a greater extent. The rate test program is given in Table 3.4.2, where the cells are exposed to both high and low C-rates.

Table 3.4.2: Rate test program.

C-rate	Voltage limits [V]	Number of cycles
C/10	3.6-4.85	5
C/5	3.6-4.85	5
C/2	3.6-4.85	5
1C	3.6-4.85	5
2C	3.6-4.85	5
C/10	3.6-4.85	5

For the cells which consisted of LNMO without carbon, both LP40 and 0.79 m RTIL were evaluated as electrolyte and the cells were cycled very slowly, at a C-rate of C/20.

3.4.2 Electrochemical Impedance Spectroscopy

For the cells where rate test was performed, potentiostatic electrochemical impedance spectroscopy (PEIS) was conducted after completed rate test to measure the resistance of the cells. A Biologic VMP3 potentiostat was used for the measurements, with a frequency from 200 to 1 kHz, 10 points per decade, a sinus amplitude of 5 mV and an average of 5 measures per frequency.

3.5 Post-Mortem Characterisation

3.5.1 Raman Spectroscopy

Pristine and cycled LNMO electrodes were characterised with WITec Alpha 300R for the Raman spectroscopy. A laser with a wavelength of 532 nm and the objective Zeiss LD EC Epiplan-Neofluar Dic with a magnification of 50x was used. The used laser power was 10 mW with 600 g/mm grating, 10 seconds integration time and 6 accumulations.

3.5.2 Scanning Electron Microscopy

Pristine and cycled LNMO electrodes were characterised with FEI Apreo field emission scanning electron microscope. A working distance of 10 mm was used for both imaging and EDS analysis. The standard mode was used for the imaging with the ETD detector, 3 kV accelerating voltage, and 0.10 nA probe current. The

EDS analysis was conducted with an Oxford Xmax EDX system in standard mode with the ETD detector, 15 kV accelerating voltage, and 0.40 nA probe current.

3.6 Summary of Methods

A summary of the method is presented in Figure 3.6.1, and a comprehensive list of all assembled cells is shown in Table C.1.

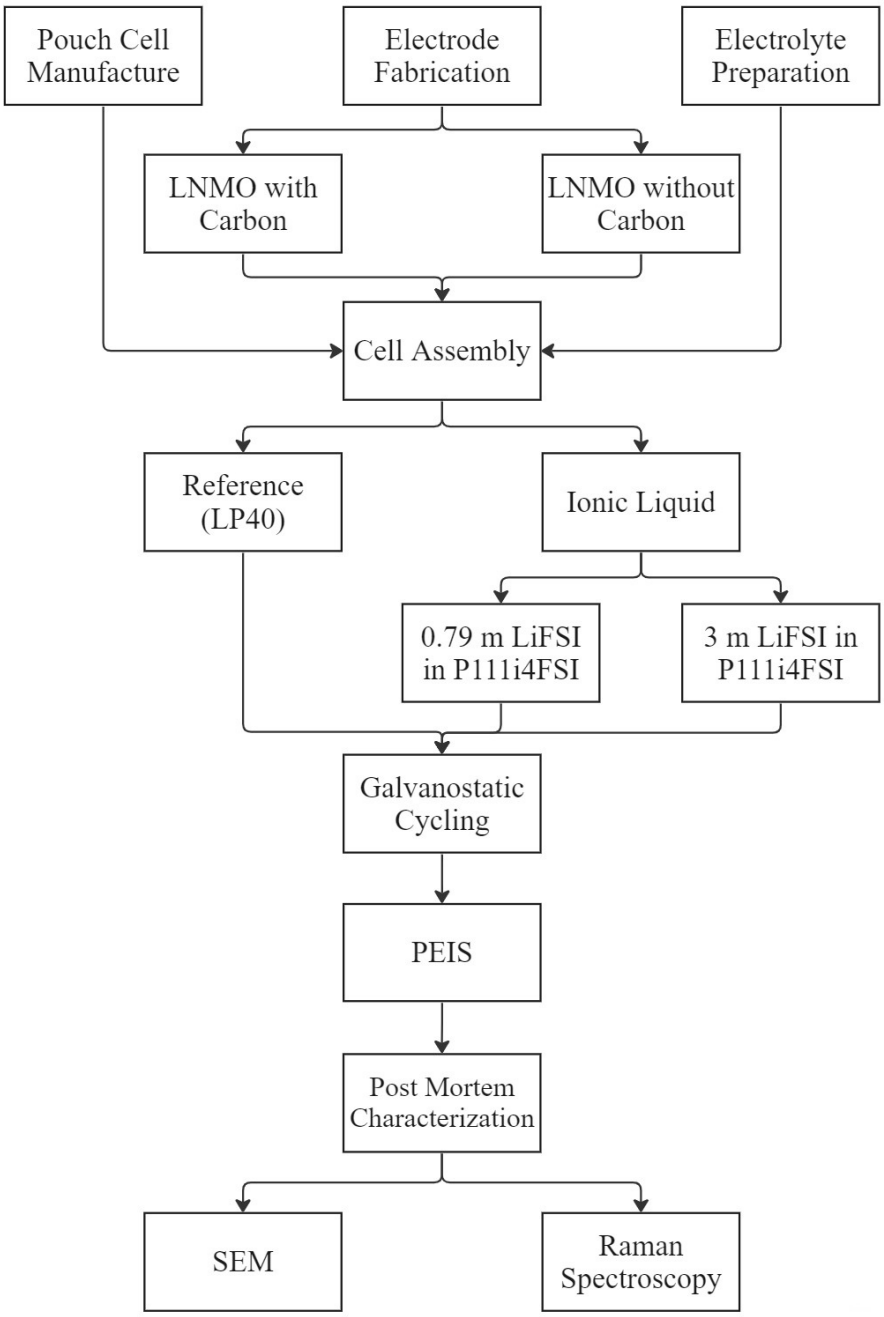

Figure 3.6.1: Flow chart of the methods.

Chapter 4

Results

4.1 Pristine LNMO

Pristine LNMO was fabricated both with and without the conductive additive carbon black, as described in Section 3. However, the majority of the experimental work in this thesis was performed with the conventional LNMO formula, i.e. with added carbon. For later comparison with cycled LNMO electrodes, pristine LNMO was also characterised.

Raman spectroscopy was conducted with the beam being focused on the LNMO particles. The Raman spectrum of LNMO both with and without carbon is presented in Figure 4.1.1 and shows different peaks and the chemical bands. For both types, the distinct peaks of nickel and manganese bands are presents, and LNMO with carbon also shows peaks corresponding to carbon bands.

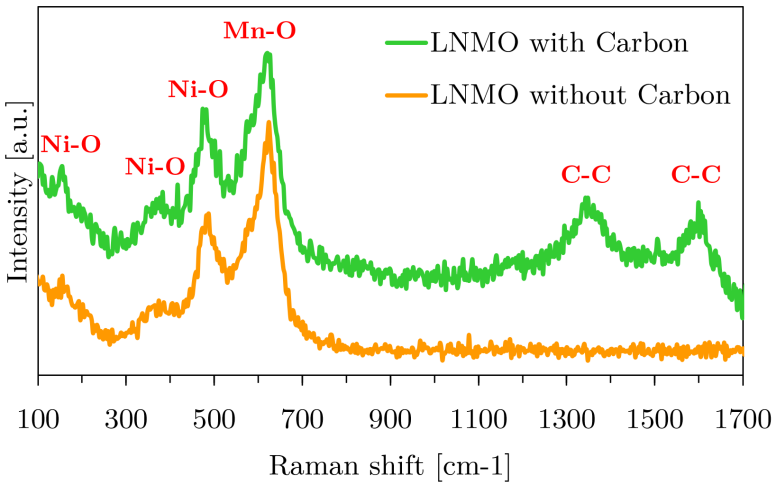

Figure 4.1.1: Raman spectrum of pristine LNMO both with and without carbon, with the chemical bands corresponding to the peaks [21] [52].

The intensity ratios of the pristine materials, both with and without carbon, are given in Table 4.1.1. The ratios are not intended to be compared but are a reference for the cycled electrodes.

Table 4.1.1: Intensity ratio between the highest Ni-O band and the Mn-O band.

Sample	Ratio $\frac{I_{Ni}}{I_{Mn}}$
Pristine LNMO with Carbon	0.86
Pristine LNMO without Carbon	0.76

4.1.1 Pristine LNMO with Carbon

Pristine LNMO with carbon was characterised with SEM, EDS and Raman spectroscopy for reference when comparing the cycled LNMO electrodes. This makes it possible to discuss the degradation of the electrode material after cycling. The SEM images of pristine LNMO with carbon in three magnifications are presented in Figure 4.1.2, which show the characteristic LNMO particles with small triangles on the surface, surrounded by a carbon/binder network.

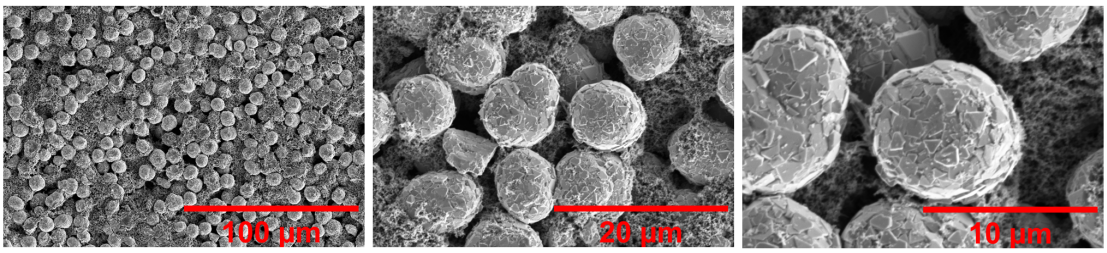

Figure 4.1.2: SEM images of pristine LNMO with carbon at three different magnifications.

The EDS analysis of pristine LNMO with carbon is presented in Figure 4.1.3. The analysis shows a distribution of the elements oxygen, manganese, carbon, nickel and fluorine, in the order from the strongest to the weakest signal. Oxygen, manganese, and nickel have their origin in the LNMO active material, while carbon and fluorine originate from the conductive additive and the binder solution, respectively. The signal of nickel was unexpectedly low in comparison to manganese.

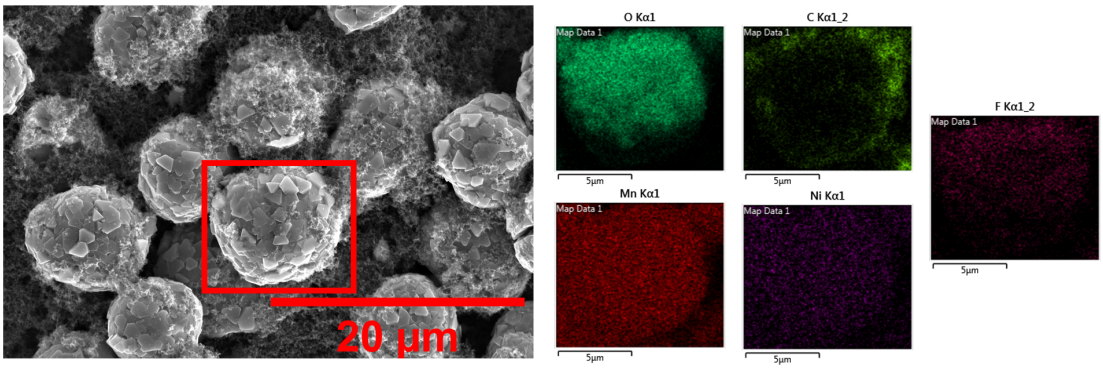

Figure 4.1.3: EDS analysis of pristine LNMO with carbon.

4.1.2 Pristine LNMO without Carbon

Pristine LNMO without carbon was characterised with SEM, EDS and Raman spectroscopy. The objective was to observe the thickness of the electrode (if the electrode was only one LNMO particle thick, as desired), and also act as a reference to cycled LNMO and as a comparison to LNMO with carbon. The fabricated LNMO without carbon resulted in a thickness of approximately 20 μm. SEM images of pristine LNMO without carbon in three magnifications are presented in Figure 4.1.4. The images of the electrode material without carbon show a more bare electrode surface as expected, since no conductive additive is present. It also reveals that the cast was thicker than that of one LNMO particle, not as thin as desired.

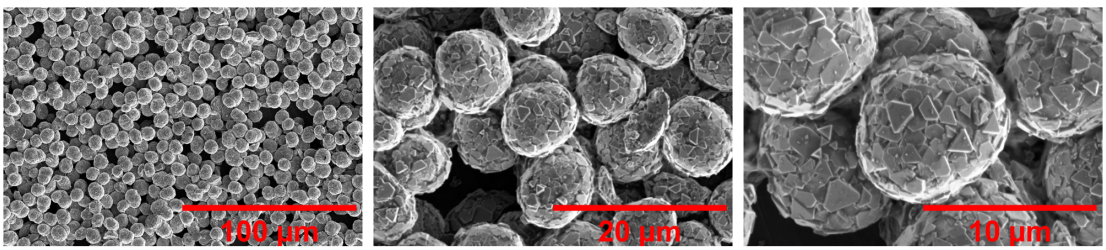

Figure 4.1.4: SEM images of pristine LNMO without carbon at three different magnifications.

The EDS analysis of pristine LNMO without carbon is presented in Figure 4.1.5. The analysis shows a distribution of the elements oxygen, manganese, nickel and fluorine from the strongest to the weakest signal. As with pristine LNMO with carbon, the signal of nickel is also low in this case. As expected, there is no signal for carbon as this is excluded from the electrode slurry. Fluorine has its origin from the binder solution.

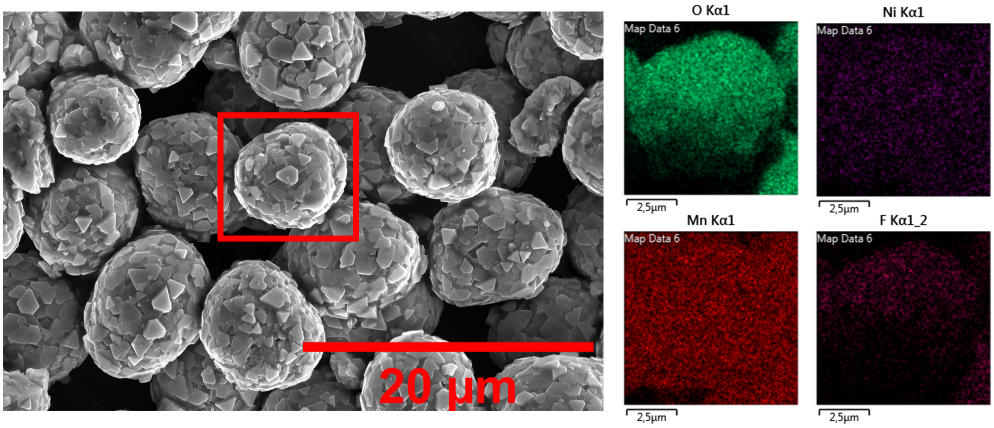

Figure 4.1.5: EDS analysis of pristine LNMO without carbon.

4.2 Electrochemical Comparison of Electrolytes

To study of the effect of different electrolytes in combination with LNMO, galvanostatic cycling data will be presented for the reference electrolyte LP40 (1M $LiPF_6$ in EC/DEC 1:1), as well as 0.79 m RTIL (0.79 m LiFSI in $P_{111i4}FSI$) and 3 m RTIL (3 m LiFSI in $P_{111i4}FSI$), obtained in half cells, as described in Section 3. The basis of the electrochemical experiments, including the galvanostatic cycling program, rate test program and PEIS measurements is given in Section 3.4.

4.2.1 Cycling Data

The discharge capacity and coulombic efficiency of LP40, 0.79 m RTIL and 3 m RTIL over 200 cycles are presented in Figure 4.2.1. For the discharge capacity, shown in Figure 4.2.1a, all electrolytes begin at a similar level but then display different behaviour. LP40 experiences an even fade in discharge capacity from 132 mAh/g to 112 mAh/g, implying a capacity retention of 84.8%. On the contrary to the RTILs, LP40 faces a capacity drop during the C/10 cycles. 0.79 m RTIL fades as LP40 during the first 100 cycles but then seems to fade at a lower rate than LP40. Ending at a discharge capacity identical to LP40 results in a capacity retention of 86.8%. 3 m RTIL undergoes a more rapid decrease than LP40 and 0.79 m RTIL during the first 50 cycles, where the rate appears to stabilise after 100 cycles, similar to the case with 0.79 m RTIL. This gives a capacity retention of 84.0%. The coulombic efficiency presented in Figure 4.2.1b shows that the RTILs possess a significantly higher CE than LP40. Their behaviour is also different, as the CE of LP40 drops when decreasing the C-rate, while the RTILs experience an increase. Overall, LP40 has a CE of 95-96%, while the RTILs have a CE of >99%, and the 3 m RTIL is slightly higher than the 0.79 m RTIL.

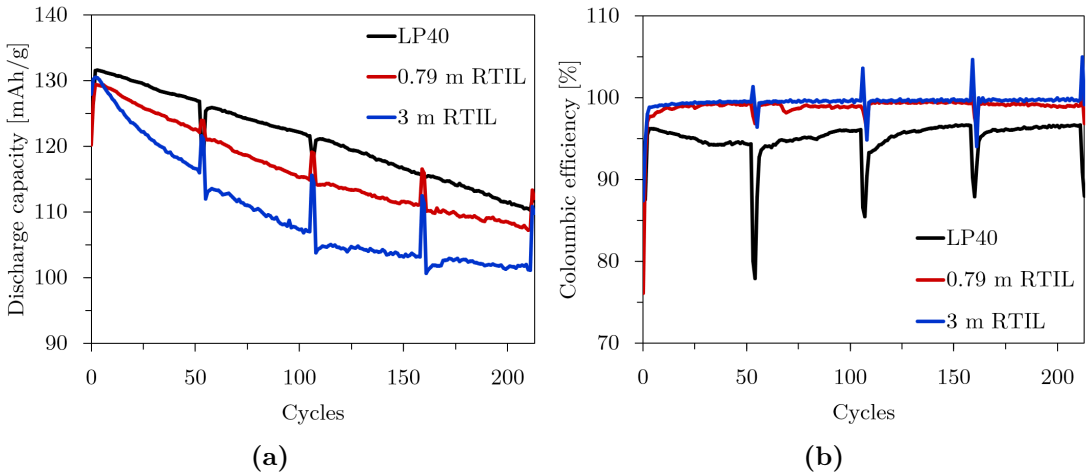

Figure 4.2.1: Comparison of LP40, 0.79 m RTIL and 3 m RTIL during over 200 cycles in terms of (a) discharge capacity and (b) coulombic efficiency, with a general C-rate of C/2 and two C/10 cycles after every 50 C/2 cycles.

Figure 4.2.2 shows the potential profiles throughout 200 cycles for the reference LP40, 0.79 m RTIL and 3 m RTIL. The plotted curves have a C-rate of C/10 and correspond to the cycle succeeding the previous 50 cycles with a C-rate of C/2. "1 cycle" represents the first C/10 cycle in the cycling program. The characteristic potential plateaus are present for all electrolytes and maintain their shape during the cycling interval. A small plateau due to the Mn^{3+}/Mn^{4+} redox couple around 4 V vs Li/Li^+ and two bigger plateaus around 4.6 and 4.8 V vs Li/Li^+ due to the Ni^{2+}/Ni^{3+} and Ni^{3+}/Ni^{4+} redox couples, respectively, can be observed. The most significant difference is the variation in the capacity of the discharge curve, even though their appearance is similar after one cycle. LP40 undergoes a rapid capacity decrease between 1 and 50 cycles and then fades more slowly. The 0.79 m RTIL cell experiences a more even capacity decrease throughout the whole interval, while 3 m RTIL fades rapidly to 100 cycles and then stabilises.

4.2.2 Rate Test

Figure 4.2.3 shows the results from rate test of LP40, 0.79 m RTIL and 3 m RTIL, where the electrodes were cycled five times at increasing C-rates before the test was finished at C/10. The discharge capacity of the electrolytes during the rate test is presented in Figure 4.2.3a. LP40 displays a relatively constant discharge capacity throughout the rate test and performs well also at high C-rates. 0.79 m RTIL starts better than LP40, but the decrease is substantial at elevated C-rates,

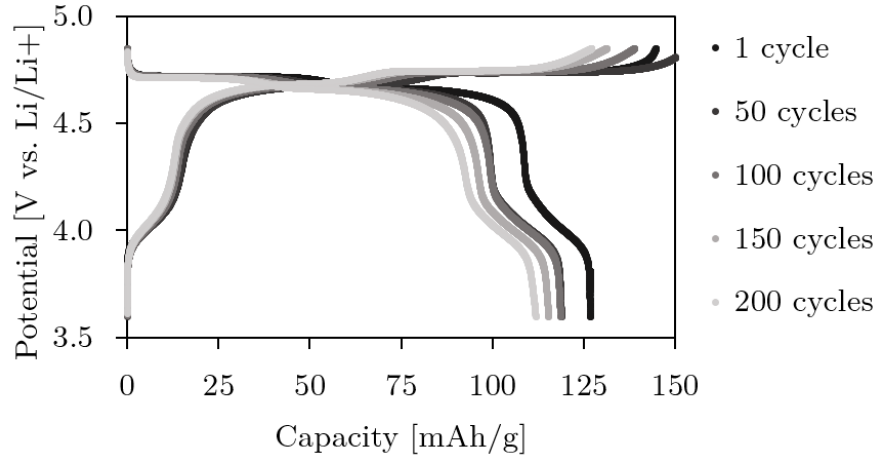

(a)

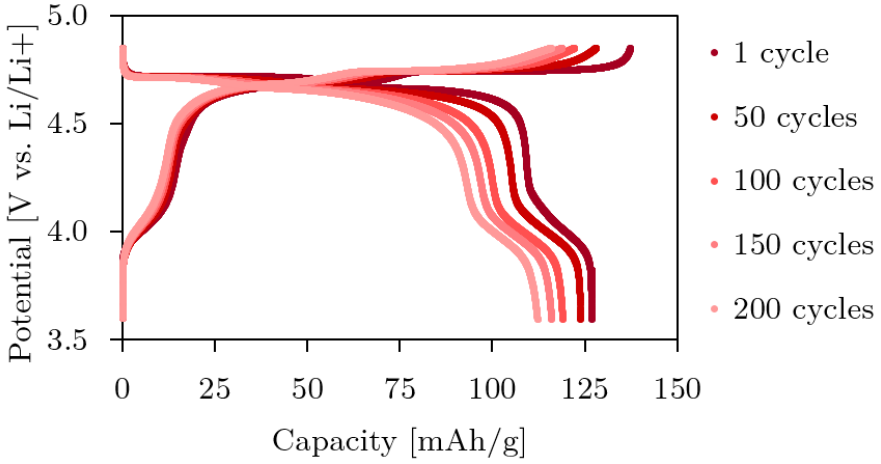

(b)

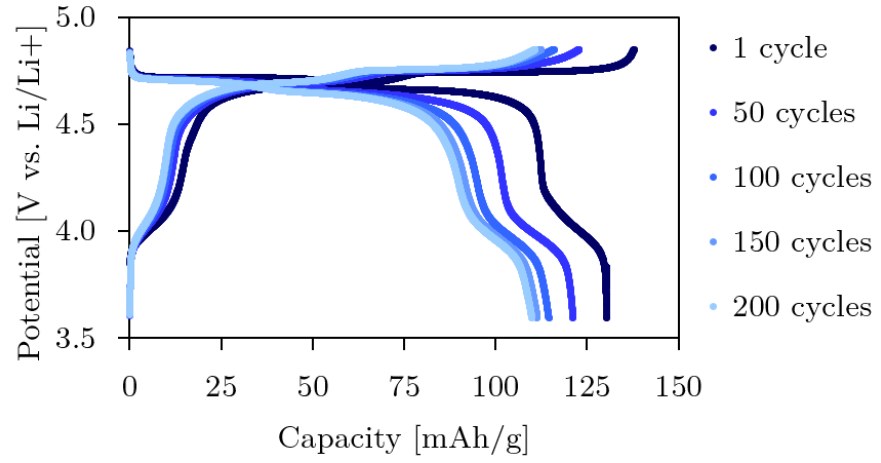

(c)

Figure 4.2.2: Potential profiles for (a) LP40, (b) 0.79 m RTIL and (c) 3 m RTIL after a certain number of cycles. The C-rate of the shown cycles is C/10, and the curves represent the successive cycle after 50 C/2 cycles, except for the curve of the first cycle.

which can be seen when comparing the discharge capacity at 2C of 104 mAh/g with the final discharge capacity at C/10 of 123 mAh/g. However, the cell does not degrade significantly, as the final C/10 cycles are not remarkably lower than the initial ones, although it should be pointed out that the degradation is even lower with LP40. 3 m RTIL shows a similar tendency to 0.79 m RTIL, but with a more significant difference between high and low C-rates. 3 m RTIL also shows greater signs of degradation since the final C/10 cycles are quite lower than the initial cycles. Figure 4.2.3b shows the coulombic efficiency throughout the rate test. The CE is similar for all electrolytes at low C-rates but differs at 1C and 2C. The difference is most significant in the transition between the C-rates, such as between 1C and 2C, and 2C and C/10. For instance, when increasing the C-rate from 1C to 2C, the CE drop is greatest for 3 m RTIL and lowest for LP40. Here, a drop in CE would indicate that more lithium ions are inserted than extracted, and the opposite effect can be observed when reducing the C-rate again to C/10 as the CE exceeds 100% considerably.

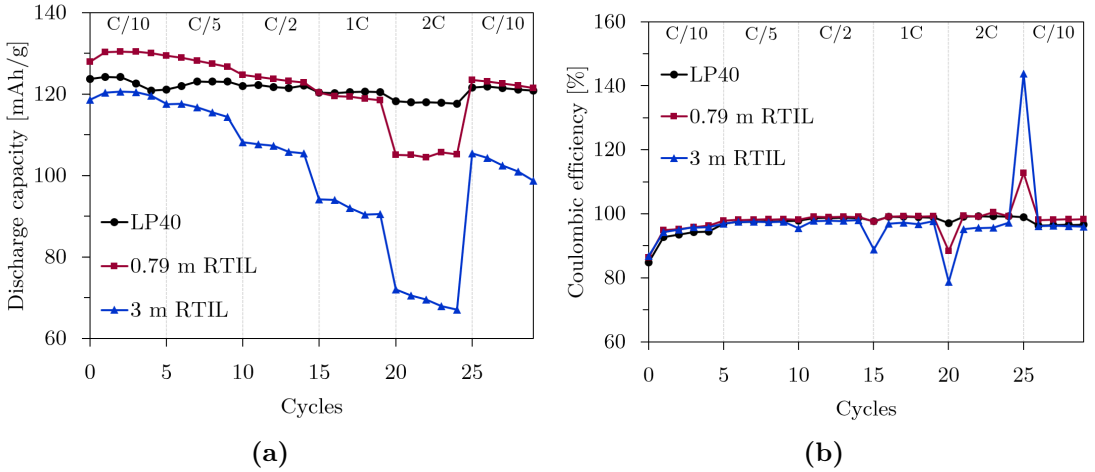

Figure 4.2.3: Rate test of LP40, 0.79 m RTIL and 3 m RTIL with five cycles of each C-rate, where (a) shows the discharge capacity and (b) shows the coulombic efficiency.

4.2.3 Ohmic Resistance from PEIS

Potentiostatic electrochemical impedance spectroscopy (PEIS) was used to determine the approximate ohmic resistance of the electrolytes right after the rate test was performed, and Nyquist plots are shown in Figure 4.2.4. The measurements indicate the differences in the ohmic resistance between the electrolytes. The ohmic resistance is given by the intercept with the real axis (x-axis). LP40 shows the lowest resistance, followed by 0.79 m RTIL. Significantly higher resistance is

observed for 3 m RTIL.

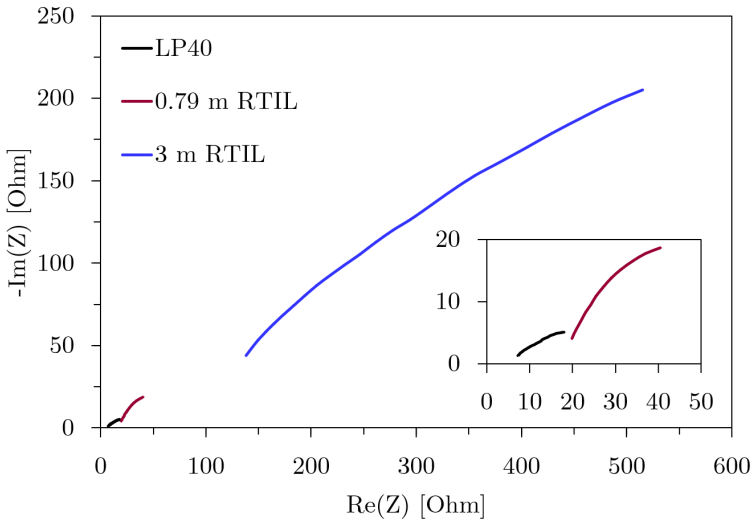

Figure 4.2.4: Nyquist plots from PEIS indicating the difference in ohmic resistance between the electrolytes.

4.2.4 Potential Profiles of LNMO without Carbon

The fabricated electrode material, which consisted of LNMO without carbon, was cycled with the electrolytes LP40 and 0.79 m RTIL at a slow C-rate of C/20. The potential profiles are presented in Figure 4.2.5, which show that the cells with both electrolytes behaved similarly, failed to produce any capacity and stopped after nearly 20 minutes.

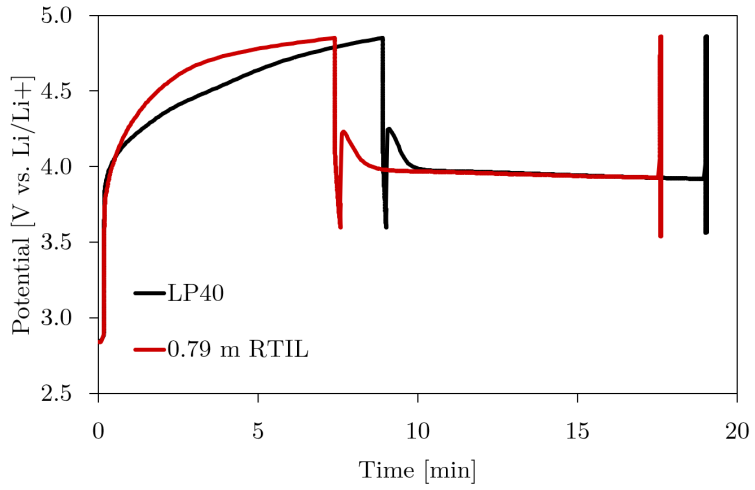

Figure 4.2.5: Potential profiles of LNMO without carbon with LP40 and 0.79 m RTIL show that the cells with both electrolytes stopped after a short time. The cells were cycled slowly with a C-rate of C/20.

4.3 Post-Mortem Characterisation

After cycling of the cells, the LNMO electrodes were extracted and characterised post-mortem with SEM, EDS and Raman spectroscopy as described in Section 3.5. These results will be presented for all electrolytes in addition to the results of LNMO without carbon.

Figure 4.3.1 shows SEM micrographs of electrodes cycled in the different electrolytes at the same magnification after 200 cycles compared to pristine LNMO. LP40 in Figure 4.3.1b indicates that darker spots/surface film have arose on the surface on some of the LNMO particles, and the network of carbon/binder between the particles has become more dominating and is also surrounding the particles to a greater extent. Figure 4.3.1c with 0.79 m RTIL indicates that unlike LP40, there are no film formation on the particle surface. The characteristic triangles are also more preserved, but the carbon/binder network is present in a similar degree. 3 m RTIL in Figure 4.3.1d shows that the surfaces of the upper particles are intact, but the edges of the particles have a different appearance, and the carbon/binder network is completely covering the lower particles.

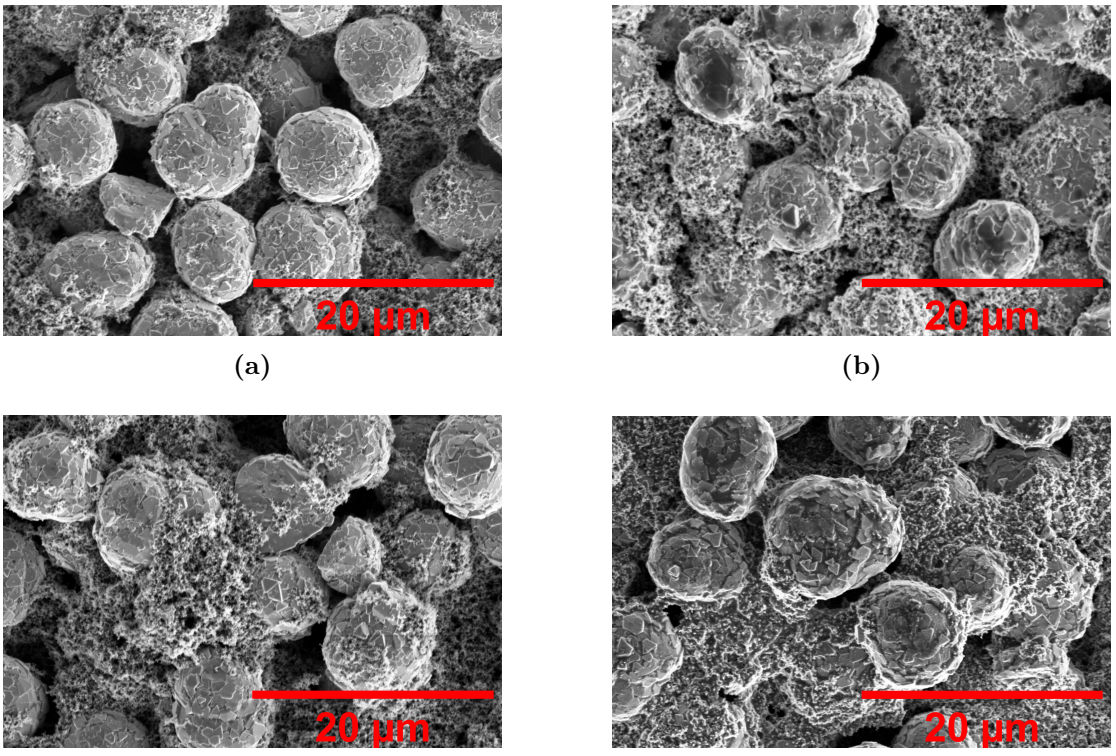

(a) **(b)**

(c) **(d)**

Figure 4.3.1: SEM images of (a) pristine LNMO and after 200 cycles: (b) LP40, (c) 0.79 m RTIL and (d) 3 m RTIL.

Figure 4.3.2 shows the Raman spectra of the different electrolytes compared to pristine LNMO, with the chemical origin of the characteristic peaks. Both LP40 and 0.79 m RTIL display the same shape as pristine LNMO, preserving the ratio between the different peaks, except that the carbon bands are less present. 3 m RTIL shows a clearer change in shape, where especially the nickel bands are less intense. Additionally, 3 m RTIL stands out from the others with a peak at higher a Raman shift, which probably is attributed to phosphate from the decomposition of the electrolyte, distinguished by a peak around 947 cm^{-1}.

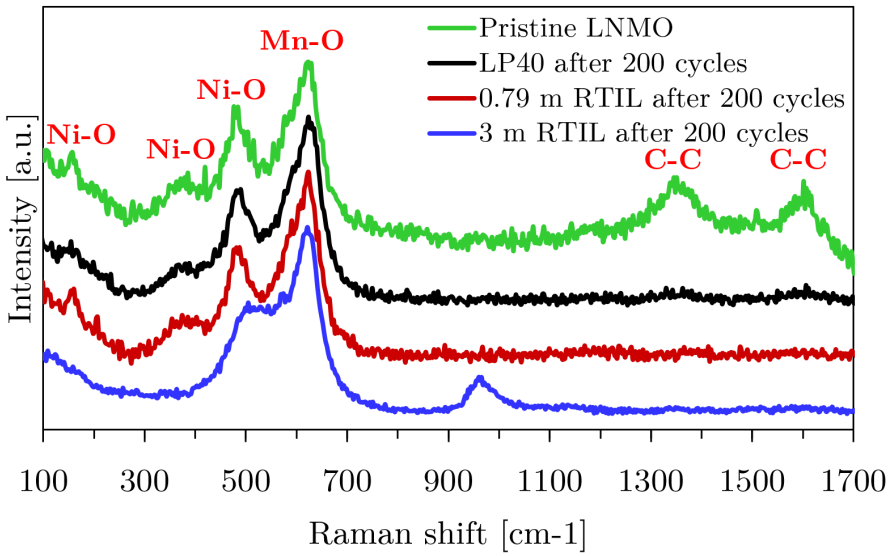

Figure 4.3.2: Raman spectrum after 200 cycles of LNMO with LP40, 0.79 m RTIL and 3 m RTIL in comparison to pristine LNMO, with chemical bands corresponding to the peaks [21] [52].

The intensity ratios were calculated based on the Ni and Mn bands from the Raman spectrum in Figure 4.3.2. The ratios after 200 cycles are presented in Table 4.3.1, in comparison to pristine LNMO. It demonstrates that there is less Ni signal after cycling, especially for LP40 and 3 m RTIL. 0.79 m RTIL exhibit a ratio closer to the pristine's ratio.

Table 4.3.1: Intensity ratio between the highest Ni-O band and the Mn-O band.

Sample	Ratio $\frac{I_{Ni}}{I_{Mn}}$
Pristine	0.86
LP40	0.64
0.79 m RTIL	0.73
3 m RTIL	0.63

4.3.1 LP40

Figure 4.3.3 demonstrates how LP40 changes during cycling, from pristine LNMO in Figure 4.3.3a to after 100 cycles in Figure 4.3.3b and after 200 cycles in Figure 4.3.3c. The images show that already after 100 cycles, dark surface spots appear on some of the particle, which may indicate a film forming. This is more notable after 200 cycles, where the original triangles are more covered. Also, the carbon/binder network is more dominant.

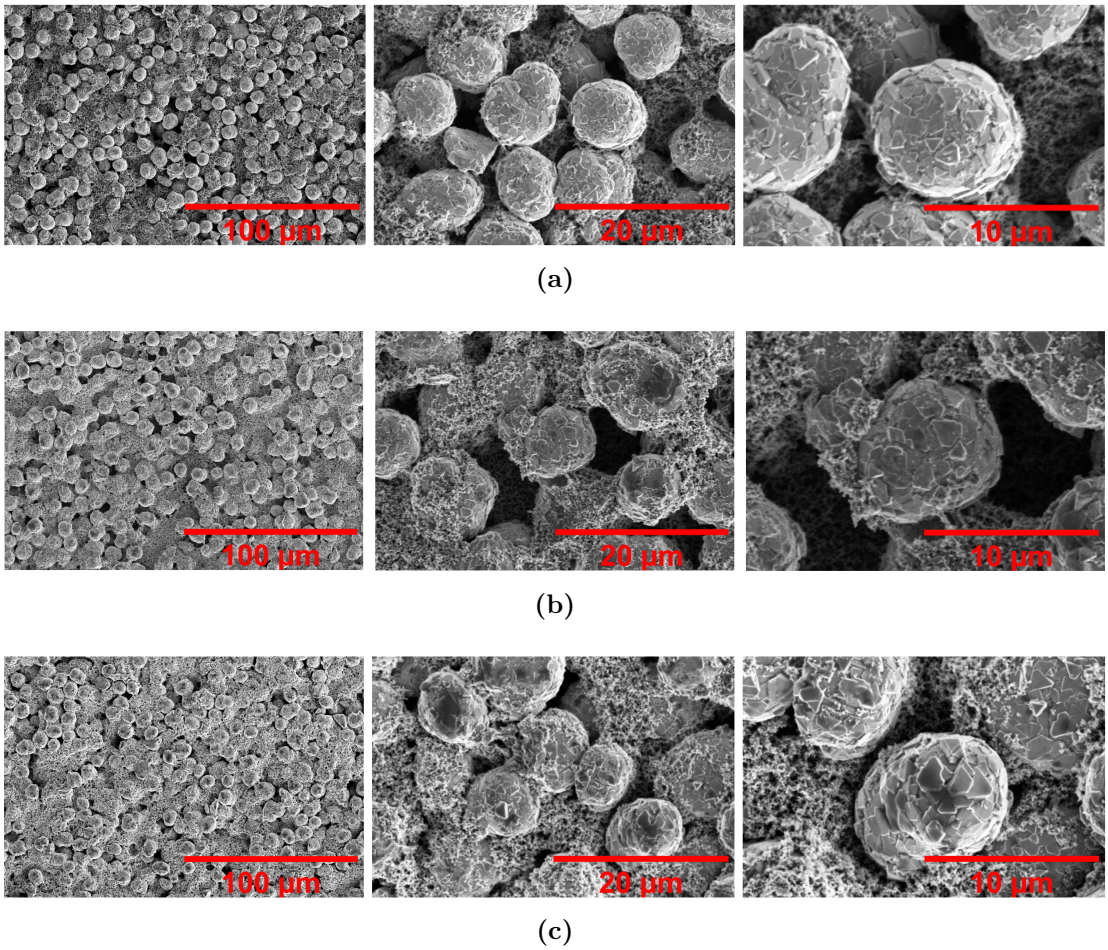

Figure 4.3.3: SEM images of (a) pristine LNMO and LP40 after (b) 100 cycles and (c) 200 cycles (unlayered area).

Figure 4.3.4 shows how the Raman spectra change from pristine LNMO compared to after 100 and 200 cycles. It can be observed that the characteristic peaks of LNMO are also present in all spectra, with similar ratio of intensity between the different bands. The only difference is that the carbon bands are less visible.

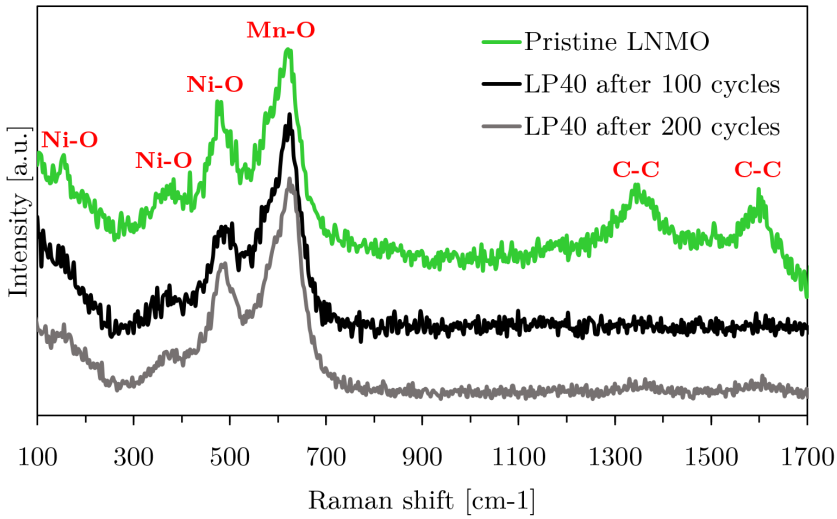

Figure 4.3.4: Raman spectrum of LNMO with LP40 after 100 and 200 cycles in comparison to pristine LNMO, with chemical bands corresponding to the peaks [21] [52].

The intensity ratios of LP40 after 100 and 200 cycles in comparison to pristine LNMO are presented in Table 4.3.2. It shows that the Ni signal decreases in relation to Mn, particularly until 100 cycles.

Table 4.3.2: Intensity ratio between the highest Ni-O band and the Mn-O band.

Sample	Ratio $\frac{I_{Ni}}{I_{Mn}}$
Pristine	0.86
LP40 after 100 cycles	0.62
LP40 after 200 cycles	0.64

The EDS analysis of LP40 after 100 cycles is presented in Figure 4.3.5, where the two images is of the exact same area, but with different accelerating voltages. At low accelerating voltage (3 kV) in the left image, the dark spots are visible, but when increasing the voltage to 15 kV for the EDS analysis in the right image, the spots can hardly be observed. The reason is that the EDS analysis captures signal from a much bigger volume than only the surface, indicating that the darker spots are surface products. The analysis indicates how the elements are distributed, where O, Mn and Ni clearly fit the LNMO particles and C is located on the edges. F and P from the binder and the electrolyte are less intense, but also distributed on the particle surface.

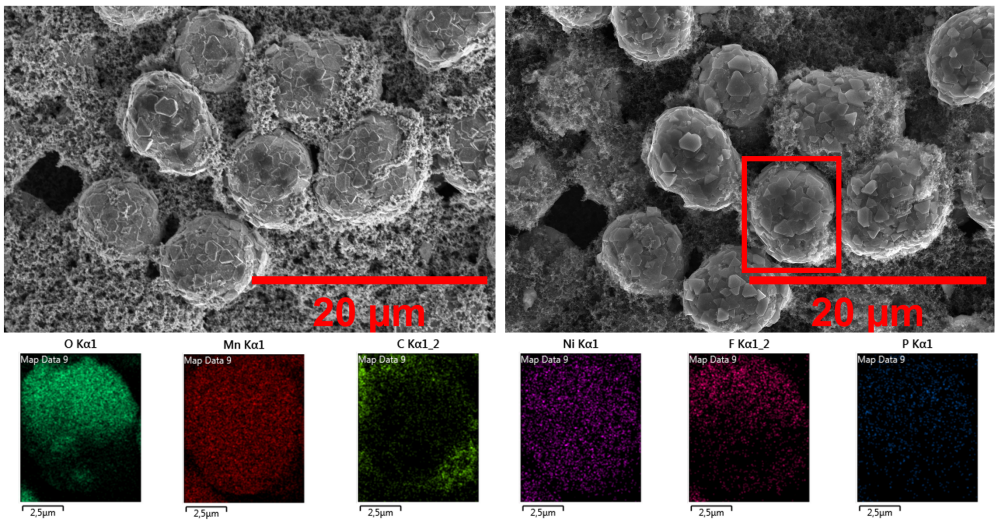

Figure 4.3.5: EDS analysis of LNMO with LP40 after 100 cycles, where the left image is taken with an accelerating voltage of 3 kV and the image on the right representing the analysis is taken of the exact same area with 15 kV.

For the LNMO electrode after 200 cycles with LP40, two different types of areas were observed in the same sample, as indicated in Figure 4.3.6. The left area constitutes to the largest part of the LNMO electrode and shows a similar appearance as after 100 cycles. For the area on the right, the particles are surrounded by a thick layer.

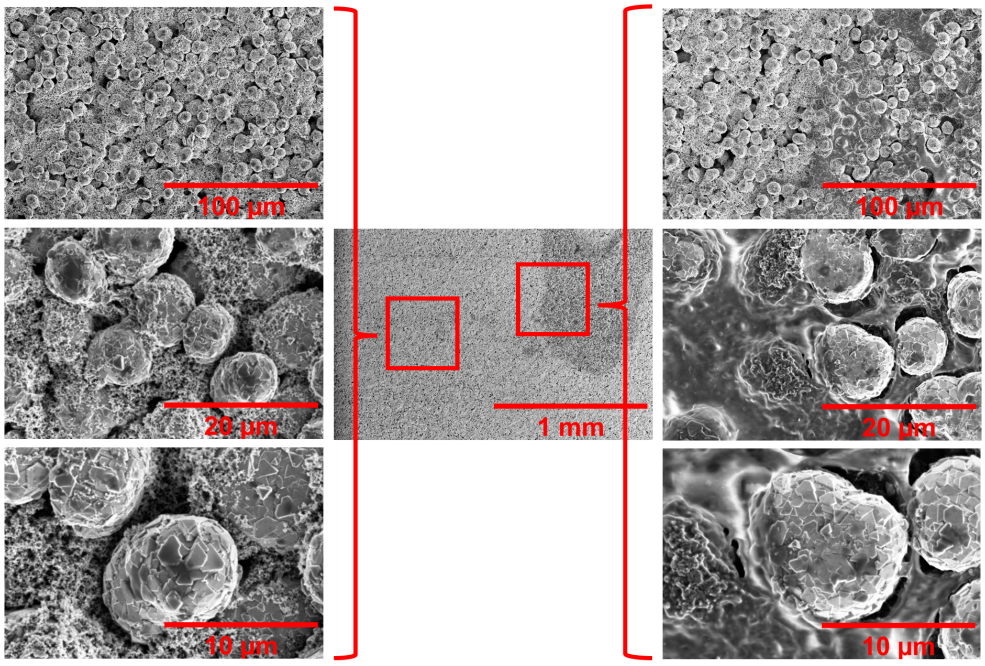

Figure 4.3.6: SEM images of LNMO with LP40 after 200 cycles showing two different areas of the electrode, where a thick layer is dominating and surrounding the particles in the area on the right side.

The two different areas were analysed with EDS and compared in Figure 4.3.7. The left area presented in Figure 4.3.7a shows a similar element distribution as after 100 cycles. The right area in Figure 4.3.7b shows LNMO particles that are surrounded by a layer of carbon black, binder, and decomposition products. The analysis suggests that the layer consists of carbon, phosphorous and fluorine, where the latter is the only element present in both the layer and the particle.

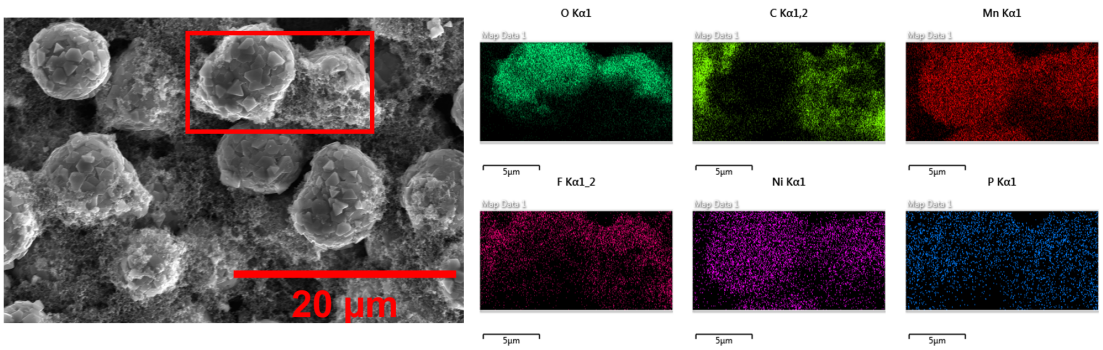

(a)

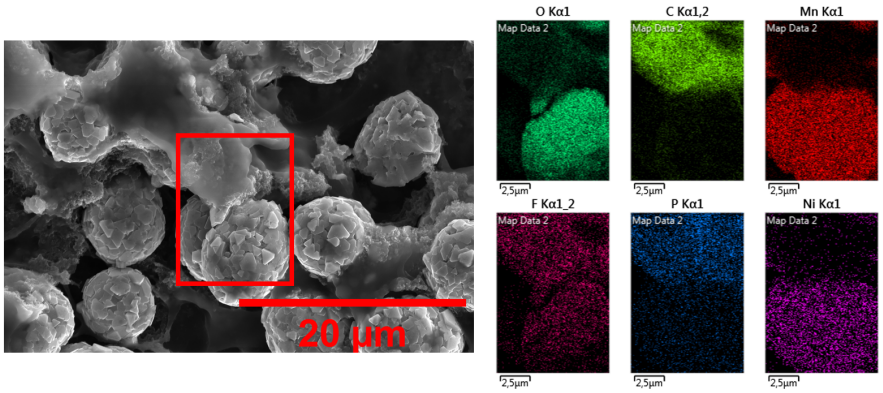

(b)

Figure 4.3.7: EDS analysis of LNMO with LP40 after 200 cycles, where (a) represents the area without a layer and (b) represents the area where a layer is dominating.

The Raman spectra in Figure 4.3.8 confirm a different composition than the non-layered region. Figure 4.3.8a shows less intense Ni peaks than in the non-layered area. For the layer itself, presented in Figure 4.3.8b, this is completely dominated by carbon bands.

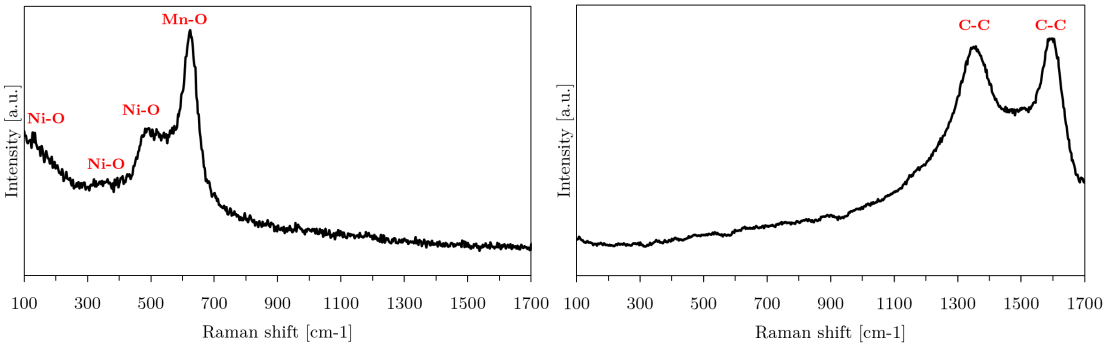

(a) **(b)**

Figure 4.3.8: Raman spectrum of layered area in LNMO with LP40 after 200 cycles where (a) is the LNMO particle and (b) is the layer surrounding the particles, with chemical bands corresponding to the peaks [21] [52].

4.3.2 0.79 m RTIL

Figure 4.3.9 shows the LNMO electrode with 0.79 m RTIL after 50 and 200 cycles, compared to pristine LNMO. When it comes to the surface of the particles, there is no major change from 50 to 200 cycles. The only change that may be observed is that the carbon/binder network is becoming more visible and more present on the top of some of the particles.

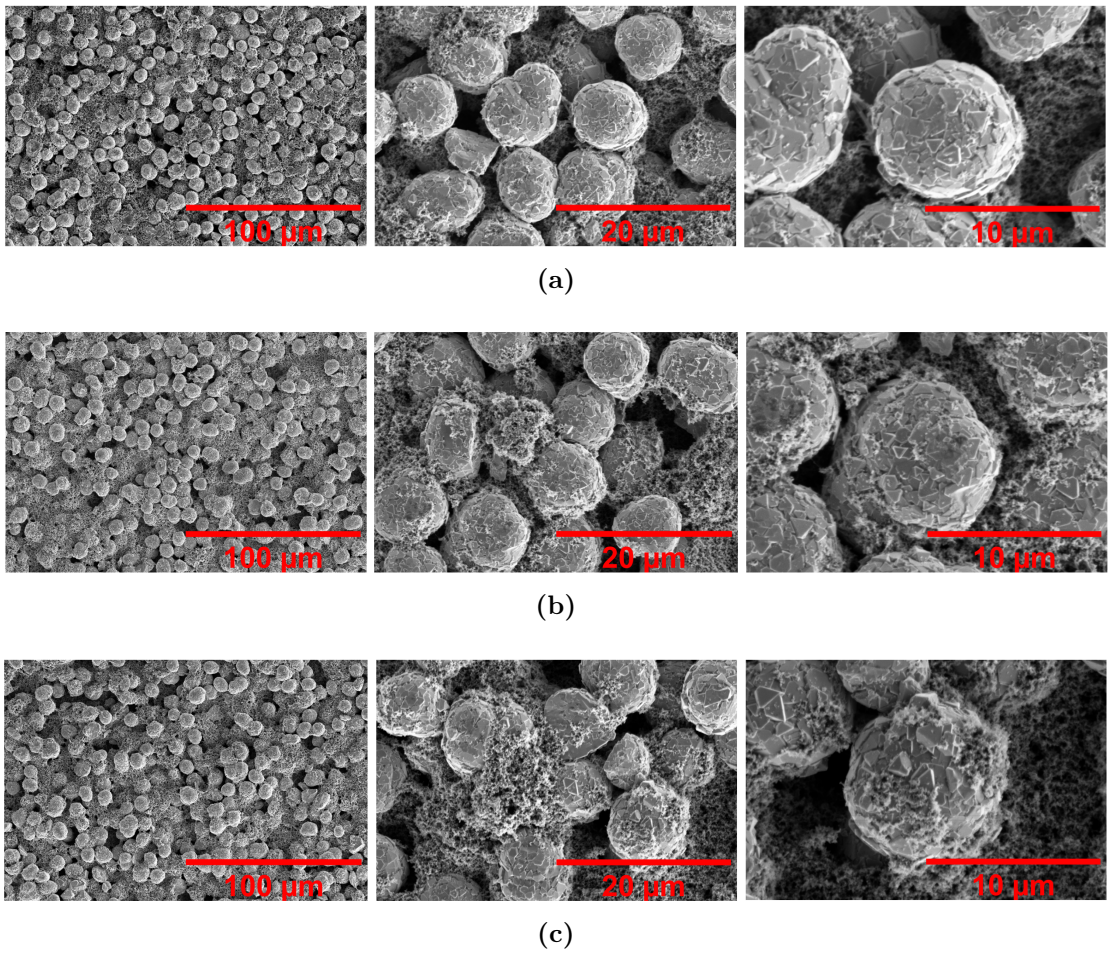

Figure 4.3.9: SEM images of (a) pristine LNMO and 0.79 m RTIL after (b) 50 cycles and (c) 200 cycles.

The Raman spectra in Figure 4.3.10 for 0.79 m RTIL after 50 and 200 cycles, indicate that the original shape of the pristine material is preserved, and all Ni and Mn bands are intense and present. The only difference from the pristine LNMO is the lack of carbon bands.

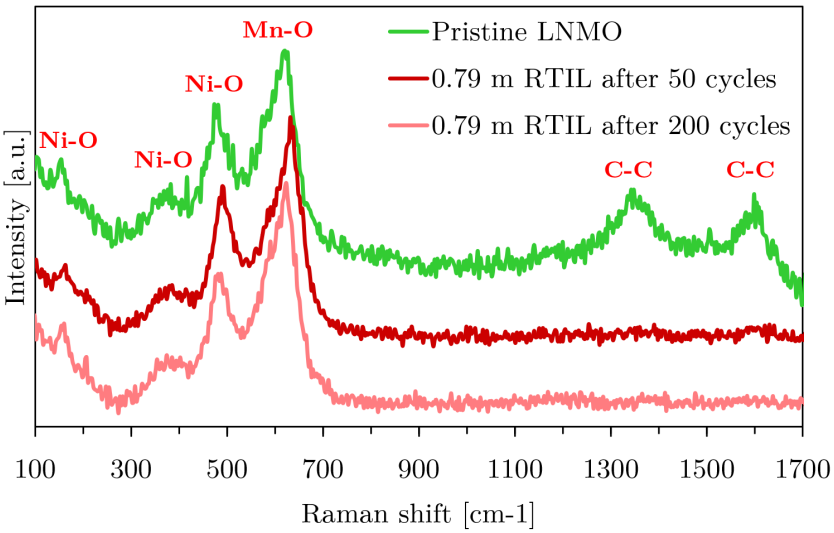

Figure 4.3.10: Raman spectrum of LNMO with 0.79 m RTIL after 50 and 200 cycles compared to pristine LNMO, with chemical bands corresponding to the peaks [21] [52].

The intensity ratios of 0.79 m RTIL after 50 and 200 cycles compared to pristine LNMO are presented in Table 4.3.3. The ratios indicate that there is a reduction in the ratio from the pristine material to after 50 cycles, with a small further decrease until 200 cycles.

Table 4.3.3: Intensity ratio between the highest Ni-O band and the Mn-O band.

Sample	Ratio $\frac{I_{Ni}}{I_{Mn}}$
Pristine	0.86
0.79 m RTIL after 50 cycles	0.78
0.79 m RTIL after 200 cycles	0.73

Figure 4.3.11 shows the EDS analyses of 3 m RTIL after 50 and 200 cycles. Figure 4.3.11a indicates that the elements F, S, P and N, which originate from the electrolyte, are similarly distributed on the sample, both on the particles and the area where carbon is located. The analysis after 200 cycles in Figure 4.3.11b shows a similar distribution as after 50 cycles, with strong signals of the electrode elements and weaker signals of the electrolyte elements.

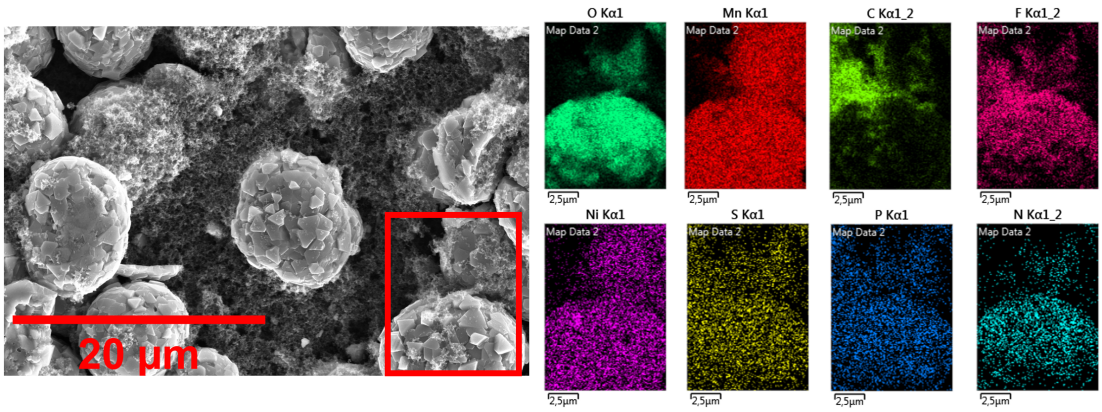

(a)

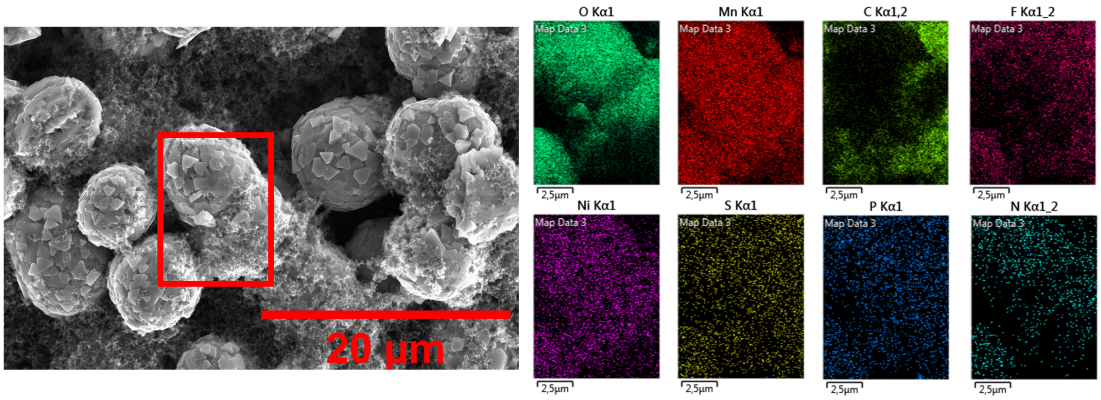

(b)

Figure 4.3.11: EDS analysis of 0.79 m RTIL after of (a) 50 cycles and (b) 200 cycles.

4.3.3 3 m RTIL

Figure 4.3.12 shows the LNMO electrode with 3 m RTIL after 50 and 200 cycles, in comparison to pristine LNMO. There is a significant difference between the pristine material in Figure 4.3.12a and the 3 m RTIL in Figure 4.3.12b and 4.3.12c, in terms of an extensive network surrounding the particles. The surface of the particles seems to be preserved, especially after 50 cycles, but show some damage after 200 cycles.

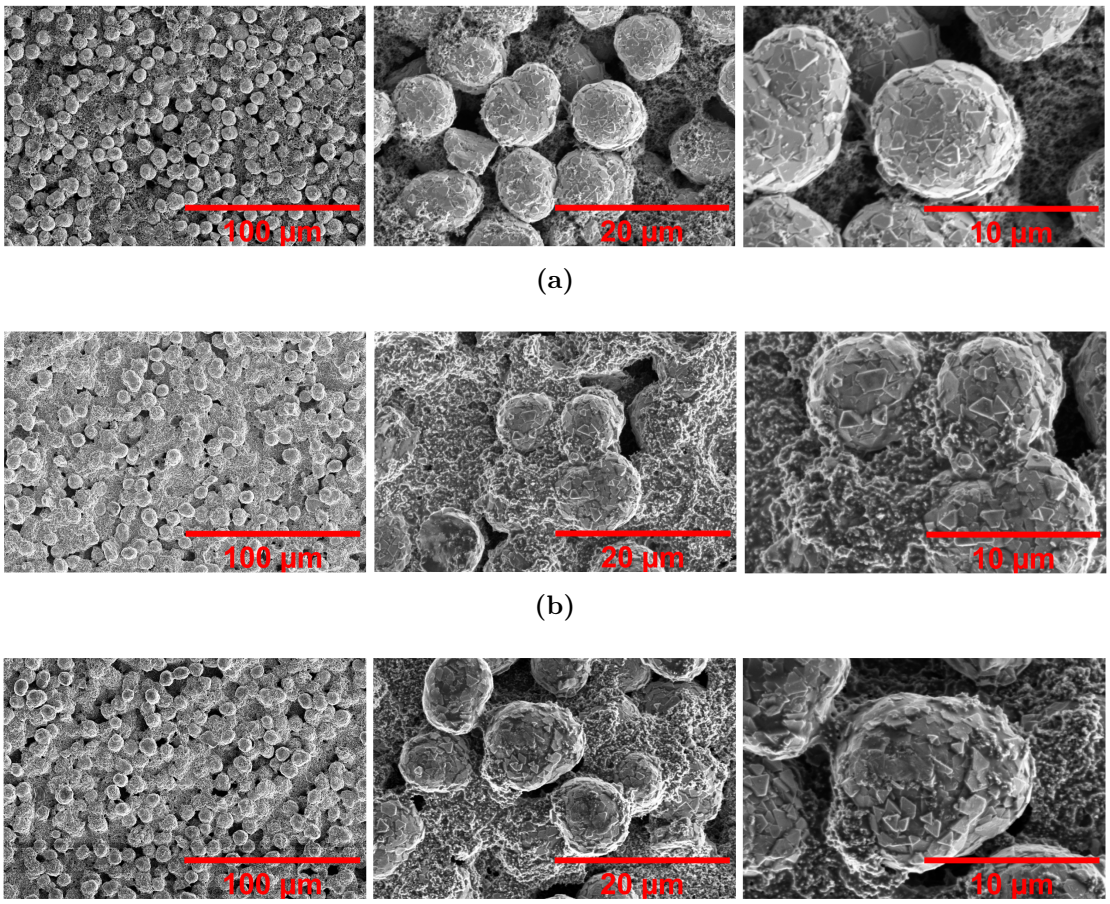

Figure 4.3.12: SEM images of (a) pristine LNMO and 3 m RTIL after (b) 50 cycles and (c) 200 cycles.

Figure 4.3.13 compares the Raman spectra of pristine LNMO with 3 m RTIL after 50 and 200 cycles. Even though the scale in intensity is different, the relative peak heights can be compared. While the Mn band is preserved from the pristine material, the most substantial difference is related to the Ni bands. Already after 50 cycles, the distinct and highest Ni peak has lost its original shape and appears more as a shoulder to the Mn peak. The other Ni bands of lower Raman shift are almost not existing. However, a new peak has arose in the middle region of the

spectra at around 950 cm^{-1}, which is not present for the pristine sample. This is believed to have its origin in phosphate which has formed due to electrolyte decomposition, distinguished by a peak around 947 cm^{-1}.

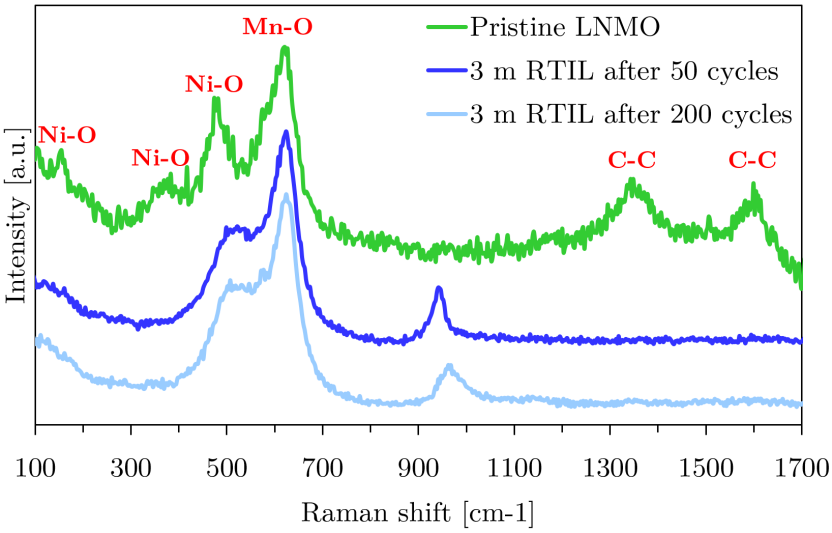

Figure 4.3.13: Raman spectrum of LNMO with 3 m RTIL after 50 and 200 cycles in comparison to pristine LNMO, with chemical bands corresponding to the peaks [21] [52].

Table 4.3.4 contains the calculated intensity ratios of 3 m RTIL after 50 and 200 cycles in comparison to the pristine material. There is a significant drop to 0.67 already after 50 cycles, with a further decrease until 200 cycles.

Table 4.3.4: Intensity ratio between the highest Ni-O band and the Mn-O band.

Sample	Ratio $\frac{I_{Ni}}{I_{Mn}}$
Pristine	0.86
3 m RTIL after 50 cycles	0.67
3 m RTIL after 200 cycles	0.63

The EDS analyses of 3 m RTIL after 50 and 200 cycles is presented in Figure 4.3.14. In the analysis after 50 cycles in Figure 4.3.14a, there is a variation between the electrolyte elements which take place at the LNMO particle, and the others that avoid it. For instance, S and P are distributed equally in the area besides the particle, while F and N are located also on top of the particle. For the sample after 200 cycles in Figure 4.3.14b, there is a layer on top of and between the two scanned particles. The analysis indicates that the elements S, F and P from the electrolyte, in addition to C, are dominating in the layer.

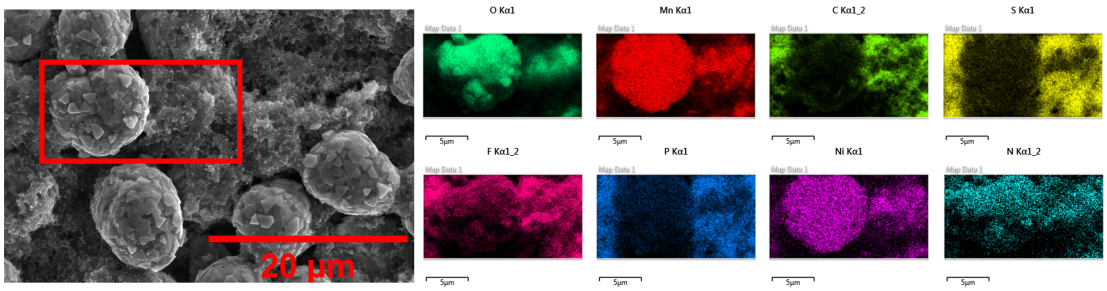

(a)

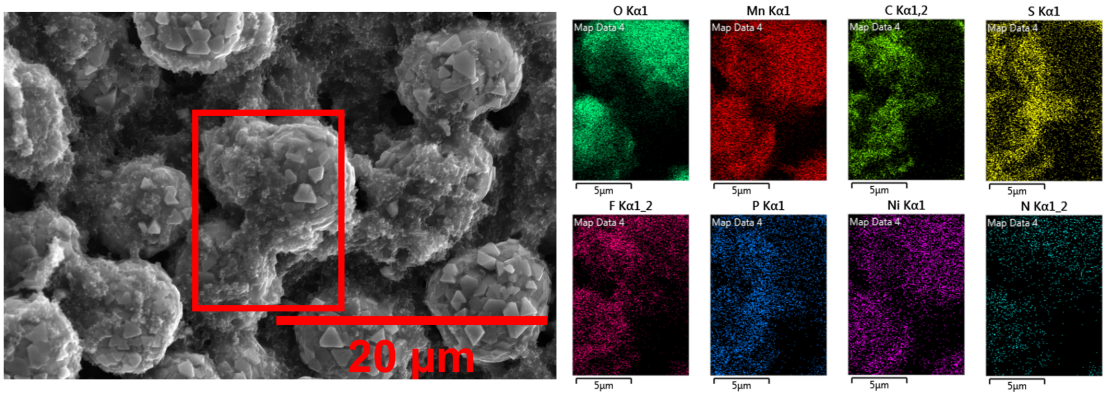

(b)

Figure 4.3.14: EDS analysis of 3 m RTIL after of (a) 50 cycles and (b) 200 cycles.

4.3.4 LNMO without Carbon

Figure 4.3.15 shows images of pristine LNMO without carbon in comparison to with LP40 and 0.79 m RTIL. The electrode material failed to cycle, but difference between the two electrolytes is displayed. With LP40 in Figure 4.3.15b a darker layer on some of the particles can be observed, while with 0.79 m RTIL in Figure 4.3.15c the surface is intact, but the appearance differs in the boundaries between the LNMO particles. All images also indicate voids between the LNMO particles.

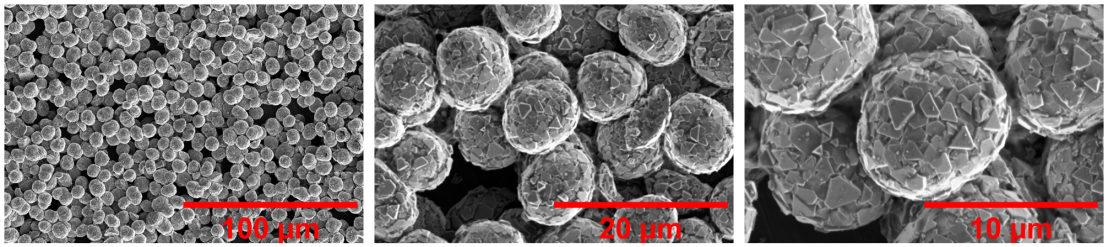

(a)

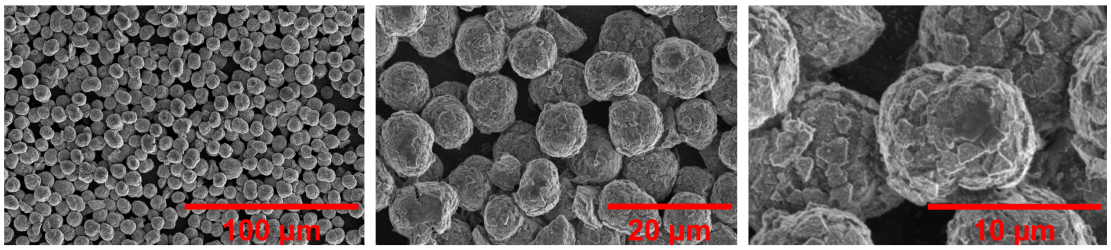

(b)

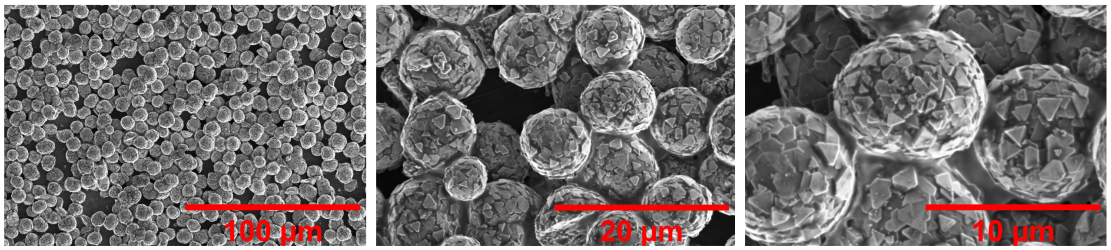

(c)

Figure 4.3.15: SEM images of (a) pristine LNMO without carbon and LNMO without carbon with (b) LP40 and (c) 0.79 m RTIL. Note that the image in the middle of (b) is not in the same exact scale as the others.

In the Raman spectra in Figure 4.3.16, all the spectra have similar shapes.

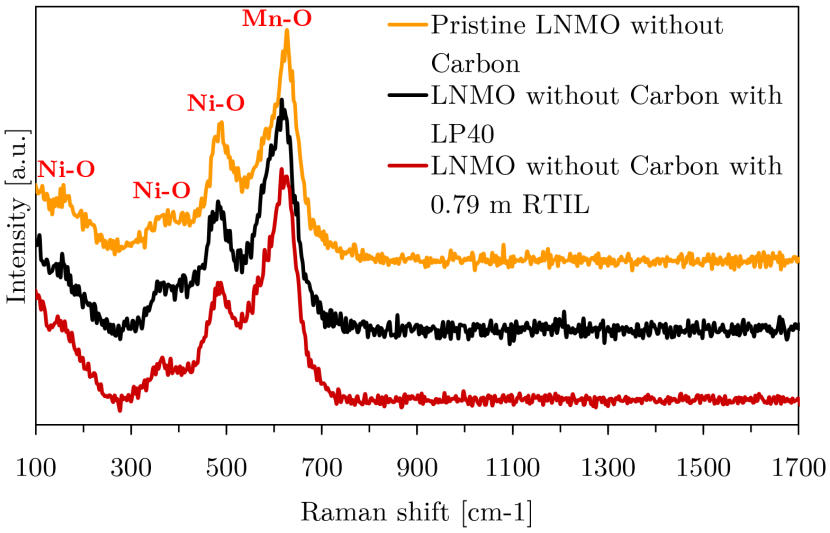

Figure 4.3.16: Raman spectrum of LNMO without carbon with LP40 and 0.79 m RTIL in comparison to pristine LNMO, with chemical bands corresponding to the peaks [21].

The intensity ratios in Table 4.3.5 shows that with LP40, the ratio is similar to the pristine sample, but with the RTIL there is a decrease.

Table 4.3.5: Intensity ratio between the highest Ni-O band and the Mn-O band.

Sample	Ratio $\frac{I_{Ni}}{I_{Mn}}$
Pristine LNMO without Carbon	0.76
LP40	0.69
0.79 m RTIL	0.55

The EDS analyses of LNMO without carbon, with both LP40 and 0.79 m RTIL, are presented in Figure 4.3.17. The analysis of LP40 in Figure 4.3.17a shows an even distribution in the electrode elements, with a low signal of P from the electrolyte. For the RTIL in Figure 4.3.17b, the elements are also evenly distributed, with a weak signal from the electrolyte elements as S, P and N.

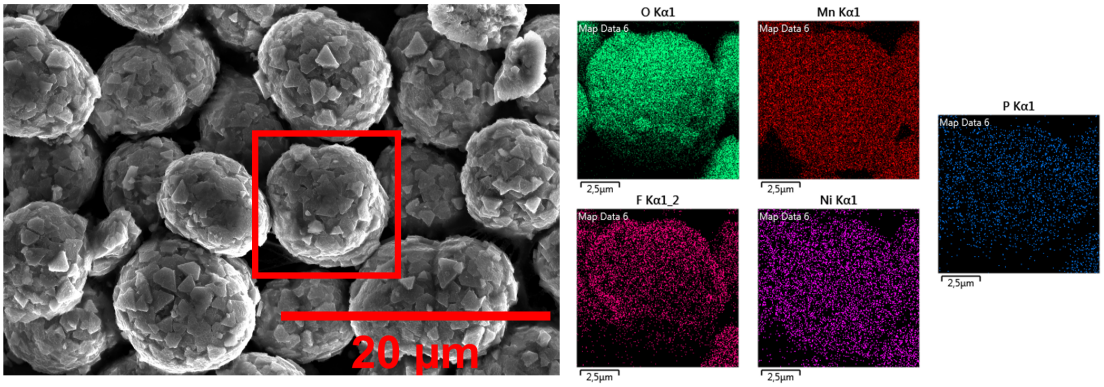

(a)

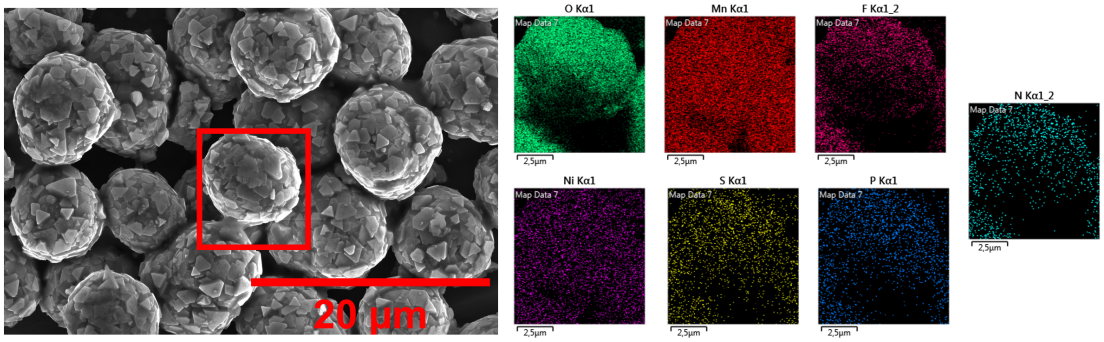

(b)

Figure 4.3.17: EDS analysis of LNMO without carbon with (a) LP40 and (b) 0.79 m RTIL.

Chapter 5

Discussion

5.1 Fabricated LNMO and Its Performance with Conventional Electrolyte

5.1.1 Characterisation of LNMO Electrode Material

The fabricated pristine LNMO electrode material was characterised with SEM, EDS, and Raman spectroscopy as a reference for the later study of degradation of the electrode surface in combination with various electrolytes. The SEM images presented in Figure 4.1.2 shows an even distribution of LNMO particles at the electrode surface, surrounded by a network of carbon and binder solution. The majority of the particles have spherical shapes, with the exception of a few that are deformed and broken into smaller parts, possibly due to the slurry mixing and/or the calendering process [53] [54]. When focusing on the LNMO particles, the surface contains characteristic triangles, also shown by Østli et al. [55]. Also, smaller, and brighter particles can be observed on the surface of the spheres, which has its origin in the conductive additive, carbon black.

The EDS analysis in Figure 4.1.3 shows that the elements from the active material LNMO causes the strongest signal, especially oxygen and manganese. Nickel is also an element in the active material but appears unexpectedly weak in this analysis. Even though Ni should not cause as strong signal as O and Mn due to the stoichiometric ratio of $LiNi_{0.5}Mn_{1.5}O_4$, previous work done by the author has showed an intensity closer to Mn [56]. The analysis also shows that carbon, with its origin in the conductive additive, is mainly located at the edges and around the LNMO particles. Some fluorine signal from the binder solution with PVDF is captured by the EDS, but the signal is scattered in the EDS map. Since F is a light element, the analysis can only be used to indicate that it is present and not

the exact position nor amount.

The Raman spectrum of the pristine LNMO material is presented in Figure 4.1.1. As described in Section 2.3.1, the spectrum confirms that the fabricated LNMO material is of the disordered structure with space group $Fd\bar{3}m$. There are six distinct peaks in the spectrum, where the the peaks between 100 and 700 cm^{-1} have their origin in LNMO. The three peaks of lowest Raman shift, at approximately 160, 380 and 480 cm^{-1}, are related to Ni-O bands. The two peaks with the lowest Raman shift are significantly less intense than the peak at 480 cm^{-1}, which is a characteristic for disordered LNMO. There is only one peak related to manganese bands in the Raman spectrum of disordered LNMO, which is located around 620 cm^{-1} and is the most intense peak of the spectrum [21]. In addition to the peaks belonging to LNMO, there are also two peaks present at the high Raman shift region, at around 1350 and 1600 cm^{-1}. These peaks have their origin in the D- and G-band of carbon, respectively [23].

5.1.2 Performance with LP40

The main purpose of cycling the LNMO material with LP40 was for the later comparison with the RTILs. In terms of galvanostatic cycling, reference cells with LP40 were both cycled over a long period (200 C/2 cycles) and at different C-rates (from C/10 to 2C), which give accurate information about the fabricated LNMO material in combination with a conventional electrolyte system. The discharge capacity of LP40 is evaluated in Figure 4.2.1a. LP40 shows an initial discharge capacity of 132 mAh/g, which is in accordance with other studies, where Yu et al. have reviewed published experimental work involving LNMO [57]. From the intitial capacity, the overall capacity fade is even, but LP40 displays abnormal behaviour when decreasing the C-rate to from C/2 to C/10, where it drops significantly, especially during the first half of the cycling program. This is the opposite to the typical behaviour but was observed in all the cells with LP40. Further investigation of this phenomena did not result in any reasonable outcome. LP40 demonstrated a capacity retention of 86.8% after 200 cycles, which is lower than previously produced results by the author [56], but is still superior to other works from open literature publications. For instance, Rong et al. have reported a capacity retention of 76.6% after 200 cycles with similar electrolyte system and C-rate [58]. The coulombic efficiency of LP40 is overall stable around 95-96%, which is worse than the author's previous results (>99%) and also the majority of published CE data [57]. A relatively low coulombic efficiency indicates that quite considerable electrochemical side reactions occur in the cell [59]. The exception

in the steady CE is when the C-rate is reduced, where a drop in CE is observed which is less severe throughout the cycling program, as with the capacity. A drop in CE indicates that more lithium is inserted in the active material than what is extracted. As opposed to the discharge capacity drops, a decline in CE when decreasing the C-rate is typical behaviour and observed in related experimental studies [60].

Figure 4.2.2a indicates how the potential profiles change during the cycling period. The characteristic potential plateaus of Ni and Mn redox couples, indicated in Figure 2.3.3b, are all present in the curves, also after 200 cycles. The gap between the charge curve and discharge curve increases with number of cycles and is a common consequence of that the polarisation increases over time, meaning that the resistance against lithiation/delithiation of the active material increases [61].

The performance of LP40 at different C-rates is presented in the rate test results in Figure 3.4.2. Both the discharge capacity (Figure 4.2.3a) and CE (Figure 4.2.3b) are relatively stable during all C-rates, but there is a minimal and expected reduction in discharge capacity at the highest C-rates. The reduction is however significantly less than in the rate test of LNMO performed by Østli et al. [60], and also other comparable rate test [57]. It is worth mentioning that the rate performance is very dependent on the thickness/loading [g/cm^2] of the electrode, where the performance is reduced when the loading is increased [62]. For instance, Østli et al. fabricated LNMO electrodes for the rate test with a loading twice as high as in this thesis, which may describe the significant difference. After the rate test, the ohmic resistance in LP40 was obtained with PEIS. This showed a resistance around 10 Ω, which is in the same order of magnitude as other reported studies of similar half cells [63].

The SEM images of LP40 after 100 and 200 cycles in Figure 4.3.3 indicate that darker spots occur at the surface of several of the LNMO particles at the electrode. The spots seem to be even more visible after 200 cycles, which may indicate that a layer is forming during cycling. As this layer is covering the LNMO surface, it might contribute to degrading the electrode material. Wang et al. have also discovered a thick surface film on the LNMO particles after cycling with $LiPF_6$ in a carbonate-based electrolyte. They point out that the film is formed during side reaction process and results in capacity loss and increase in resistance [64]. The EDS analysis of LP40 after 100 cycles in Figure 4.3.5 has been compared with the ordinary SEM images with a lower accelerating voltage, which clearly indicates

where the spots are located. The selected particle for the analysis contains such spot but shows that the EDS analysis is not able to capture it. The reason is that the EDS technique, with a higher accelerating voltage, captures signal of a much bigger volume of the sample than only the surface [51]. The elements distribution is similar to the distribution of pristine LNMO, but with the feature of the electrolyte's elements, such as fluorine and and a weak signal of phosphorous. F and P is located on the particle, which does not exclude that the surface film may has its origin in these elements.

The Raman spectra presented in Figure 4.3.4 together with the calculated intensity ratios in Table 4.3.2 demonstrate a small decrease in especially the nickel bands already after 100 cycles, from a ratio of 0.86 to 0.62. It has previously been shown that this is a typical behaviour of LNMO with LP40 after cycling, namely that Ni decreases significantly in proportion to Mn [65]. Transition metal dissolution is a known degradation mechanism in LNMO, which involves both Mn and Ni [6]. The calculated intensity ratio indicates that Ni is most affected. Additionally, the carbon bands are less present after cycling, which could indicate that the conductive additive no longer is as present at the particle surface due to the formation of surface products.

After 200 cycles, there is a noteworthy change taking place on the electrode surface, illustrated in Figure 4.3.6. The majority of the electrode is showing a typical LNMO surface with LP40, but there is also a large part on the right side which appears darker, with the approximate measures of 1 mm x 0.5 mm. Magnified images of this area disclose that a thick, glue-like layer is surrounding the LNMO particles. The EDS analysis in Figure 4.3.7b of this area demonstrates that the layer consists of carbon, fluorine and phosphorus, where F and P have their origin in the electrolyte. The layer can be a result of electrolyte decomposition and seems to block the signal of the LNMO particles beneath. It is challenging to determine the reactions and mechanisms behind the layer that has formed, but Pieczonka's work can be utilised in an attempt to describe the likely decomposition of the electrolyte [6]. It has been discovered that the solvents EC and DEC decompose and form oxidation products on the LNMO surface at high potentials, according to Equation 2.9 and 2.10, respectively. Additionally, the formation of HF will dissolve the active material as described in Equation 2.12, leading to fluorine-based products formed on the electrode surface, such as LiF, MnF_2, NiF_2. These mechanisms can therefore explain the presence of a thick layer on the electrode surface consisting of C, F and P, as discovered in the EDS analysis.

The Raman spectrum of the LNMO particles in the layered region, given in Figure 4.3.8a, displays a significant reduction in the signal of the Ni peaks. This also reveals that the particles, which appear uncovered by the thick layer, are heavily influenced by the surrounding layer. The spectrum of the layer itself in Figure 4.3.8b gives signal only for carbon, but as the peaks of carbon generally are more intense than the peaks of other elements, it does not exclude that F and P are present, as the EDS analysis indicates.

5.2 Performance of the RTILs and the Effect of Salt Concentration

5.2.1 Electrochemical Performance

Both 0.79 m (low-concentrated) and 3 m (high-concentrated) RTIL were tested with the objective to study their performance compared to the reference LP40, in addition to determine whether high or low concentration resulted in the best performance. Their electrochemical performance were thoroughly examined both over 200 cycles and at high C-rates in a rate test. The discharge capacity of the electrolytes is presented in Figure 4.2.1a. 3 m RTIL faces a fast capacity drop until approximately 100 cycles, when it then stabilises, while 0.79 m RTIL follows a fade similar to LP40. 0.79 m RTIL also flattens out to some degree at the end of the cycling program, but not as much as 3 m RTIL. This may indicate that 3 m RTIL encounters a saturation point in the capacity decay but is regardless outperformed by 0.79 m RTIL. After 200 cycles, 0.79 m RTIL achieves a discharge capacity of 112 mAh/g. When comparing the capacity retention values of the electrolytes, 0.79 m RTIL surpasses LP40 with 86.8% compared to 84.8%. Since 3 m RTIL catches up in the end, its capacity retention is close to LP40 with 84%. When it comes to the coulombic efficiency in Figure 4.2.1b, the RTILs show superior results than LP40 with efficiencies above 99%, indicating that the fraction of side reactions is negligible [66]. It should however be mentioned that the CE of LP40 in this case can be considered somewhat low with its 95-96%. It can be observed that the CE of the 3 m RTIL is a bit higher than in 0.79 m RTIL, but the difference is minimal. Altogether, it can be established that the low-concentrated RTIL performs significantly better than the high-concentrated RTIL.

The potential profiles of 0.79 and 3 m RTIL for selected cycles throughout the 200 cycles are presented in Figure 4.2.2b and 4.2.2c, respectively. Overall, the

behaviour of 0.79 m RTIL is close to the behaviour of LP40, with all the potential plateaus present and a similar gap size between the charge and discharge curves, indicating the same degree of polarisation. The dissimilarity is however that the 0.79 m RTIL has a steadier fade in discharge capacity than LP40, which experiences a drop from 1 to 50 cycles. Even though the 3 m RTIL also displays all potential plateaus, it differs in terms of larger charge/discharge gap and thus indicating more polarisation, and a more rapid capacity decay, especially until 100 cycles.

There is a lack of studies where LNMO is combined with the same RTIL (LiFSI in $P_{111i4}FSI$), which complicates the comparison of the achieved performance with the literature. However, some publications can be considered comparable and worth discussing. Salem et al. studied a half cell configuration with different cathode materials, including LNMO, and an electrolyte system consisting of 0.5 M $LiPF_6$ in $P_{111i4}FSI$ [40]. While working well with LFP, the the high-potential cells with LNMO failed to produce any capacity even at a low C-rate of C/12, pointing at the reactivity between the RTIL and the cations in the active material as the possible reason to the malfunctioning. The similar electrolyte system in this thesis, where only the salt dissolved in the RTIL differs, proves that $P_{111i4}FSI$ cope with the high voltage.

Forsyth et al. investigated an identical electrolyte system as in this thesis, consisting of different concentrations of the salt LiFSI in $P_{111i4}FSI$ [8]. They discovered that in spite of an increase in viscosity, and thus a reduction in conductivity, the alkali metal cation transference number improved. Additionally, this gave rise to substantial improvements in the electrochemical stability and performance of the cells. These findings suggested that the high-concentrated RTIL would possibly perform better than the low-concentrated RTIL, which did not match the results of this thesis.

Even though the performance of LP40 and the RTILs are rather similar, the difference between them is more visible at higher C-rates, as expressed in the rate test in Figure 4.2.3. While LP40 displays a stable discharge capacity in Figure 4.2.3a, also at higher C-rates, the RTILs show variation among high and low rates. 0.79 m RTIL starts off at a higher capacity than LP40, but then shows a stair-like behaviour with increasing C-rates. At especially 2C, the difference between LP40 and the RTIL is substantial. Although the 3 m RTIL begins at a lower discharge capacity than the others, the effect shown in the low-concentrated RTIL is further

escalated. The fact that the capacity increases to a level up towards the initial values indicates that the capacity decay at high C-rates for the RTILs are mainly limited by kinetics of the electrolyte, and not due to severe degradation of the active material [60]. In terms of coulombic efficiency, all the electrolytes exhibit similar values until C/2, when the 3 m RTIL starts deviating from the others. A well descriptive phenomena for the comparison of the electrolytes is occurring when increasing the C-rate from 1C to 2C. It is a typical behaviour that the CE slightly drops when increasing the C-rate, as electrolyte kinetics restricts the flow of lithium ions. However, the effect is further strengthened for the RTILs and the highly concentrated RTIL in particular, which shows that there is a significant difference in the amount of lithium ions which are extracted compared to inserted in the cathode material. When decreasing the C-rate again to C/10 the opposite happens. This supports the assumption that the RTILs are more kinetically limited than LP40, with 3 m RTIL being the poorest, and is expected in the view of the higher ohmic resistance.

The Nyquist plot presented in Figure 4.2.4 gives an indication of the difference in ohmic resistance among the electrolytes. Even though other various factors affect the resistance, such as the different separators used for LP40 and the RTILs, the electrolyte is considered as dominating the cell's ohmic resistance [47]. Despite that impedance measurements often involve fitting of the data, the presented Nyquist plot is a valid indicator of the variation of resistances. As mentioned, LP40 shows a low resistance under 10 Ω. 0.79 m RTIL displays a resistance in the same order of magnitude as LP40, starting at around 20 Ω. The high-concentrated RTIL exhibits a significantly higher resistance of approximately 150 Ω, which indicates that a higher salt concentration leads to increased ohmic resistance, as anticipated. Similars result were arrived at by Forsyth et al. [8].

5.2.2 Post-Mortem Observations of the Electrodes

A comparison of the SEM images of post-mortem LNMO electrodes with the different electrolytes after 200 cycles, including pristine material, can be viewed in Figure 4.3.1. These images show that the surface of 0.79 m RTIL is appearing similarly to the pristine material, with the particle surfaces still intact. The previously discussed surface layer in LP40 is not visible in the RTILs either, which may indicate that the layer is formed due to the carbonate-based solvent. The point where the 0.79 m RTIL resembles LP40 is regarding the carbon/binder network surrounding the particles, and in some areas also cover them. Despite that, it can be concluded that the electrode material has been better preserved in the low-

concentrated RTIL than LP40. The high-concentrated RTIL does however cause changes in the surface of some of the LNMO particles. Additionally, the edges of the particles appear differently, and the particles are linked together, probably caused by the higher viscosity of the 3 m RTIL. The underlying particles are also more or less covered by the carbon/binder network. The Raman spectra comparison after 200 cycles in Figure 4.3.2 and the intensity ratios in Table 4.3.1 supports the observations in the SEM images. The spectrum of the low-concentrated RTIL behaves almost as the spectrum of LP40 and exhibits an intensity ratio closer to the pristine material than LP40, indicating that at least the Ni content is better preserved after 200 cycles. The same tendency was observed with another FSI^{-1}-based ionic liquid [65]. The high-concentrated RTIL displays a quite different spectrum compared to 0.79 m RTIL and LP40. Especially the Ni peaks have almost vanished, and the strongest peak takes shape more as a shoulder to the Mn peak, resulting in an intensity ratio of 0.63. This confirms the assumption that the active material in the highly concentrated RTIL has been depleted. Furthermore, a peak at a higher Raman shift can be found in the spectrum of 3 m RTIL, which will be assessed in detail in the evaluation of the 3 m RTIL after 50 and 200 cycles below.

Observations of the low-concentrated RTIL both after 50 and 200 cycles in Section 4.3.2 contributes to a more comprehensive evaluation of the behaviour during long-term cycling. The comparison of 0.79 m RTIL after 50 cycles in Figure 4.3.9b and 200 cycles in Figure 4.3.9c indicate that there is minimal difference between the two cycling periods. The only observation that can be done is that the carbon/binder network is more dominating and present also at some of the LNMO particle's surfaces. The Raman spectra in Figure 4.3.10 after 50 and 200 cycles substantiate this observation, as their spectra appear identical, with only a small decrease in the intensity ratio between 50 and 200 cycles. The comparison of the EDS analyses in Figure 4.3.11 also does not show any particular difference after 50 and 200 cycles but demonstrates that the elements of the electrolyte (F, S, P and N) clearly are present in the sample, both on and around the LNMO particles. Similar observations were done in a study of another LiFSI-based ionic liquid, where elements from the salt such as S and F also showed strong signals at the surface of LNMO [67].

The comparison of the SEM images of the 3 m RTIL after 50 cycles in Figure 4.3.12b and 200 cycles in Figure 4.3.12c demonstrate that the presence of carbon/binder network is similar in both the samples. However, it may seem like the

surface of the captured LNMO particles is more degraded after 200 cycles than 50 cycles, as the surface triangles are harder to observe. The Raman spectra after 50 and 200 cycles in Figure 4.3.13 also do not indicate any particular difference, except the fact that both the spectra show that the electrode surface has significantly changed from the pristine material, with the Ni peaks almost not existing. An interesting detail which requires further attention is the peak that has arose in both the spectra around 950 cm^{-1} but can not be found in either the pristine material or with the other electrolytes. There are limited studies conducted involving Raman spectroscopy of the current RTIL, which makes it challenging to determine the origin of the peak. Additionally, Raman spectroscopy of other ionic liquids have not shown related peaks. However, one of the factors that distinguishes the current RTIL from others common RTILs is that it is phosphonium-based. Therefore, a possible source to the peak would be compounds based on phosphorous. Within battery research, there are several Raman studies on the cathode material LFP, where phosphate (PO_4^{3-}) is an essential anion. Guptka et al. showed, among other things, a dominating peak at 947 cm^{-1} corresponding to the A_g mode of (PO_4^{3-}) [68]. A similar peak is displayed, and also attributed to phosphate by Wu et al. in a Raman study of LFP [69]. On the other hand, it is not fully reasonable that this peak does not appear in the low-concentrated RTIL, as the amount of phosphorous is actually less in the high-concentrated RTIL, as presented in Table 3.2.1. Thus, it would be more logical that the peak is due to the larger amount LiFSI added to the ionic liquid, introducing also sulfate (SO_4^{2-}) or nitrate (NO_3^-) as possible sources to the peak. Sulfate gives rise to an intense peak around 977 cm^{-1} [70], while nitrate displays an intense peak around 1049 cm^{-1} [71]. Thus, phosphate matches better the peak in the spectrum of the high-concentrated RTIL. Regardless of the correct origin of the peak, it most likely indicates that it is due to decomposition of the electrolyte. The fact that the peak to some degree shift to the right, might indicate that the compound changes composition during cycling. The EDS analyses in Figure 4.3.14 display that the same elements are present as with the low-concentrated RTIL. There are some minor differences in the intensity of the elements, but not enough to compare them. A difference which however can be observed, is that after 50 cycles in Figure 4.3.14a, S and P coexist with C and avoid the particle surface. After 200 cycles, there is a carbon/binder network which covers parts of the LNMO particles, but in this case, it consists of all the electrolyte elements, in accordance with other publications [67].

5.3 Cyclability and Evaluation of LNMO without Conductive Additive

LNMO electrodes without carbon black, often added to the electrode slurry as conductive additive, were fabricated with the purpose of investigating its cyclability and if successful, determine whether samples without carbon degrade in the same manner. The reason is that carbon is believed to function as a source to side reaction and thus degrade the cell [9]. Previous observations have also showed that decomposition products tend to form on the carbon/binder network. Additionally, LNMO should be sufficiently electronically conductive to ensure cyclability [72]. Therefore, the goal was to obtain LNMO electrode with a minimal thickness (desirable with a thickness of one particle). However, the SEM images of the pristine material in Figure 4.1.4 disclose that the desired thickness of one particle was not obtained. The Raman spectrum of pristine LNMO without carbon in Figure 4.3.16 shows a very similar spectrum compared to that of LNMO with carbon, of course without the designated peaks corresponding to carbon.

Since there was an uncertainty related to whether the electrode material without carbon would function or not, a low C-rate of C/20 was chosen for the attempted cycling with both LP40 and low-concentrated RTIL. In spite of that, as indicated in Figure 4.2.5, the cells failed to produce capacity and stopped automatically after almost 20 minutes. From this experience, it can be concluded that the cyclability of at least the fabricated electrode material without carbon is absent. In an attempt to describe the reason of the failure, the electrodes of the cells were characterised post-mortem, as with the conventional electrode material. The SEM images in Figure 4.3.15 compare the pristine electrode material with the electrodes after cycling with LP40 and 0.79 m RTIL. In general, there are voids at the electrode surface, which probably will result in a poorer conductivity than if LNMO particles were covering the whole surface of the electrode. The pristine material in Figure 4.3.15a shows the characteristic surface of the active material, which becomes even clearer without carbon present. When LP40 is used as electrolyte in Figure 4.3.15b, the particle surface changes like seen with conventional LNMO, and darker spots appear although the cell did not cycle for long. This contributes to covering the triangles on the surface. With the RTIL in Figure 4.3.15c, the particle surface remains intact, and the particles are more linked together. The SEM images therefore show that there is a change in appearance when the LNMO electrode is in contact with the electrolytes, also without cycling, indicating a chemical reaction taking place. Yet, it seems like neither of the observations re-

sult in the malfunction, since both type of electrolytes fail to cycle. Thus, an inadequate conductivity is more likely to be the reason.

The Raman spectra in Figure 4.3.16 indicate whether the signal of the Ni and Mn bands have decreased and thus the active material functions as intended or not. The general observation is that all peaks are present both with LP40 and the RTIL, and the shape of the graphs are very similar to the pristine material. The intensity ratios in Table 4.3.5 also demonstrate that the nickel content is more or less preserved, especially with LP40. A drop is seen with the RTIL, but this is not decisive enough to conclude that the RTIL functions poorer, as neither of the electrolyte managed to cycle. The EDS analyses in Figure 4.3.17 show that the distribution is similar to the distributions of the electrolytes with the electrode material with carbon. It should be mentioned that the signal of the RTIL elements in Figure 4.3.17b are weaker than with LNMO with carbon. This is reasonable, as the electrolyte elements tend to concentrate in positions where carbon is present. Anyhow, there is no observable layer formed after the short cycling time. This also supports the idea that the poor conductivity is the main reason of the failed cyclability.

Chapter 6

Conclusion

The cathode active material LNMO in combination with the salt LiFSI in the RTIL $P_{111i4}FSI$ was investigated with the objective to examine its performance in comparison to the conventional electrolyte LP40, which suffers from challenges as HF formation. Additionally, it was a desire to determine whether high or low concentration of the salt LiFSI resulted in the superior performance. LNMO electrodes were fabricated and assembled in pouch cells as half cells against lithium, with either LP40, 0.79 m or 3 m LiFSI in $P_{111i4}FSI$ as electrolyte. The cells were galvanostatic cycled for 200 C/2 cycles and evaluated at higher C-rates as well. Overall, the low-concentrated RTIL outperformed the high-concentrated RTIL. The low-concentrated RTIL demonstrated a capacity retention of 86.8%, superior to 84.8% of LP40. Also, the coulombic efficiencies of the RTILs were significantly higher with >99% compared to 95-96% of LP40, indicating a lower fraction of side reactions taking place. At higher C-rates up to 2C, both concentrations of the RTIL displayed worse discharge capacity than LP40. As the capacity increased up to the initial level when decreasing the C-rate again, it is believed that electrolyte kinetics is the limiting factor, not degradation of the active material. The LNMO electrodes were characterised post-mortem with SEM, EDS and Raman spectroscopy to evaluate the degradation of the electrode after cycling. LP40 caused the formation of a surface film on the LNMO particles, with a thicker layer of the electrolyte elements after 200 cycles. The images of the low-concentrated RTIL displayed more intact LNMO particles similarly to the pristine material. The high-concentrated RTIL caused a different electrode surface, with less particles visible and a more dominant carbon/binder network surrounding the particles, probably caused by the higher viscosity. The Raman spectra and the calculated intensity ratios confirmed the observations with SEM, showing that mainly the Ni content was affected during cycling and especially for the high-concentrated RTIL. It was also in interest to fabricate and investigate the cyclability of LNMO without

a conductive carbon additive, as this is assumed to be the source of side reactions and degradation of the active material. The electrode material however failed to produce any capacity, probably due to a poor conductivity of bare LNMO.

Chapter 7

Further Work

This thesis investigated two concentrations of the RTIL, 0.79 m and 3 m, which resulting in very different cycling performance, supported by the observations that were done post-mortem. However, the range between these two concentrations is significant. Therefore, it would be interesting to evaluate concentrations in the middle, and also lower than 0.79 m, to optimise the salt concentration. This is related to the work done by Forsyth et al., who investigated a wide range of salt concentrations in the RTIL [8]. With RTILs there is a trade off when it comes to sacrificing conductivity and at the same time utilise the benefits of a higher salt concentrations, thus it would be of interest to investigate this in the future.

All the cycling data obtained in this thesis was based on cycling at room temperature, but that it not necessarily the case in reality. For that reason, it would be fascinating to cycle the cells in a wider temperature range, especially at elevated temperatures. It is also known that the conductivity of RTILs improve when increasing the temperature, making the RTILs even more competitive compared to conventional carbonate-based electrolytes.

In this thesis, Raman spectroscopy has been utilised extensively for post-mortem characterisation of the cycled LNMO electrodes compared to the pristine electrodes. This has led to interesting observations, such as that particularly the nickel peaks decrease in intensity compared to the manganese peaks, and also that the high-concentrated RTIL showed a very different spectrum than those of LP40 and the low-concentrated RTIL. In the beginning of the work with thesis, is was an aim to develop a procedure for in-situ Raman spectroscopy, which would give the possibility to better understand the degradation of the electrode during cycling. Unfortunately, there were problems with the special cell that would make it achievable. Thus, it would be useful to resume this work.

Another aim of this thesis was to fabricate LNMO electrodes without conductive carbon additive, to investigate whether electrodes without carbon degrade in the same manner as with carbon. This was based on the author's own observations that decomposition products tend to form on the carbon additive, and also that the literature points towards carbon being the source to unwanted side reactions [9]. However, it proved to be challenging to produce thin enough electrode material, which probably led to a poor conductivity. Hence, a goal for future work could be to continue the attempt of casting electrode material with a one-particle thickness, hopefully increasing the conductivity and cyclability of the material.

References

[1] H Lee, K Calvin, and D Dasgupta. *Synthesis Report of the IPCC Sixth Assessment Report (AR6): Summary for Policymakers.* Tech. rep. Intergovernmental Panel on Climate Change, 2023.

[2] Christian Julien et al. *Lithium Batteries: Science and Technology*. eng. Cham: Springer International Publishing AG, 2015. ISBN: 3319191071.

[3] IEA. *Global EV Outlook 2023*. Tech. rep. Paris, 2023.

[4] IEA. *Average pack price of lithium-ion batteries and share of cathode material cost, 2011-2021*. Tech. rep. Paris, 2022.

[5] Gemeng Liang et al. "Developing high-voltage spinel LiNi0.5Mn1.5O4 cathodes for high-energy-density lithium-ion batteries: current achievements and future prospects". eng. In: *Journal of materials chemistry. A, Materials for energy and sustainability* 8.31 (2020), pp. 15373–15398. ISSN: 2050-7488.

[6] Nicholas P.W. Pieczonka et al. "Understanding transition-metal dissolution behavior in LiNi 0.5Mn1.5O4 high-voltage spinel for lithium ion batteries". In: *Journal of Physical Chemistry C* 117.31 (Aug. 2013), pp. 15947–15957. ISSN: 19327447. DOI: 10.1021/jp405158m.

[7] Neha Chawla, Neelam Bharti, and Shailendra Singh. *Recent advances in non-flammable electrolytes for safer lithium-ion batteries*. Mar. 2019. DOI: 10.3390/batteries5010019.

[8] M. Forsyth et al. "Inorganic-Organic Ionic Liquid Electrolytes Enabling High Energy-Density Metal Electrodes for Energy Storage". In: *Electrochimica Acta* 220 (Dec. 2016), pp. 609–617. ISSN: 00134686. DOI: 10.1016/j.electacta.2016.10.134.

[9] Wangda Li et al. "Dynamic behaviour of interphases and its implication on high-energy-density cathode materials in lithium-ion batteries". In: *Nature Communications* 8 (2017). ISSN: 20411723. DOI: 10.1038/ncomms14589.

[10] John B Goodenough and Kyu-Sung Park. "The Li-Ion Rechargeable Battery: A Perspective". eng. In: *Journal of the American Chemical Society* 135.4 (2013), pp. 1167–1176. ISSN: 0002-7863.

[11] Burak Aktekin et al. "The Effect of the Fluoroethylene Carbonate Additive in LiNi0.5Mn1.5O4 - Li4Ti5O12 Lithium-Ion Cells". In: *Journal of The Electrochemical Society* 164.4 (2017), A942–A948. ISSN: 0013-4651. DOI: 10.1149/2.0231706jes.

[12] M Stanley Whittingham. "Lithium Batteries and Cathode Materials". eng. In: *Chemical reviews* 104.10 (2004), pp. 4271–4302. ISSN: 0009-2665.

[13] Zhaolin Liu, Aishui Yu, and Jim Y Lee. "Synthesis and characterization of LiNi[1-x-y]Co[x]Mn[y]O[2] as the cathode materials of secondary lithium batteries". In: *Journal of power sources* 81-82 (1999), pp. 416–419. ISSN: 0378-7753. DOI: 10.1016/S0378-7753(99)00221-9.

[14] Samuel G. Booth et al. *Perspectives for next generation lithium-ion battery cathode materials*. Oct. 2021. DOI: 10.1063/5.0051092.

[15] Abdulrahman Shahul Hameed. *Phosphate Based Cathodes and Reduced Graphene Oxide Composite Anodes for Energy Storage Applications*. Singapore: Springer Singapore, 2016, pp. 1–30. ISBN: 978-981-10-2301-9. DOI: 10.1007/978-981-10-2302-6.

[16] Hyung Joo Noh et al. "Comparison of the structural and electrochemical properties of layered Li[NixCoyMnz]O2 (x = 1/3, 0.5, 0.6, 0.7, 0.8 and 0.85) cathode material for lithium-ion batteries". In: *Journal of Power Sources* 233 (2013), pp. 121–130. ISSN: 03787753. DOI: 10.1016/j.jpowsour.2013.01.063.

[17] Weikang Li et al. "Enabling high areal capacity for Co-free high voltage spinel materials in next-generation Li-ion batteries". In: *Journal of Power Sources* 473 (Oct. 2020). ISSN: 03787753. DOI: 10.1016/j.jpowsour.2020.228579.

[18] Koichi Momma and Fujio Izumi. "VESTA 3 for three-dimensional visualization of crystal, volumetric and morphology data". In: *Journal of Applied Crystallography* 44.6 (Dec. 2011), pp. 1272–1276. ISSN: 00218898. DOI: 10.1107/S0021889811038970.

[19] Xiao Long Xu et al. *Research progress in improving the cycling stability of high-voltage LiNi0.5Mn1.5O4 cathode in lithium-ion battery*. Apr. 2017. DOI: 10.1007/s40820-016-0123-3.

[20] Muharrem Kunduraci, Jafar F. Al-Sharab, and Glenn G. Amatucci. "High-power nanostructured LiMn[2-x]Ni[x]O[4] high-voltage lithium-ion battery electrode materials: Electrochemical impact of electronic conductivity and morphology". In: *Chemistry of Materials* 18.15 (July 2006), pp. 3585–3592. ISSN: 08974756. DOI: 10.1021/cm060729s.

[21] M. Kunduraci and G. G. Amatucci. "Synthesis and Characterization of Nanostructured 4.7 V LixMn1.5Ni0.5O4 Spinels for High-Power Lithium-Ion Batteries". In: *Journal of The Electrochemical Society* 153.7 (2006), A1345. ISSN: 00134651. DOI: 10.1149/1.2198110.

[22] Shiyuan Zhou et al. "Hierarchical LiNi0.5Mn1.5O4 micro-rods with enhanced rate performance for lithium-ion batteries". In: *Journal of Materials Science* 53.13 (July 2018), pp. 9710–9720. ISSN: 15734803. DOI: 10.1007/s10853-018-2272-x.

[23] Claire Chunjuan Zhang et al. "Raman Spectroscopy Characterization of Amorphous Coke Generated in Industrial Processes". In: *ACS Omega* 7.3 (Jan. 2022), pp. 2565–2570. ISSN: 24701343. DOI: 10.1021/acsomega.1c03456.

[24] Ting Feng Yi, Jie Mei, and Yan Rong Zhu. *Key strategies for enhancing the cycling stability and rate capacity of LiNi0.5Mn1.5O4 as high-voltage cathode materials for high power lithium-ion batteries*. June 2016. DOI: 10.1016/j.jpowsour.2016.03.070.

[25] Philipp Jehnichen, Klaus Wedlich, and Carsten Korte. "Degradation of high-voltage cathodes for advanced lithium-ion batteries–differential capacity study on differently balanced cells". In: *Science and Technology of Advanced Materials* 20.1 (Jan. 2019), pp. 1–9. ISSN: 18785514. DOI: 10.1080/14686996.2018.1550625.

[26] Li Yang, Boris Ravdel, and Brett L. Lucht. "Electrolyte Reactions with the Surface of High Voltage LiNi0.5Mn1.5O4 Cathodes for Lithium-Ion Batteries". In: *Electrochemical and Solid-State Letters* 13.8 (2010), A95. ISSN: 10990062. DOI: 10.1149/1.3428515.

[27] Takayuki Aoshima et al. "Mechanisms of manganese spinels dissolution and capacity fade at high temperature". In: *Journal of Power Sources* 97-98 (July 2001), pp. 377–380. ISSN: 03787753. DOI: 10.1016/S0378-7753(01)00551-1.

[28] Subrahmanyam Goriparti et al. *Review on recent progress of nanostructured anode materials for Li-ion batteries*. July 2014. DOI: 10.1016/j.jpowsour.2013.11.103.

[29] J O Besenhard and G Eichinger. "High energy density lithium cells: Part I. Electrolytes and anodes". In: *Journal of Electroanalytical Chemistry and Interfacial Electrochemistry* 68.1 (1976), pp. 1–18. ISSN: 0022-0728. DOI: https://doi.org/10.1016/S0022-0728(76)80298-7. URL: https://www.sciencedirect.com/science/article/pii/S0022072876802987.

[30] Xiao Guang Yang et al. "Fast charging of lithium-ion batteries at all temperatures". In: *Proceedings of the National Academy of Sciences of the United States of America* 115.28 (July 2018), pp. 7266–7271. ISSN: 10916490. DOI: 10.1073/pnas.1807115115.

[31] Zewen Zhang et al. "Cathode-Electrolyte Interphase in Lithium Batteries Revealed by Cryogenic Electron Microscopy". In: *Matter* 4.1 (Jan. 2021), pp. 302–312. ISSN: 25902385. DOI: 10.1016/j.matt.2020.10.021.

[32] Kang Xu. "Nonaqueous liquid electrolytes for lithium-based rechargeable batteries". In: *Chemical Reviews* 104.10 (Oct. 2004), pp. 4303–4417. ISSN: 00092665. DOI: 10.1021/cr030203g.

[33] Ken Tasaki et al. "Decomposition of LiPF6 and stability of PF5 in Li-Ion battery electrolytes. Density functional theory and molecular dynamics studies". In: *Journal of the Electrochemical Society* 150.12 (2003), A1628–A1636. ISSN: 0013-4651. DOI: 10.1149/1.1622406.

[34] Yuanli Cai et al. "Synthesis, application and industrialization of LiFSI: A review and perspective". eng. In: *Journal of power sources* 535 (2022), p. 231481. ISSN: 0378-7753.

[35] Sheng Shui Zhang. "A review on electrolyte additives for lithium-ion batteries". In: *Journal of Power Sources* 162.2 SPEC. ISS. (Nov. 2006), pp. 1379–1394. ISSN: 03787753. DOI: 10.1016/j.jpowsour.2006.07.074.

[36] Maciej Galiński, Andrzej Lewandowski, and Izabela Stepniak. *Ionic liquids as electrolytes*. Aug. 2006. DOI: 10.1016/j.electacta.2006.03.016.

[37] Ali Eftekhari, Yang Liu, and Pu Chen. *Different roles of ionic liquids in lithium batteries*. Dec. 2016. DOI: 10.1016/j.jpowsour.2016.10.025.

[38] A. Guerfi, A. Vijh, and K. Zaghib. "Safe Lithium Rechargeable Batteries Based on Ionic Liquids". In: *Lithium Batteries*. Hoboken, NJ, USA: John Wiley & Sons, Inc., June 2013, pp. 291–326. DOI: 10.1002/9781118615515.ch14.

[39] G. M.A. Girard et al. "Electrochemical and physicochemical properties of small phosphonium cation ionic liquid electrolytes with high lithium salt content". In: *Physical Chemistry Chemical Physics* 17.14 (Apr. 2015), pp. 8706–8713. ISSN: 14639076. DOI: 10.1039/c5cp00205b.

[40] Nuha Salem et al. "Physical and Electrochemical Properties of Some Phosphonium-Based Ionic Liquids and the Performance of Their Electrolytes in Lithium-Ion Batteries". In: *Journal of The Electrochemical Society* 164.8 (2017), H5202–H5209. ISSN: 0013-4651. DOI: 10.1149/2.0061708jes.

[41] Junyoung Mun et al. "Surface Film Formation on LiNi0.5Mn1.5O4 Electrode in an Ionic Liquid Solvent at Elevated Temperature". In: *Journal of The Electrochemical Society* 158.5 (2011), A453. ISSN: 00134651. DOI: 10.1149/1.3560205.

[42] Sheng Shui Zhang. "A review on the separators of liquid electrolyte Li-ion batteries". In: *Journal of Power Sources* 164.1 (Jan. 2007), pp. 351–364. ISSN: 03787753. DOI: 10.1016/j.jpowsour.2006.10.065.

[43] Frank Richter et al. "Thermal conductivity and internal temperature profiles of Li-ion secondary batteries". In: *Journal of Power Sources* 359 (2017), pp. 592–600. ISSN: 03787753. DOI: 10.1016/j.jpowsour.2017.05.045.

[44] Jiadeng Zhu et al. "Understanding glass fiber membrane used as a novel separator for lithium-sulfur batteries". In: *Journal of Membrane Science* 504 (Apr. 2016), pp. 89–96. ISSN: 18733123. DOI: 10.1016/j.memsci.2016.01.020.

[45] Lorenzo Zolin. *Large-scale Production of Paper-based Li-ion Cells*. Cham: Springer International Publishing, 2017, pp. 55–66. ISBN: 978-3-319-39015-4. DOI: 10.1007/978-3-319-39016-1.

[46] Alexandros Ch Lazanas and Mamas I. Prodromidis. "Electrochemical Impedance Spectroscopy - A Tutorial". In: *ACS Measurement Science Au* (2022). ISSN: 2694250X. DOI: 10.1021/acsmeasuresciau.2c00070.

[47] Kieran Mc Carthy et al. "Review—Use of Impedance Spectroscopy for the Estimation of Li-ion Battery State of Charge, State of Health and Internal Temperature". In: *Journal of The Electrochemical Society* 168.8 (Aug. 2021), p. 080517. ISSN: 0013-4651. DOI: 10.1149/1945-7111/ac1a85.

[48] Hery Mitsutake, Ronei J. Poppi, and Márcia C. Breitkreitz. "Raman Raman imaging imaging spectroscopy: Spectroscopy: History, history, fundamentals fundamentals and current and current scenario scenario of the oftechnique the technique". In: *Journal of the Brazilian Chemical Society* 30.11 (2019), pp. 2243–2258. ISSN: 16784790. DOI: 10.21577/0103-5053.20190116.

[49] Gustavo M. Do Nascimento. "Introductory Chapter: The Multiple Applications of Raman Spectroscopy". In: *Raman Spectroscopy*. InTech, Apr. 2018. DOI: 10.5772/intechopen.75795.

[50] Ado Jorio et al. "Measuring disorder in graphene with the G and D bands". In: *Physica Status Solidi (B) Basic Research* 247.11-12 (Dec. 2010), pp. 2980–2982. ISSN: 03701972. DOI: 10.1002/pssb.201000247.

[51] Jarle Hjelen. *Scanning elektron-mikroskopi*. nob. Trondheim: SINTEF, 1989.

[52] Morten Onsrud et al. "Novel carbon coating on aluminum current collectors for lithium-ion batteries". In: *SN Applied Sciences* 4.8 (Aug. 2022). ISSN: 25233971. DOI: 10.1007/s42452-022-05103-y.

[53] Fabienne Huttner et al. "Increased Moisture Uptake of NCM622 Cathodes after Calendering due to Particle Breakage". In: *Journal of The Electrochemical Society* 168.9 (Sept. 2021), p. 090539. ISSN: 0013-4651. DOI: 10.1149/1945-7111/ac24bb.

[54] Christiane Schilcher, Chris Meyer, and Arno Kwade. "Structural and Electrochemical Properties of Calendered Lithium Manganese Oxide Cathodes". In: *Energy Technology* 4.12 (Dec. 2016), pp. 1604–1610. ISSN: 21944296. DOI: 10.1002/ente.201600130.

[55] Elise R. Østli et al. "Limitations of Ultrathin Al2O3Coatings on LNMO Cathodes". In: *ACS Omega* 6.45 (Nov. 2021), pp. 30644–30655. ISSN: 24701343. DOI: 10.1021/acsomega.1c04457.

[56] Mika Serna Malmer. *Combining LiNi0.5Mn1.5O4 Cathodes with Lithium Bis(fluorosulfonyl)imide-based Electrolytes*. Tech. rep. Trondheim: NTNU - Department of Materials Science and Engineering, Dec. 2022.

[57] Xingwen Yu, Wiley A. Yu, and Arumugam Manthiram. "Advances and Prospects of High-Voltage Spinel Cathodes for Lithium-Based Batteries". In: *Small Methods* 5.5 (May 2021). ISSN: 23669608. DOI: 10.1002/smtd.202001196.

[58] Haibo Rong et al. "Enhanced cyclability of LiNi0.5Mn1.5O4 cathode in carbonate based electrolyte with incorporation of tris(trimethylsilyl)phosphate (TMSP)". In: *Journal of Power Sources* 261 (Sept. 2014), pp. 148–155. ISSN: 03787753. DOI: 10.1016/j.jpowsour.2014.03.032.

[59] Philipp Jehnichen, Klaus Wedlich, and Carsten Korte. "Degradation of high-voltage cathodes for advanced lithium-ion batteries–differential capacity study on differently balanced cells". In: *Science and Technology of Advanced Materials* 20.1 (Jan. 2019), pp. 1–9. ISSN: 18785514. DOI: 10.1080/14686996.2018.1550625.

[60] Elise R. Østli et al. "On the Durability of Protective Titania Coatings on High-Voltage Spinel Cathodes". In: *ChemSusChem* 15.12 (June 2022). ISSN: 1864564X. DOI: 10.1002/cssc.202200324.

[61] Changsheng Qiu et al. "The polarization characteristics of lithium-ion batteries under cyclic charge and discharge". In: *Journal of Solid State Electrochemistry* 23.6 (June 2019), pp. 1887–1902. ISSN: 14328488. DOI: 10.1007/s10008-019-04282-w.

[62] Honghe Zheng et al. "A comprehensive understanding of electrode thickness effects on the electrochemical performances of Li-ion battery cathodes". In: *Electrochimica Acta* 71 (June 2012), pp. 258–265. ISSN: 00134686. DOI: 10.1016/j.electacta.2012.03.161.

[63] Jianling Guo et al. "Preparation and electrochemical performance of LiNi0.5Mn1.5O4 spinels with different particle sizes and surface orientations as cathode materials for lithium-ion battery". In: *Journal of Materials Science* 55.27 (Sept. 2020), pp. 13157–13176. ISSN: 15734803. DOI: 10.1007/s10853-020-04973-0.

[64] Xingyu Wang et al. "Adiponitrile as Lithium-Ion Battery Electrolyte Additive: A Positive and Peculiar Effect on High-Voltage Systems". In: *ACS Applied Energy Materials* 1.10 (Oct. 2018), pp. 5347–5354. ISSN: 25740962. DOI: 10.1021/acsaem.8b00968.

[65] Yu Qiao et al. "High-Voltage Li-Ion Full-Cells with Ultralong Term Cycle Life at Elevated Temperature". In: *Advanced Energy Materials* 8.33 (Nov. 2018). ISSN: 16146840. DOI: 10.1002/aenm.201802322.

[66] Fangfang Yang et al. "A study of the relationship between coulombic efficiency and capacity degradation of commercial lithium-ion batteries". In: *Energy* 145 (Feb. 2018), pp. 486–495. ISSN: 03605442. DOI: 10.1016/j.energy.2017.12.144.

[67] Elise R. Østli et al. "Stabilizing the Cathode Interphase of LNMO using an Ionic-liquid based Electrolyte". In: *Batteries & Supercaps* (June 2023). ISSN: 2566-6223. DOI: 10.1002/batt.202300085. URL: https://chemistry-europe.onlinelibrary.wiley.com/doi/10.1002/batt.202300085.

[68] Reema Gupta et al. “Effect of manganese doping on conduction in olivine LiFePO4”. In: *Journal of Materials Science: Materials in Electronics* 28.7 (Apr. 2017), pp. 5192–5199. ISSN: 1573482X. DOI: 10.1007/s10854-016-6175-9.

[69] Jing Wu et al. “In situ Raman spectroscopy of LiFePO4: Size and morphology dependence during charge and self-discharge”. In: *Nanotechnology* 24.42 (Oct. 2013). ISSN: 09574484. DOI: 10.1088/0957-4484/24/42/424009.

[70] Alexander Börger et al. “On the use of Raman microscopy for sulfation analysis in lead-acid battery research”. In: *Journal of Energy Storage* 12 (Aug. 2017), pp. 305–310. ISSN: 2352152X. DOI: 10.1016/j.est.2017.05.011.

[71] Marc D. Fontana, Kawther Ben Mabrouk, and Thomas H. Kauffmann. “Raman spectroscopic sensors for inorganic salts”. In: *Spectroscopic Properties of Inorganic and Organometallic Compounds* 44 (2013), pp. 40–67. ISSN: 14651939. DOI: 10.1039/9781849737791-00040.

[72] Shuo Yang et al. “Electrochemical and electronic charge transport properties of Ni-doped LiMn2O4 spinel obtained from polyol-mediated synthesis”. In: *Materials* 11.5 (May 2018). ISSN: 19961944. DOI: 10.3390/ma11050806.

Appendix A - Formula of LNMO Electrode Slurry

The exact amounts of each electrode slurry component are presented in Table B.1. As a basis for the slurry formula, the start weight of LNMO was set to 0.75 g, and the distribution was 90 wt% LNMO, 5 wt% carbon black and 5 wt% PVDF. For the viscosity, a ratio between NMP and solids of 2:1 was used. It was casted on double sided carbon coated Al foil with a 100 µm bar.

Table B.1: Formula of LNMO electrode slurry with carbon.

Component	Weight percentage [wt-%]	Calculated weight [g]	Actual weight [g]	Actual weight percentage [wt-%]
LNMO	90	0.7500	0.7516	89.7553
Carbon black	5	0.0417	0.0422	5.0502
PVDF	5	0.0417	0.0418	5.0030
PVDF in NMP (5%)	-	0.8333	0.8361	-
Extra NMP	-	0.8750	0.8772	-
Total NMP	-	-	1.6715	-
Total LNMO+carbon black+PVDF	-	-	0.8356	-
Total slurry	-	-	2.5071	-
Ratio (NMP/solid)	2.0003			

Appendix B - Formulas of LNMO Electrode Slurries without Carbon

The exact amounts of each electrode slurry component are presented in Table B.1 to B.4. As a basis for the slurry formula, the start weight of LNMO was set to 0.75 g, and the distribution was 95 wt% LNMO and 5 wt% PVDF. For the viscosity, a ratio between NMP and solids varied between the casts from 1:1 to 1.5:1. The gap size of the casting bar used was 50 and 30 µm. The most successful cast was number 6, with an NMP:solid ratio of 1:1 and 30 µm gap size.

B1

Table B.1: Formula of LNMO electrode slurry without carbon (number 4). Casted on Al foil without carbon coating, using a 50 µm bar. No additonal NMP was added.

Component	Weight percentage [wt-%]	Calculated weight [g]	Actual weight [g]	Actual weight percentage [wt-%]
LNMO	95	0.7500	0.7504	94.8413
PVDF	5	0.0395	0.0404	5.1082
PVDF in NMP (5%)	-	0.7895	0.8079	-
Extra NMP	-	-	-	-
Total NMP	-	-	0.7675	-
Total LNMO+PVDF	-	-	0.7908	-
Total slurry	-	-	1.5583	-
Ratio (NMP/solid)			0.9705	

B2

Table B.2: Formula of LNMO electrode slurry without carbon (number 5). Casted on Al foil without carbon coating, using a 50 µm bar. Additonal NMP was added, resulted in too low viscosity and no usable cast.

Component	Weight percentage [wt-%]	Calculated weight [g]	Actual weight [g]	Actual weight percentage [wt-%]
LNMO	95	0.7500	0.7503	95.0522
PVDF	5	0.0395	0.0387	4.9098
PVDF in NMP (5%)	-	0.7895	0.7748	-
Extra NMP	-	0.4342	0.4332	-
Total NMP	-	-	1.1693	-
Total LNMO+PVDF	-	-	0.7890	-
Total slurry	-	-	1.9583	-
Ratio (NMP/solid)			1.4819	

B3

Table B.3: Formula of LNMO electrode slurry without carbon (number 6). Casted on Al foil without carbon coating, using a 30 µm bar. No additonal NMP was added.

Component	Weight percentage [wt-%]	Calculated weight [g]	Actual weight [g]	Actual weight percentage [wt-%]
LNMO	95	0.7500	0.7496	94.9842
PVDF	5	0.0395	0.0400	5.0665
PVDF in NMP (5%)	-	0.7895	0.8001	-
Extra NMP	-	-	-	-
Total NMP	-	-	0.7601	-
Total LNMO+PVDF	-	-	0.7896	-
Total slurry	-	-	1.5497	-
Ratio (NMP/solid)			0.9626	

B4

Table B.4: Formula of LNMO electrode slurry without carbon (number 7). Casted on Al foil without carbon coating, using a 30 µm bar. Additonal NMP was added, resulted in too low viscosity and no usable cast.

Component	Weight percentage [wt-%]	Calculated weight [g]	Actual weight [g]	Actual weight percentage [wt-%]
LNMO	95	0.7500	0.7500	95.0570
PVDF	5	0.0395	0.0390	4.9430
PVDF in NMP (5%)	-	0.7895	0.7800	-
Extra NMP	-	0.1974	0.2020	-
Total NMP	-	-	0.9430	-
Total LNMO+PVDF	-	-	0.7890	-
Total slurry	-	-	1.7320	-
Ratio (NMP/solid)		1.1952		

Appendix C - Overview of Assembled Cells

Table C.1: Overview of assembled cells. 1.x, 2.x and further refer to different series of cells, where 1.x consists of identical cells. Wrong electrolyte/separator combination resulted in the malfunction of series 1.x and 2.x.

Cell	Electrode	Cast	Counter Electrode	Electrolyte	Separator	Cycling Program
1.1	LNMO	23.01.23	Li	1M LiPF6 in EC/DMC	Celgard 2325	-
1.2	LNMO	23.01.23	Li	1M LiPF6 in EC/DMC	Celgard 2325	-
1.3	LNMO	23.01.23	Li	1M LiPF6 in EC/DMC	Celgard 2325	-
1.4	LNMO	23.01.23	Li	1M LiPF6 in EC/DMC	Celgard 2325	-
1.5	LNMO	23.01.23	Li	1M LiPF6 in EC/DMC	Celgard 2325	-
2.1	LNMO	Other	Li	1M LiPF6 in EC/DMC	Celgard 2325	-
2.2	LNMO	Other	Li	1M LiPF6 in EC/DMC	Celgard 2325	-
3.1	LNMO	19.09.22	Li	1M LiPF6 in EC/DEC	Celgard 2325	50 C/2
3.2	LNMO	19.09.22	Li	1M LiPF6 in EC/DEC	Celgard 2325	50 C/2
4.1	LNMO	23.01.23	Li	1M LiPF6 in EC/DEC	Celgard 2325	200 C/2
4.2	LNMO	23.01.23	Li	1M LiPF6 in EC/DEC	Celgard 2325	100 C/2

4.3	LNMO	23.01.23	Li	1M LiPF6 in EC/DEC	Celgard 2325	Rate test
4.4	LNMO	23.01.23	Li	1M LiPF6 in EC/DEC	Celgard 2325	Rate test
5.1	LNMO	23.01.23	Li	0.79 m LiFSI in P111i4FSI	2 Freudenberg + GF	50 C/2
5.2	LNMO	23.01.23	Li	0.79 m LiFSI in P111i4FSI	2 Freudenberg + GF	200 C/2
5.3	LNMO	23.01.23	Li	0.79 m LiFSI in P111i4FSI	2 Freudenberg + GF	50 C/2
5.4	LNMO	23.01.23	Li	0.79 m LiFSI in P111i4FSI	2 Freudenberg + GF	200 C/2
5.5	LNMO	23.01.23	Li	0.79 m LiFSI in P111i4FSI	2 Freudenberg + GF	Rate test
5.6	LNMO	23.01.23	Li	0.79 m LiFSI in P111i4FSI	2 Freudenberg + GF	Rate test
6.1	LNMO	23.01.23	Li	3 m LiFSI in P111i4FSI	2 Freudenberg + GF	50 C/2
6.2	LNMO	23.01.23	Li	3 m LiFSI in P111i4FSI	2 Freudenberg + GF	200 C/2
6.3	LNMO	23.01.23	Li	3 m LiFSI in P111i4FSI	2 Freudenberg + GF	50 C/2
6.4	LNMO	23.01.23	Li	3 m LiFSI in P111i4FSI	2 Freudenberg + GF	200 C/2
6.5	LNMO	23.01.23	Li	3 m LiFSI in P111i4FSI	2 Freudenberg + GF	Rate test
6.6	LNMO	23.01.23	Li	3 m LiFSI in P111i4FSI	2 Freudenberg + GF	Rate test
6.7	LNMO	23.01.23	Li	3 m LiFSI in P111i4FSI	2 Freudenberg + GF	Rate test
6.8	LNMO	23.01.23	Li	3 m LiFSI in P111i4FSI	2 Freudenberg + GF	Rate test
6.9	LNMO	23.01.23	Li	3 m LiFSI in P111i4FSI	2 Freudenberg + GF	Rate test
7.1	LNMO without C	23.03.23 (Nr 6)	Li	1M LiPF6 in EC/DEC	Celgard 2325	C/20

7.2	LNMO without C	23.03.23 (Nr 6)	Li	1M LiPF6 in EC/DEC	Celgard 2325	C/20
8.1	LNMO without C	23.03.23 (Nr 6)	Li	0.79 m LiFSI in P111i4FSI	2 Freudenberg + GF	C/20
8.2	LNMO without C	23.03.23 (Nr 6)	Li	0.79 m LiFSI in P111i4FSI	2 Freudenberg + GF	C/20

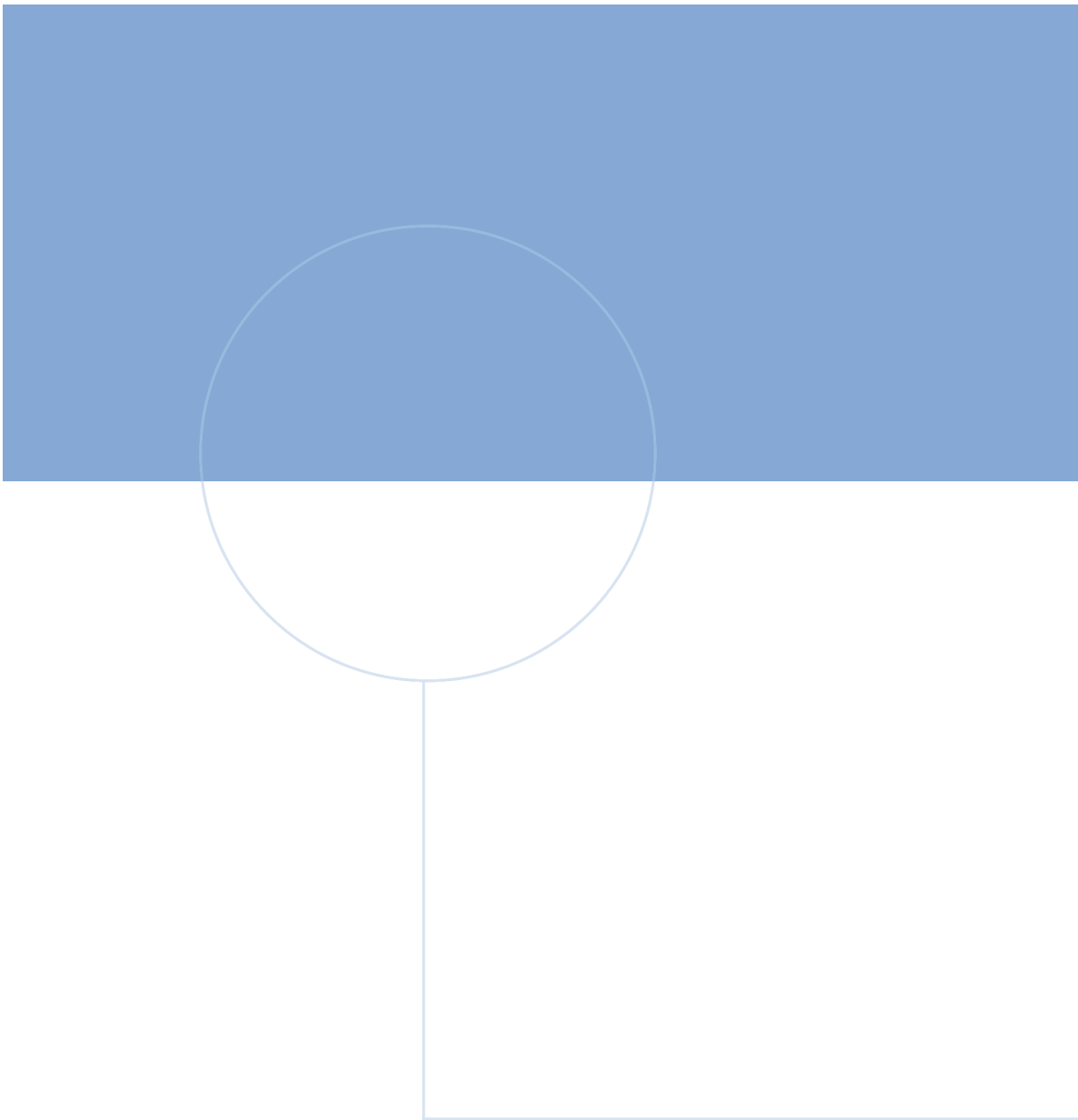

NTNU

Norwegian University of
Science and Technology